Alma Mater Studiorum – Università di Bologna

Facoltà di Scienze Matematiche, Fisiche e Naturali
Dipartimento di Astronomia

DOTTORATO DI RICERCA IN
ASTRONOMIA
Ciclo XXIII

Settore scientifico–disciplinare: Area 02 – Scienze Fisiche
FIS/05 Astronomia e Astrofisica

Multiwavelength studies of hard X-ray selected sources

Presentata da:
Pietro Parisi

Coordinatore dottorato:
Chiar.mo Prof. Lauro Moscardini

Relatore:
Chiar.mo Prof.
Francesco R. Ferraro

Co-relatori:
Dr. Nicola Masetti
Dr. Loredana Bassani

Esame finale anno 2011

Contents

Abstract

Hard X-ray surveys like those provided by IBIS and BAT on board the Integral and Swift satellites list a significant number of sources which are unidentified and unclassified and deserve multiwaveband observations to be properly characterized; in particular cross correlation with various catalogues and follow up optical and X-ray observations can be used to identify and classify the optical counterpart of these sources. In this thesis we have been able to follow up 148 of such sources and have found that 27 are X-ray binaries while 121 are active galaxies. The galactic set includes 18 Cataclysmic variables and 9 high mass X-ray Binaries, including one sg[Be] system. Forty eight of the AGN studied exhibit broad and narrow emission lines which are typical of type 1 AGN, while 69 display only narrow emission lines which are more characteristic of type 2 AGN . The remaining 4 objects have the spectra of normal galaxies and were classified as XBONG (X-ray bright optical normal galaxies). Within the AGN population we found mainly Seyfert 1 and 2, a few Narrow Line Seyfert 1, some Liners and only one source which could not be classified properly. From this sample of AGN, we extracted a set of 94 objects for which we performed an X-ray study, by means of *XMM-Newton* and *Swift*/XRT observations. We determined their X-ray spectral properties and in particular, for most objects in the sample, we measured photon index, absorption column density and X-ray flux. Using a diagnostic diagram we identified a few peculiar sources like unabsorbed type 2 sources and absorbed type 1 objects : the first could be Compton thick AGN candidates, but also AGN without a Broad Line Region while the second maybe AGN viewed from a particular line of sight. Both types of AGN are

unexpected in the classical unified model of AGN. Finally, in the last part of the thesis we have compared the optical properties of these 94 AGN with their X-ray characteristics and discussed our overall results within the framework of the recently proposed clumpy torus models and disk-wind scenario. First, we have compared X-ray (2-10 keV and 20-100 keV) versus optical (R magnitude) properties to search for AGN showing peculiarity with respect to the unified theory: overall, we did not find too many peculiar objects and even the few found could be explained assuming the presence of some X-ray absorption not accounted for and of a bright host galaxy. In agreement with previous works (Winter et al. 2010; Melendez et al. 2008) we did not find evidence for a strong correlation between the [OIII] and 20-100 keV luminosities using the entire sample or type 1 and type 2 AGN separately. This means that the [OIII] luminosity can only be used to predict the hard X-ray luminosity with a large uncertainty. Finally we have compared the X-ray column density (N$_H$) estimated from the X-ray spectroscopy with the optical extinction (E$_{B-V}$) evaluated using optical data, finding that the E$_{B-V}$/N$_H$ ratio is generally around the Galactic standard value for type 1 AGN, while for the more heavily absorbed type 2 sources, is lower by a factor of 10-100. While some of our results seemed, at first glance, in disagreement with the Unified Theory of AGN, they found a natural explanation in the framework of clumpy model and disk-wind scenario. In particular, we can explain the observations of peculiar sources such as absorbed type 1 AGN, naked Seyfert 2 galaxies and a different optical versus X-ray absorption ratio in type 1 and type 2 objects.

Chapter 1

Introduction

A critically important region of the astrophysical spectrum is the hard X-ray band, from 15 to 200 keV. In this band, an unusually rich range of astrophysical processes occurs. This is the energy domain where fundamental changes from primarily thermal to non-thermal sources/phenomena are expected, where the effects of absorption are drastically reduced and where most of the extreme astrophysical behaviour is taking place.

Surprisingly, for such a pivotal region of the astronomical spectrum, the hard X-ray Universe has been relatively unexplored until recently. Only one all sky survey (HEAO-A4, in years 1978-80, Levine et al. 1984) was carried out in the past in this energy range but at relatively low sensitivity and without the benefit of imaging. The survey was a complete one, except in regions of source confusion, down to an intensity level of about 1/75 of the Crab Nebula in the 13-80 keV band and detected a total of 70 sources; of these, 44 were detected in the 40-80 keV energy band while only 14 were detected in the 80-180 keV band. Although most of the detected sources were galactic, seven were extragalactic.

Soon after, the French coded aperture telescope SIGMA on the Russian GRANAT satellite demonstrated the power of wide-field imaging in the 35-300 keV band but it was not extremely sensitive and observed only a small fraction of the sky (primarily the Galactic Center); nevertheless, it provided a catalogue of 37 sources of which 8 were X-ray novae (Revnivtsev et al. 2004).

Finally, the BATSE instrument, aboard the Compton Gamma Ray Observatory (CGRO), provided a monitoring of the low-energy gamma-ray sky (20-1000 keV) over a 9 year period from 1991 to 2000. Using the Earth Occultation Technique, it published a list of 83 objects with 36 additional sources considered as possible detections (Harmon et al. 2004). All these pioneering studies indicated that the sky is rich of sources emitting above 10 keV, the majority being X-ray binaries (with a black hole or a neutron star as accreting object), active galaxies of different types and pulsars.

But there is more than producing a catalogue in the study of the sky at energies greater than 10 keV. To illustrate the power of hard X-ray surveys, we provide here just a couple of cases where hard X-ray observations are crucial: in studying absorbed sources and in exploring spectral features.

Figure 1.1 compares the broad band spectrum of a very bright AGN 3C273 (known to be an unabsorbed object) to that of MKN3 which is instead a heavily absorbed, Compton thick source (see section 1.3.2). While the two objects are similar above 10 keV, i.e. the central nucleus has the same power, the two are remarkably different at lower energies where the emission from MKN 3 is significantly depleted by the high column density (a few 10^{24} cm^{-2}). Galactic and extragalactic objects with such high absorption can only be found and studies by means of hard X-ray surveys.

Another reason for studying the sky at high energies is illustrated in figure 1.2 which shows the broad band spectrum of a typical AGN; on top of the primary power law continuum there are a number of different spectral features, some of which can only be studied by observing above 10 keV, in particular the reflection bump and the power law high energy cut-off (see section 1.3.2 for further details). Both features could be present also in galactic objects and can be explored only having observational coverage at high energies.

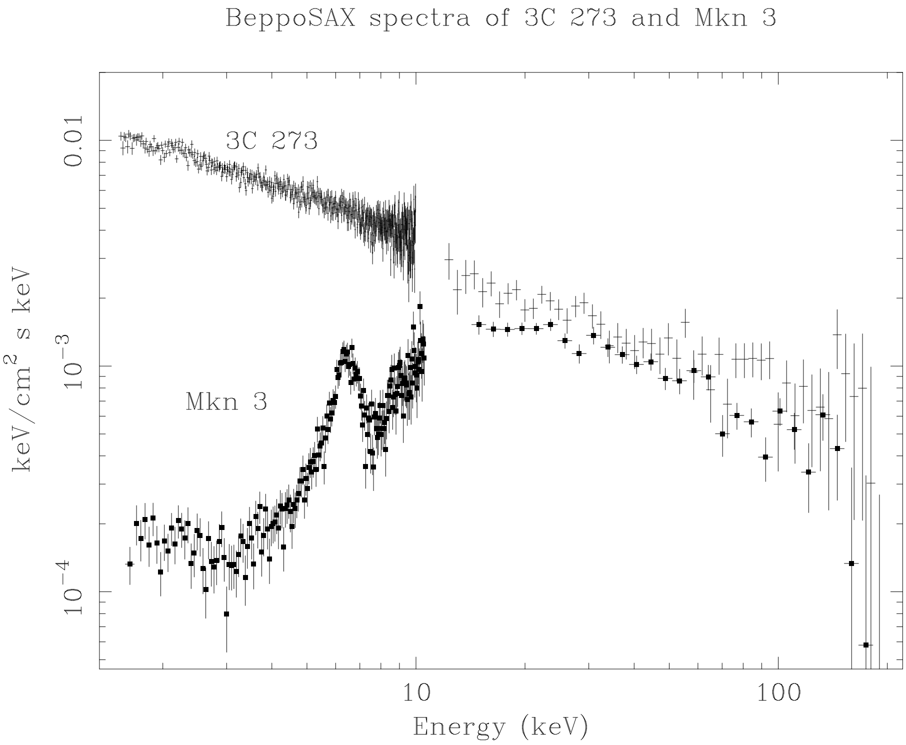

Figure 1.1: X-ray spectra of an absorbed source (Mkn 3) and of an unabsorbed one (3C273).

Recently, the advent of two satellites, INTEGRAL and Swift which carry instruments (IBIS and BAT respectively) operating above 15 keV completely changed our vision of the hard X-ray sky. These telescopes operate in a complementary way, as the first concentrates on mapping the Galactic plane, while the second mainly covers the high Galactic latitude sky, so that together they provide the best yet sample of objects selected in this energy domain. So far, they have found a large number of known and new objects, have discovered new classes of sources and provided a database for follow-up observations and more in depth studies. A brief outline of the surveys provided by these two instruments is given in the following section.

1.1 INTEGRAL/IBIS and Swift/BAT surveys

A sequence of IBIS survey catalogs has been published at regular intervals in the last 6 years as more observations/data become available. The frequent Galactic Plane Scans (GPS) within the

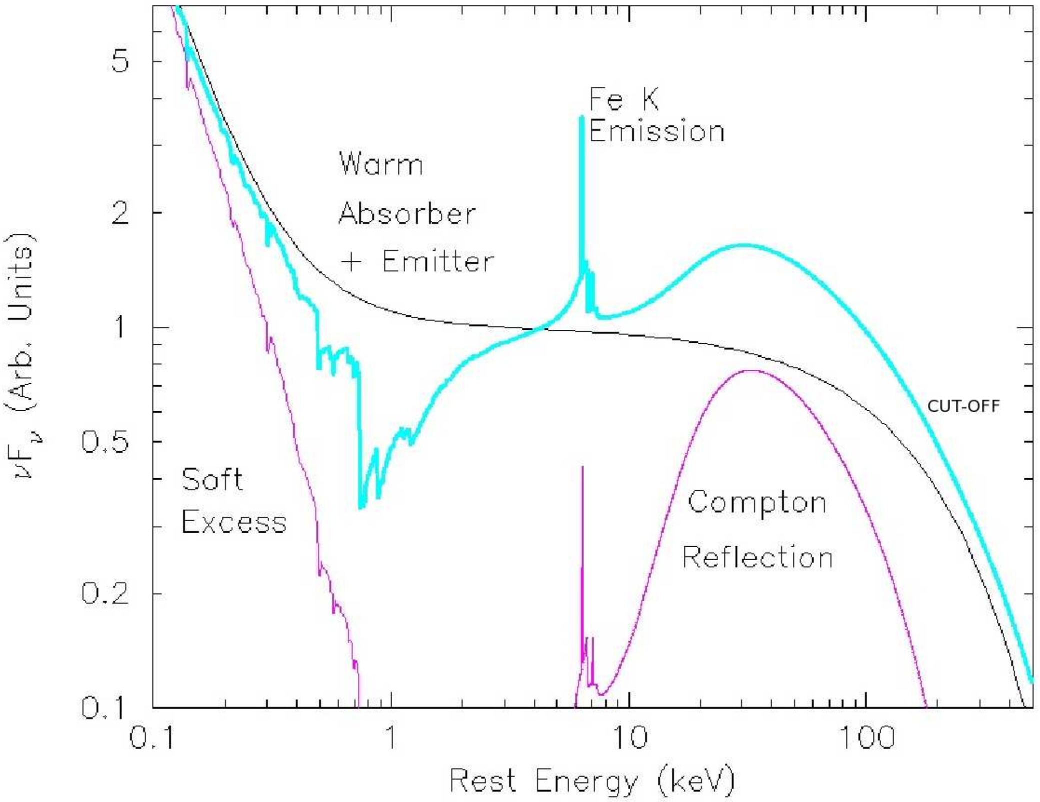

Figure 1.2: Broad band spectrum of a typical AGN. Different colors point out different models. We have in violet the soft excess and the Compton reflection components, in cyan the warm absorber plus emitter and the Iron line.

Core Program, performed in the first year of operations, were successfully exploited to yield a first survey of the Galactic plane to a depth of $\sim$1 mCrab in the central radian (Bird et al. 2004). This gave evidence for a hard X-ray sky populated with more than 120 sources, including a substantial fraction of previously unseen objects. The second IBIS/ISGRI catalog (Bird et al. 2006) used a greatly increased data set (of $\sim$10 Ms) to unveil a sky comprising 209 sources, again with a substantial component ($\sim$25%) of new and unidentified objects. The third IBIS/ISGRI catalog (Bird et al. 2007) further increased the data set, with a substantial improvement in extragalactic coverage, resulting in the detection of a total of 421 sources. The most recent 4^{th} catalogue (Bird et al. 2010) is based on more than 70 Ms of high-quality observations performed during the first five and a half years of the Core Program and public observations. Compared to previous IBIS surveys, this catalog includes a substantially increased coverage of extragalactic fields, and comprises 723 high-energy sources detected in the energy range 17-100 keV, including transients and faint persistent objects that can only be revealed with longer exposure times. Around 684 sources are secure detections of greater than 4.8σ, the remainder are detected between 4.5σ and 4.8σ but still with a good statistical significance. A large fraction (30%) of the objects reported in this 4th survey are unidentified and so need follow up work to be identified and properly classified.

To complement the 4th IBIS catalogue, Krivonos et al. (2010) published an INTEGRAL all sky survey using a newly developed image analysis technique which significantly improves the sensitivity limits reached by the IBIS imager. The survey covers 90% of the sky down to the flux limit of 6.2×10^{-11} erg s^{-1} cm^{-2}, and 10% of the sky down to the flux limit of 8.6×10^{-12} erg s^{-1} cm^{-2}. The survey, which is constantly updated on line[1] contains at the moment 521 objects subdivided in 219 X-ray binaries, 211 AGN and 33 sources which are either unidentified or belonging to other classes. The overlap between the 4th IBIS survey and this all sky survey is obviously quite significant but not perfect due to the use of a different analysis technique as well as of a different set of data.

---

[1] see http://hea.iki.rssi.ru/integral/survey/catalog.php

The most recent BAT/Swift catalog (Cusumano et al. 2010) lists 1256 sources in the range 15-150 keV; it covers 50% of the sky at a flux limit of 1.0×10^{-11} erg s^{-1} cm^{-2} and 9.2×10^{-11} erg s^{-1} cm^{-2} for b $\leq \pm$ 10° and $\geq \pm$ 10°, respectively. This BAT hard X-ray catalogue includes 1079 ($\sim$86%) hard X-ray sources with an associated counterpart and 177 detections ($\sim$14%) that still lack a counterpart. The main difference between the sky surveyed by IBIS and BAT resides in the ratio of the Galactic against extragalactic source populations detected so far. The IBIS sky in the range 20-100 keV is almost equally shared by Galactic (36%), extragalactic (35%), and unidentified sources (29%). Conversely, the extragalactic sources account for 57% of the BAT list, while only 19% of the catalogue is made of Galactic objects. Cross-correlation of the IBIS and BAT source lists results in $\sim$ 420 correlations within 7 arcmins, the number of false correlations at this level should be around 0. This mismatch could be explained by a variety of reasons including the different exposure/sensitivity, larger FOV, and the flaring activity which characterizes many of these high energy emitters, to which BAT is more sensitive.

1.2 The population of high energy emitting sources

In this section we give a brief summary on the type of sources detected at hard X-ray energies so far. This is because one of the main objectives of this work is the identification and classification of unidentified sources reported in the INTEGRAL and Swift surveys described above. In our follow up work, it is indeed important to know which type of object emits above 10 keV so that we can recognize likely counterparts. Because the second part of the thesis is mainly devoted to the study of AGN and in particular of their X-ray and optical properties, we give a more detailed description of these sources, with particular emphasis on their X-ray spectral characteristics and unification theory.

1.2.1 X-ray Binaries

Binaries star systems contain two stars that orbit around their common center of mass. The majority of the stars in our Galaxy have binary companions, isolated stars like the Sun are the exception rather than the norm. A small proportion of binary star systems will evolve into X-ray binaries, where one of the two stars is a collapsed compact object (neutron star or black hole) and the other, normal, star is called the companion. The separation between them is small enough so that the strong gravity of the compact object drags onto it material from the companion. The X-ray emission in these systems (White et al. 1995) is thus due to accretion of matter onto the compact object falling toward it and heated to very high temperatures, over millions of degrees. The geometry of the accretion flow (i.e. spherical accretion or disk) determines the X-ray emission region, which can be the magnetic polar cap of the neutron star, the hot accretion disk surrounding the black hole, a shock heated region in the spherical inflow, or the boundary layer between an accretion disk and a neutron star. In general, X-ray binaries are classified into two different groups according to the mass of the companion donor star. In this work we also take into account another group of X-ray binaries where the collapsed compact object is a white dwarf which are found to be hard X-ray emitters as well. We are thus talking about High Mass X-ray Binaries (HMXBs), Low Mass X-ray Binaries (LMXBs) and Cataclysmic Variables (CVs).

High Mass X-ray Binaries

The companion donor star in HMXBs (Liu et al. 2000) is a massive OB-type star (> 10 M$_\odot$). These systems are the descendants of massive binaries in which the initially most massive star exploded as a supernova, leaving behind a neutron star or a black hole as the compact object. Due to a phase of mass transfer, the secondary star becomes the most massive one in the system before the primary supernova, so that the system remained bound (Van den Heuvel & Heise 1972). HMXBs are relatively young with short lifetimes ($\sim 10^5$-10^7 years). In fact the HMXB phase occurs relatively soon after the supernova explosion in the system, and cannot last longer than the nuclear burning time of the massive companion star. They are distributed along the Galactic Plane, as young stellar populations are (Grimm et al. 2002). To this type of X-ray binaries belong two subclasses: the Be HMXBs and the Supergiant HMXBs.

Be HMXBs dominate the population of known HMXBs in our Galaxy (Lie et al. 2006) and consist of a neutron star orbiting a Be star companion (Negueruela 2004 and Ziolkowski 2002). The Be star is a massive early-type star (mostly B-type) typically close to the main sequence, which has one or more Balmer lines in emission in its optical spectrum. The Balmer emission lines are attributed to the presence of circumstellar material forming a disk around the equator of the Be star. Accretion of this material onto the neutron star is responsible for the X-ray emission in the system while the optical emission is completely dominated by the Be star.

Supergiant HMXBs (SGXBs) host an evolved massive supergiant early-type (OB) companion donor star (from $\sim$ 10 to $\sim$ 60 $M_\odot$) in a relatively tight orbit with a magnetized neutron star or a black hole (Kaper & Van der Meer 2005). Stars in the supergiant phase have a very short lifetime; due to the evolutionary timescales involved, SGXBs are expected to be rare objects, much less numerous than Be/X-ray binaries. The X-ray emission in SGXBs is powered by accretion of material originating from the donor supergiant through two different mechanisms: 1) by stellar wind, the mass loss rates being typically 10^{-6}-10^{-8} $M_\odot$/yr; 2) occasionally by Roche lobe overflow, when the supergiant donor star grows and fills its Roche lobe, some of the material in the star's outer edges is no longer bound to the star, thus flowing into the other lobe through the inner Lagrangian point. Prior to the launch of *INTEGRAL*, the number of galactic wind-fed HMXBs composed of pulsating neutron stars and OB supergiant companions was limited to a few sources. Then, thanks to IBIS sensitivity at hard X-rays and the monitoring strategy of the Galactic plane adopted by INTEGRAL, several new HMXBs could be discovered and identified, either with highly obscured objects or with fast transient X-ray sources characterized by long duty cycles (Sguera et al. 2008); both types of binaries were very difficult to discover with previous missions.

Low Mass X-ray Binaries

LMXBs are systems containing a neutron star or a black hole as the compact object and a low mass (< 1 M$_\odot$) star as donor companion, typically a late type sequence star or a white dwarf (Liu et al. 2001). The X-ray emission is powered by accretion of material originating from the donor star through Robe lobe overflow and forming an accretion disk around the compact object. A bulge or hot-spot occurs where the accretion stream impacts the accretion disk. LMXBs can be transient or very bright persistent X-ray sources. For example, nearly all of the known black hole LMXBs are transient. These sources are found mostly toward the Galactic Bulge (Grimm et al. 2002); moreover, several of them are located in globular clusters. This implies that they are old stellar systems. Many neutron star LMXBs display bursts of X-ray emission, which are very rapid increases in the X-ray output, followed by exponential declines (typically lasting seconds to minutes). The bursts are interpreted as thermonuclear explosions on the NS stellar surface, after material has accumulated due to accretion. During these bursts, the X-ray emission coming from the vicinity of the neutron star dominates that coming from the disk.

Cataclysmic Variables

Cataclysmic Variables (CVs) are close binary systems, with orbital period typically less than one day, where a white dwarf (WD) is accreting material from a late-type main sequency secondary star filling its Roche lobe (for a review see Warner 1995). Amongst the many phenomena that are observed in these systems, the most dramatic are the outbursts that give the class its name. The largest outbursts are shown by *novae*: the star brightens by a factor of more than 10 million in a few days and then fades gradually over months to years. No ordinary nova has been observed to recur as, for theoretical reasons, they should do after an interval of 10^4-10^5 years. Less dramatic, but much more frequent are the *dwarf novae* outbursts: in this case the star brightens by a factor up to 100 in less than a day and fades over the next week or two. They are all seen to recur on time-scales from a few weeks to a few decades. Two other class of objects have been recognised on the basis of their optical properties: *recurrent novae*, known to have eruptive behaviors that fall between the definitions of classical and dwarf novae, and *nova-like* systems, which are stars that have similar spectra to other types of CVs in the visual light, but have not been seen to erupt.

CVs can be broadly divided into two subclasses: non-magnetic and magnetic objects depending on the strength of the WD magnetic field.

In non-magnetic CVs (e.g. dwarf novae and novalike variables), the magnetic field of the WD is not sufficiently strong to dominate the dynamic of the accretion flow. As the accreting matter falls onto the WD, it forms a disk; the infalling matter releases its gravitational energy, heating the accretion disk and the regions where matter falls onto the WD. As a result, radiation is emitted over many frequencies, from infrared to X-rays.

Magnetic cataclysmic variables (mCVs), which represents $\sim$25% of the whole CV class, are themselves divided in two classes: polars (or AM Her type) and intermediate polars (IPs or DQ Her type). In polars the magnetic field is so strong ($B > 10^7$ Gauss) that it forces the WD to spin with the same period of the binary system ($P_{\mathrm{rot,WD}} = P_{\mathrm{orb}}$) and preventing the formation of an accretion disk around the WD. The infalling material is chanelled by the magnetic field along its lines and falls on the magnetic poles of the WD. In the IPs, instead, the weaker magnetic field ($B \sim 10^6 - 10^7$ Gauss) does not synchronize the spin period of the WD with the orbital period of the binary system ($P_{\mathrm{rot,WD}} < P_{\mathrm{orb}}$). In these objects, the accretion process is through a disk, which is truncated in its inner region because of the interaction with the WD magnetosphere; the overall result is the formation of an accretion curtain rather than a converging stream. In these systems, it is also likely that part of the material from the companion can flow directly on the magnetic poles without passing through the disk (disk–overflow).

This class of binaries has re-gained interest recently because they have been detected in large numbers both by IBIS and BAT surveys, whereas very few cases were known before these surveys. The majority of these new hard X-ray selected CVs belong to the IP type with only very few objects ascribed to the polar class.

1.3 Active Galactic Nuclei

Active Galactic Nuclei (AGN) are the most violent, long lived objects in the Universe and are the sites of energy release at the most powerful sustained rates we know of. Active nuclei can be found in the cores of "normal" galaxies, but their emission is so powerful to outshine that of their host galaxy. Such strong emission cannot be, in general, related to stellar activity, but has instead to be traced back to the galaxy central engine responsible for the energy production. The huge observed power is thought to be provided by the release of gravitational energy as the gas in the galaxy spirals towards a Super Massive Black Hole (SMBH), which can have a mass of typically 10^7 $M_\odot$ or more. As a consequence, AGN continuum spectra look dramatically different from those of normal galaxies.

Well-defined and distinctive features of AGN are in fact:

- High nuclear luminosity (10^{41}-10^{47} erg s^{-1}), frequently outshining that of a normal galaxy.
- The presence of strong high ionisation lines in their optical spectra.
- A broad-band continuum emission extending from radio to gamma-rays.
- Rapid variability in the optical continuum as well as in the emission lines.

Such complexity led to an heterogeneous classification based on the continuum, spectral and variability properties. AGN are firstly divided in *radio quiet* (90% of the population) and *radio loud*. Radio quiet objects are further divided in subclasses: high luminosity radio quiet AGN (quasars), Seyfert galaxies, low luminosity AGN and LINERS (Low-Ionisation Nuclear Emission-lines Regions). Radio loud AGN are mainly quasars or blazar type sources. in the following we provide a brief description of the main classes of AGN:

•**Seyfert galaxies**. Among all these different types of sources, Seyfert galaxies, which are dominant type in hard X-ray surveys, represent a major class consisting of AGN which are luminous and located in the nearby Universe, i.e. at $z<0.5$. Seyfert galaxies were first recognised as a separate class of objects by Carl Seyfert in 1943, who found that the optical spectra of these objects were characterised by high ionisation emission lines, with widths up to several thousands km/sec. All Seyfert galaxies show narrow high ionisation emission lines in their optical spectra, indicating the presence of strong ionising radiation. However, some Seyfert galaxies (type 1 Seyferts) also show a broadening of the permitted lines, suggesting the presence of a dense ($\rho \geq 10^9$ cm^{-3}) and fast moving ($v \sim 10^4$ km s^{-1}) gas. Sources which instead show only narrow emission lines are classified as type 2 Seyferts. In between type 1 and 2 Seyferts there is a wide variety of intermediate types, where the broad line components are weakly observable. A peculiar type of Seyferts are the Narrow Line Seyfert 1 (NLSy1) galaxies; their defining criterion is the width of the broad component of their optical Balmer emission lines in combination with the relative weakness of the [OIII] emission (FWHM $H_\beta \leq$ 2000 km/s and [OIII]/$H_\beta < 3$). NLSy1 also show strong FeII emission which anticorrelates in strength with the [OIII] emission, and with the width of the broad Balmer lines. A popular explanation of the differences in the optical properties across the Seyfert population is that NLSy1s have smaller black hole masses than their broad line analogues. Given that NLSy1s have comparable luminosity to that of the broad line Seyferts, they must be emitting at higher fractions of their Eddington luminosity. Thus a plausible scenario is one in which NLSy1 have not yet been fed enough to become massive and are therefore in a rapidly growing phase; if this is true they are key objects for studying the formation and evolution of active galaxies.

•**Radio galaxies** are usually elliptical. They often exhibit jet structure from a compact nucleus. They typically show two lobes of radio frequency emission that are often approximately aligned with the jets observed in the visible spectrum and that may extend for millions of light years. Sometimes the optical counterparts of radio galaxies show a continuum emission and/or emission lines (broad and narrow) similar to those seen in Seyfert galaxies; consequently we may have Broad Line Radio Galaxies or Narrow Line Radio Galaxies.

•**QSO** (Quasi Stellar Objects) are point-like sources (hence the name) at high redshift ($z >$

0.5). They show an intense continuum and broad and narrow emission lines like those observed in Seyfert galaxies. Few QSO are similar to radio galaxies since they show lobes and strong radio emission (Radio Loud QSO); the majority behave like Seyfert galaxies as they do not show powerful emission at radio frequencies (Radio Quiet QSO).

•**BL Lac** objects are characterized by rapid and large amplitude flux variability and significant optical polarization; they are named after the prototype, BL Lacertae. When compared to QSO and Seyfert galaxies optical spectra, which are dominated by strong emission lines, BL Lac objects have spectra characterized by a featureless non-thermal continuum. They are hosted in massive spheroidal galaxies and are associated with core dominated radio sources; many of them exhibiting radio jets with superluminal motion.

•**LINERS** are galaxies characterized by a low-ionization nuclear emission-line region. LINERs are very common in the nearby universe as approximately one third of all nearby galaxies may be classified as LINERs (Heckman, 1980). Despite this and the long time passed since their discovery, there is still an ongoing strong debate on the origin of their energy source, with two main alternatives for the ionizing source being considered: either a low luminosity AGN or a thermal origin from massive star formation.

•**Starburst galaxies** are otherwise normal galaxies that are undergoing an intense episode of star formation. They contain many HII regions illuminated by hot, young stars, and the emission lines show up clearly in the optical spectrum. We mention starburst galaxies here because, as we will see, their spectra have a resemblance to active galaxies, and it is important to be able to distinguish the two.

Active galaxies are an important ingredient of the population of hard X-ray emitting objects as shown both by IBIS and BAT surveys: the majority of the hard X-ray selected AGN is made of Seyfert galaxies of type 1 and 2, plus some QSO and BL Lac objects. Other typologies of AGN (Narrow line Seyfert 1, XBONG) are by far less important although recently they have appeared among the newly identified and optically classified objects as shown in the following chapters of this work.

1.3.1 AGN Structure and Unified Theory

As already mentioned, AGN derive their power from accretion onto a super massive black hole, and the primary continuum emission peaking at UV/soft X-ray wavelengths, with a tail in the optical and extending up to few hundreds keV. Despite the fact that many different types of AGN are observed, all of them seem to have some common underlying characteristics, thus representing different aspects of the same astrophysical phenomenon. A unified scenario has been developed both for radio loud (Urry & Padovani 1995) and Seyfert galaxies (Antonucci & Miller 1985), which is explained in the following and is outlined in figure 1.3.

The structure of an AGN can be characterised by the presence of the following regions:

•**Black Hole and Accretion Disk**: kinematic observations of a significant number of galaxies show evidence for central black holes with masses between 10^6 and 10^9 $M_\odot$ (Kormendy & Richstone 1995). Around the central black hole, the accretion disk is where the primary emission comes from, although its structure and emission mechanisms are still a matter of debate. Shakura & Sunyaev (1973) proposed a model in which the accretion disk is optically thick but geometrically thin. In this model, the efficiency of the accretion process, i.e. the ratio between the average radiated energy per particle and the particle rest energy, can reach the maximum allowed by a general relativistic gravitational potential. Another model, proposed by Narayan et al. in 1998, involves the *Advection Dominated Accretion Flow* mechanism (ADAF). In this scenario, the energy transfer from baryons (which gain much of the gravitational energy) to electrons (which radiate most efficiently) is highly inefficient. Therefore baryons fall into the last stable orbit maintaining most of their energy and the ratio between the radiated luminosity and the accretion mass is low. This mechanism is the favoured one for explaining the accretion geometry of the lowest luminosity AGN.

•**Broad Line Region (BLR)**: the broad lines observed in Seyfert galaxies optical/UV spectra

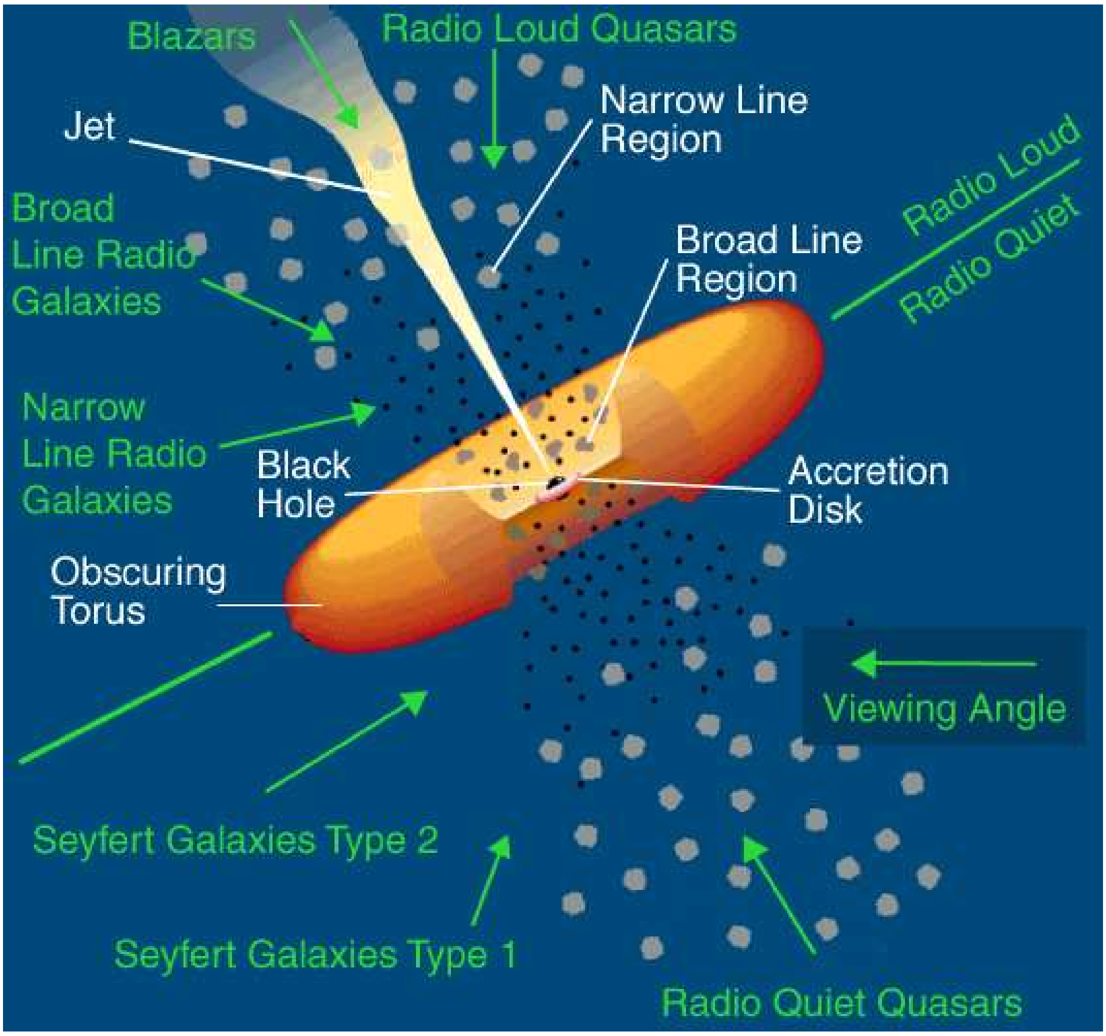

Figure 1.3: A schematic view of an Active Galactic Nucleus. A central black hole surrounded by a luminous accretion disk. Broad emission lines are produced in clouds orbiting above the disk, called broad-line regions. A thick dusty torus obscures these broad-line regions at some angle of the line of sight. Narrow lines are produced in clouds farther away from the central source. As it can see form this figure, the different classification of an AGN depends from the line of sight of the observer (Urry & Padovani 1995).

have typical widths of 5000 km s^{-1} up to 10^4 km s^{-1}. These large widths are interpreted as due to Keplerian velocities of large numbers of clouds rotating around the central black hole at distances of 0.01-0.1 pc. The density of this gas is believed to be very high ($\rho \geq 10^9$ cm^{-3}), as required by the observed ratio between the permitted and forbidden emission line transitions. The typical processes involved in the BLR are mainly photoionisation heating and Bremsstrahlung cooling.

•**Narrow Line Region (NLR)**: narrow lines, which are also commonly observed in AGN, have much smaller widths ($\sim$100 km s^{-1}) than broad lines. This can be explained if these lines are produced by material placed further away from the central black hole, extending on scales of typically 100 pc. The gas is also less dense ($\rho \sim 10^3$-10^6 cm^{-3}) than that present in the BLR.

•**Obscuring Molecular Torus**: this is the key component of unification scheme. It prevents the direct observation of the BLR if the line of sight intercepts it and it is usually located at $\sim$1 pc from the central black hole. It is thought to be made of a thick toroidal wall of dust and molecular gas, whose vertical axis is perpendicular to the equatorial plane of the accretion disk. According to the unified model developed by Antonucci & Miller in 1985, type 2 galaxies harbour a bright type 1 nucleus hidden from our view by an optically and geometrically thick torus. This picture implies that type 1 and 2 AGN are essentially the same objects viewed at different inclination angles. Direct observational evidence for this unified model came from spectro-polarimetric observations of some narrow line objects, revealing hidden polarised broad lines (Antonucci & Miller 1985; Tran 2001), scattered by free electrons in a mirror of ionised gas located just outside the opening of the torus, as well as from detection of maser-like structures orbiting around a central super massive object on scales of 0.1-1 pc in some nearby AGN (Greenhill et al. 1996). Additional strong support has been obtained from X-ray observations of Seyfert 2 nuclei showing heavy photoelectric absorption due to cold gas, likely associated with the dusty torus (Matt et al. 2003). Variability in the X-ray column density of type 2 sources (Risaliti et al. 2002), associated with clouds in close proximity to the AGN (<0.1 pc) also suggests that X-ray absorption, broad line emission, dust obscuration and reprocessing are produced by a single, continuous distribution of clouds. According to a recent model (Elitzur 2008) the torus can also be considered as made of dust-free clouds that absorb X-rays. In this scenario, the torus is also considered as a continuation of the Broad Line Region, that extends to the inner boundary of the torus, and not a separate entity, as suggested also by IR reverberation observations (Suganuma et al. 2006).

Besides orientation, the bimodality of the radio luminosity of AGN (when normalised to their optical power) has also led to the distinction between radio loud and radio quiet objects. A unification model which takes into account the different properties observed among radio loud AGN, also including the presence of a relativistic jet, has been proposed by Urry & Padovani (1995). According to these authors, radio jets in radio loud AGN introduce another element of anisotropy in addition to the torus. Because of relativistic beaming effects, if our line of sight is along the radio jet direction, then its emission completely dominates the underlying nuclear continuum emission and the source is classified as a *Blazar*. As the viewing angle increases, the strength of the beamed component decreases, thus explaining the different spectral characteristics observed along the sequence Blazar-RL quasar-Broad Line Radio Galaxy-Narrow Line Radio Galaxy. The latter two classes can be considered as the radio loud counterparts of Seyfert 1 and Seyfert 2 galaxies respectively.

1.3.2 X-ray emission

The source of X-rays in AGN is located in the very inner nuclear region of the accretion disk, where most of the gravitational energy is released. Thermal emission emerges from an optically thick disk, providing the bulk of photons with energies spanning from the optical to the extreme UV/soft X-ray range. The Comptonisation of such photons occurs in a hot optically thin corona made of "thermal" mildly relativistic electrons (i.e. with $kT_e \sim 200$ keV) which extends above the accretion disk. There is a general consensus in indicating successive inverse-Compton scatterings of softer seed photons as the main production mechanism of X-rays.

The particle acceleration, i.e. the coronal heating mechanism, is often said to be due to dissipation of accretion energy generated in magneto-rotational instabilities in the disk and eventually transferred in the corona via reconnection of magnetic loops. However, this issue is far from being clear and also the geometry of the corona itself is almost unknown. The irradiated energy from the corona, in turn, is believed to be the main source of heating for the disk, introducing a coupling between the corona and the disk (Haardt & Maraschi 1993).

Comptonisation models account for the overall “first-order” spectral shape of AGN observed in the X-ray band, i.e. a high energy cut-off power law with a photon index $\Gamma \sim$1.8-2. However, a detailed examination of AGN spectra reveals the existence of many additional components to the simple power law model, that have been interpreted as signatures of the reprocessing of the primary nuclear continuum by some material located around the central engine (Mushotzky, Done & Pounds 1993). This is the best way to get a complete description of the geometry and the nature of the accretion process of an AGN. In the following we report the main features of an AGN X-ray spectrum:

•**Neutral Absorption**: one of the most conspicuous broad spectral features observed in the X-ray spectra of active galaxies is the cut-off in the soft X-ray region due to absorption by material associated with the interstellar medium in our Galaxy and by material local to the source. This material suppresses the primary power law-like continuum via photoelectric absorption. The observed values for the intrinsic absorption column density span from $N_H \sim$few$\times 10^{20}$ cm^{-2} up to $N_H > 10^{25}$ cm^{-2}. When N_H exceeds 1.5×10^{24} cm^{-2} (i.e. the inverse of the Thomson scattering cross-section), the Compton scattering optical depth equals unity and the source is defined to be ‘Compton-thick’, otherwise the source is defined ‘Compton-thin’.

•**Reflection Component**: The optically thick material of the disk is irradiated by the primary X-ray emitting source: soft X-ray (<10 keV) photons incident on this material are photoelectrically absorbed by ions of elements such as C, O and Fe and subsequently thermalised. On the other hand, photons with harder energies (>30-40 keV) incident on the disk are backscattered via Compton scattering, transferring only $\sim$10% of their energy to the disk. This scattered emission from the optically thick material (the so-called ‘reflection’ component; Guilbert & Rees 1988; George & Fabian 1991) results in a broad hump, peaking at $\sim$30-40 keV, due to the combination between Compton scattering at high energies and absorption at low energies.

•**Fluorescent Emission Lines**: The most prominent line, among those of an X-ray spectrum, is the typically narrow Fe Kα at 6.4 keV in the case of neutral iron. This value slowly rises up to 6.9 keV in the case of fully ionised iron. The combination of fluorescence yield ($\propto$Z^4) and relative abundance of iron justifies the strength of this feature. A line arising from a rotating disk is expected to have a double-peaked profile (e.g. Fabian et al. 2002): however, the detailed profile of the observed line strongly depends on several parameters such as the geometry assumed for the primary X-ray source, the inclination of the emitting region with respect to our line of sight and/or the disk emissivity law. Moreover, contributions to the Fe Kα emission are also expected from reflection onto the optically thick torus and onto the BLR and NLR clouds (Ogle et al. 2000). Hence the final profile as well as the intensity of the line are both quite difficult to interpret.

Note that type 2 AGN are expected to have larger Fe Kα equivalent widths (EWs), since most of their primary continuum is intercepted by the torus and the Fe Kα photons are also produced by transmission through such absorbing material. Moreover, other Fe Kα photons originate by reflection in the inner, farthest, part of the torus. In the most extreme cases (i.e. Compton-thick sources) the direct continuum is completely absorbed, only the reflected component can be observed, thus providing the most extreme values of EWs (up to $\sim$2 keV, e.g. Levenson et al. 2002).

•**Warm absorber and Soft Excess Emission**: Often an X-ray spectrum shows the presence of two more components occurring in the soft band: the warm absorber and the soft excess. The high resolution soft X-ray spectra of bright type 1 AGN obtained with soft X-ray telescopes show many absorption lines and few emission lines from hydrogen-like and helium-like ions of the most common metals (see Krolik & Kriss, 1995, for a theoretical review). The column densities of several atomic species are typically in the range of $\sim 10^{19}$-10^{21} cm^{-2}. Moreover, absorption lines are found to be blueshifted, suggesting that they are emitted from an outflowing wind (Kaspi et al. 2001). The most plausible location for this photoionised gas appears to be a stratified absorber with different ionisation levels, lying a few parsecs from the nucleus and extending up to the NLR. On the basis of *Chandra* and *XMM-Newton* data, Kinkhabwala et al. (2002) and Sako et al. (2001) have found that this warm ionised absorber is also responsible for the soft X-ray scattered emission seen in obscured Seyfert 2 galaxies. The same gas absorbing the primary continuum in face-on (type 1) objects produces the “secondary” emission line spectrum observed in edge-on (type 2) sources. These findings allow to infer many important parameters, such as the geometry and the physical conditions of the innermost regions of AGN and they also provide a further strong support to Unified Models.

As far as the soft excess emission in type 1 objects is concerned, two physical interpretations are given on the basis of the observational properties (Pounds & Reeves 2002). In the case of a “sharp” soft excess, the most plausible explanation is that it originates as reprocessing of the hard X-ray emission by the inner parts of the disk (i.e. the soft X-ray portion of the reflection spectrum, see also Branduardi-Raymont et al. 2001). On the other hand, if the upturn gradually emerges below 2-3 keV (“gradual” soft excess) the emission is believed to be the Comptonised hard tail of the Big Blue Bump (i.e. the thermal emission arising directly from the disk).

Chapter 2

X-ray satellites and optical telescopes

2.1 Introduction

As already point out in the introduction, sources reported in recent high energy surveys are often unidentified and unclassified and hence need of follow up observations both in X-rays (to reduce the positional error box, pinpoint the likely counterpart and study its spectral properties) and in optical (to classify the likely association/s). This work is done with a number of instruments operating at X-ray energies and at optical frequencies and which are described in the present chapter. We start with a description of the *INTEGRAL* and *Swift* satellites and in particular of the instruments which have been used in this work: IBIS in the first case and BAT and XRT in the second. IBIS and BAT are the two instruments used to provide the high energy surveys from which we selected the sources for our follow up identification program (see Chapter 3). The XRT instrument has instead been used for the X-ray follow up work, while a number of ground based telescopes located around the world have been employed for the optical spectroscopic studies. Where possible, also *XMM-Newton* has been used for some sources for our X-ray follow-up work, because of its positional accuracy (see previous sections). An insight into these instruments will provide the reader with an idea of the instrument complexity, capabilities and on the expertise concerning broad band data analysis also broad band expertise acquired by myself during this work.

2.2 X-ray satellites and instruments

In this work we have used data from a number of X-ray instruments located onboard various space borne satellites. In the following we briefly described the satellites characteristics and then we go into a more detailed description of the X-ray detectors used in this work.

2.2.1 *INTEGRAL*

The ESA satellite *INTEGRAL* (*INTErnational Gamma Ray Astrophysics Laboratory*) is dedicated to high resolution spectroscopy and high resolution imaging in the energy range 15 keV-10 MeV. *INTEGRAL* can also perform simultaneous observations of the X-ray (3-35 keV) and optical (V band, 550 nm) bands thanks to two smaller monitors, JEM-X and OMC (Winkler et al. 2003).

INTEGRAL, one of ESA's medium size missions within the "*Horizon 2000*" programme, was successfully launched from Baikonour (Kazakhstan) on October 17, 2002. The mission is managed by ESA with contributions from 16 European countries, as well as from Russia (participating with the PROTON launcher) and from NASA (participating with the *Deep Space Network* ground stations).

The satellite (see figure 2.1) was placed in a highly eccentric orbit with a high perigee, so to allow long uninterrupted observations with a practically constant background, far from the radiation belts around the Earth. The initial orbital parameters were: an orbital period of 72 hours with an inclination of 52.2°; perigee at 9000 km; apogee at 154 000 km. In order to reduce the instrumental background, all scientific observations are conducted when the satellite is at a nominal altitude of 60 000 km when approaching the radiation belts and above 40 000 km when

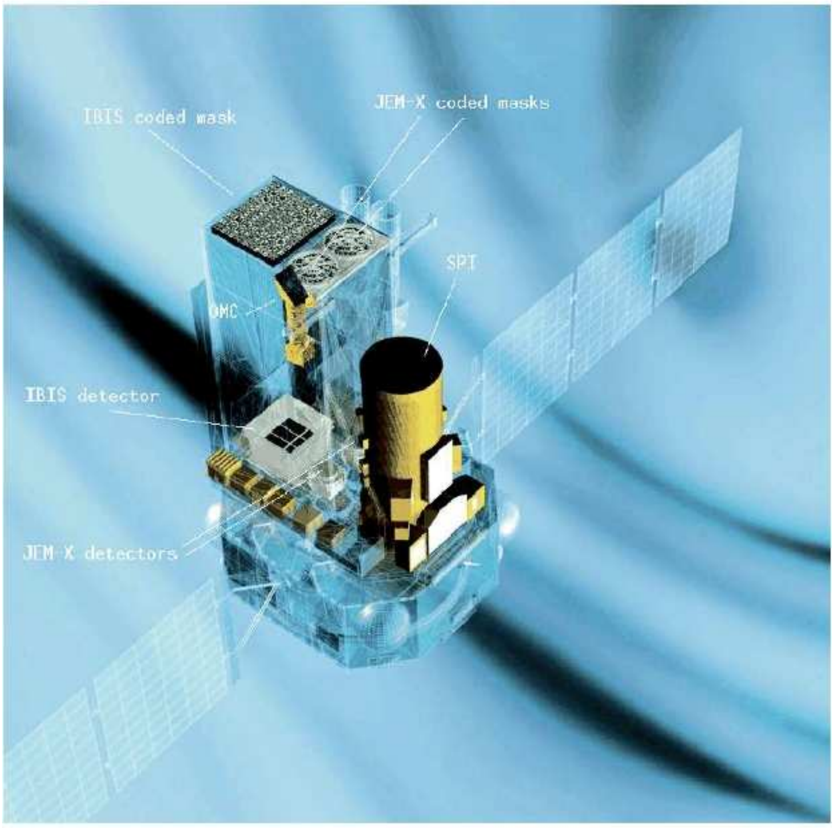

Figure 2.1: The *INTEGRAL* satellite.

moving away from the belts. This means that during a single orbit, the satellite can perform scientific observations for about 90% of the time.

The *INTEGRAL* nominal lifetime was initially 2 years renewable for other 2 but the satellite is celebrating, 9 years of activity on October 2011 and has been founded until the end of year 2013.

The overall dimensions of the *INTEGRAL* satellite are $5 \times 2.8 \times 3.2$ m. When deployed, the solar panels are 16 m long; the total mass is $\sim$4 tons, including $\sim$2 tons of scientific instrumentations.

INTEGRAL has two main gamma ray instruments on board: a spectrometer, SPI (*Spectrometer on INTEGRAL*; Vedrenne et al. 2003), and an imager, IBIS (*Imager on Board INTEGRAL Satellite*; Ubertini et al. 2003). These two instruments provide high energy and angular resolution, respectively, coupled with good sensitivity over a wide field of view. Two monitors, JEM-X (Lund et al. 2003) for the X-ray band and OMC (Mas-Hesse et al. 2003), operating at optical wavelengths, are also part of the payload.

The spectrometer, imager and the X-ray detector share a common principle: they all are, in fact, coded mask telescopes. The coded mask technique is crucial for high energy imaging and for the separation and positioning of sources. Coded mask instruments also offer an almost perfect background subtraction, since, for any pointing direction, the detector pixels can be considered as split into two separate sets: one able to “see” the source and another in which the flux is blocked by the opaque elements of the mask. The latter set provides a simultaneous measurement of the background for the other on-source set under the same conditions.

All instruments are co-aligned, with overlapping fully-coded fields of view (FoV), ranging from 4.8° for JEM-X, to $5^\circ \times 5^\circ$ for OMC, $9^\circ \times 9^\circ$ for IBIS and 16° (diagonal) for SPI. Since in this thesis we will used data collected by IBIS, in the following this instrument will be described briefly.

The IBIS instrument

IBIS is a coded mask telescope (Ubertini et al. 2003), constituted by two main components: a mask which constitutes the telescope aperture and a detector to collect the incident radiation (see fig. 2.2). The detector is positioned on-axis below the mask and consists of two layers: ISGRI (*INTEGRAL Soft Gamma Ray Imager*; Lebrun et al. 2003) and PICsIT (*Pixellated Imaging CsI Telescope*; Labanti et al. 2003). ISGRI is constituted of solid state position sensitive CdTe (Cadmium Telluride) detectors, optimised to operate between 15 keV and 1 MeV; PICsIT is instead made of scintillating CsI (Cesium Iodide) crystals, optimised for a higher energy range between 175 keV and 20 MeV. This double-layer configuration ensures a good continuum and broad line sensitivity over the whole energy range in which IBIS operates. The instrument also possesses an anticoincidence system in order to be able to reject events caused by photons present

Figure 2.2: IBIS during the last phases of mechanical integration at ESTEC.

in the background or produced inside the satellite itself. A collimation system is also present so to keep the low energy response of IBIS; it consists of a passive lateral shield that limits the solid angle (and therefore the cosmic gamma-ray background) viewed directly by the IBIS FOV up to a few hundreds of keV. Data used in the present work were collected by the ISGRI instrument in the 20-100 keV and so we provide here more information on this detector.

ISGRI is constituted by 8 identical *Modular Detection Units* (MDUs), each containing 2048 pixels read by 512 *Application Specific Integrated Circuits* (ASICs). Each of the 16348 CdTe pixels of which ISGRI is made has a size of 4×4 mm^2 and a thickness of 2 mm. The small pixel area is responsible for the good spatial resolution, even if the relative thinness of the pixels implies that they can be used only at low energies. ISGRI total area is about 3600 cm^2, while the operative area is 2621 cm^2. ISGRI provides images of the sky with an angular resolution of 12 arcmin and a point source location accuracy of few arcminutes. The detector sensitivity is at the mCrab level for long enough exposures (typically 10^6 s)

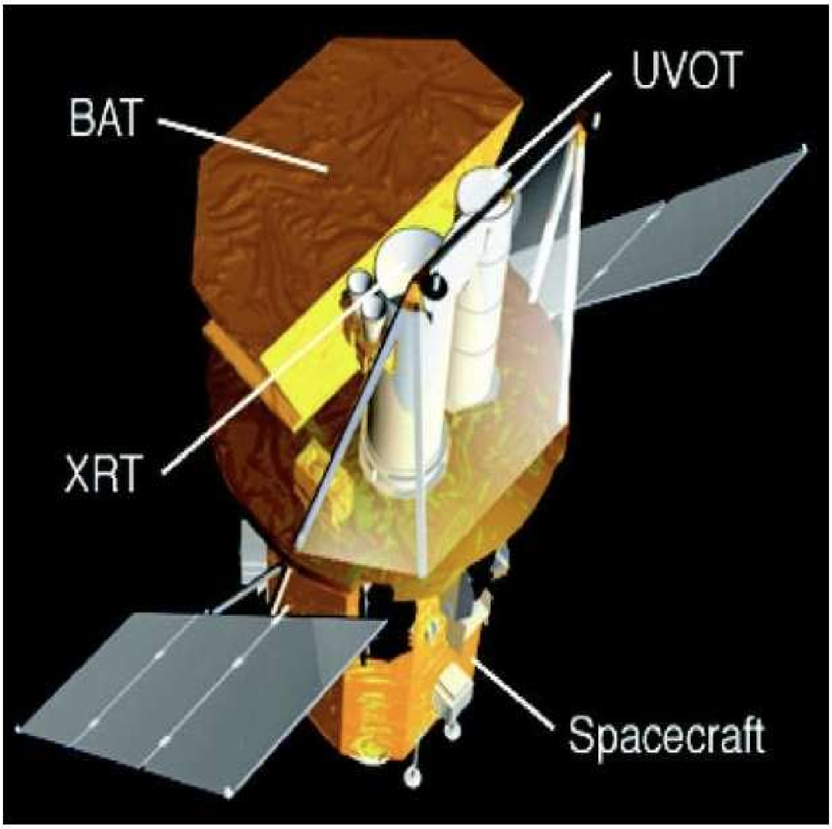

Figure 2.3: Image of the *Swift* satellite and its main instruments.

2.2.2 Swift

The *Swift* Gamma-ray Burst Explorer (Gehrels et al. 2004) is a NASA's multi-wavelength space-based observatory primarily dedicated to the study of gamma-ray burst (GRB) science. Its instruments work together to observe GRBs and their afterglows in the gamma-ray, X-ray, ultraviolet, and optical wavebands. In the time between GRB events, *Swift* is available for other science objectives like a full survey of the sky at hard energies and X/UV observations of interesting sources. The Swift Gamma-Ray Burst Mission was launched into orbit on 20 November 2004, 17:16:00 UTC on the Delta II 7320-10C series expendable launch vehicle. *Swift* is managed by the NASA Goddard Space Flight Center, was developed by an international consortium formed by the United States, United Kingdom, and Italy and is part of NASA's Medium Explorer Program (MIDEX). The *Swift* satellite (see figure 2.3) settled into low Earth orbit at an altitude of 600 km and with an inclination of 20.6 degrees. It orbits the Earth once every 96 minutes. The mission had a nominal on-orbit lifetime of 3 years but it will celebrate 7 years of activity on November 2011. The overall dimensions of the *Swift* satellite are 5.7×2.7m; the total mass is $\sim$1.47 tons.

The *Swift* scientific payload is made of three instruments which work together to meet the scientific objectives of the mission: the Burst Alert Telescope (BAT; Barthelmy 2004), which is very similar to the ISGRI detector on board *INTEGRAL* ; the X-ray Telescope (XRT; Burrows et al. 2004) which is optimized for the X-ray band, and an Ultraviolet/optical telescope (UVOT; Roming et la. 2005). Since BAT coded aperture field of view always covers both the XRT and UVOT FoVs, sources observed by BAT (including GRBs) can be studied simultaneously with the X-ray and optical instruments. In this thesis we have made use of data collected by BAT and XRT, and so both instruments will be described in more details in the following sections.

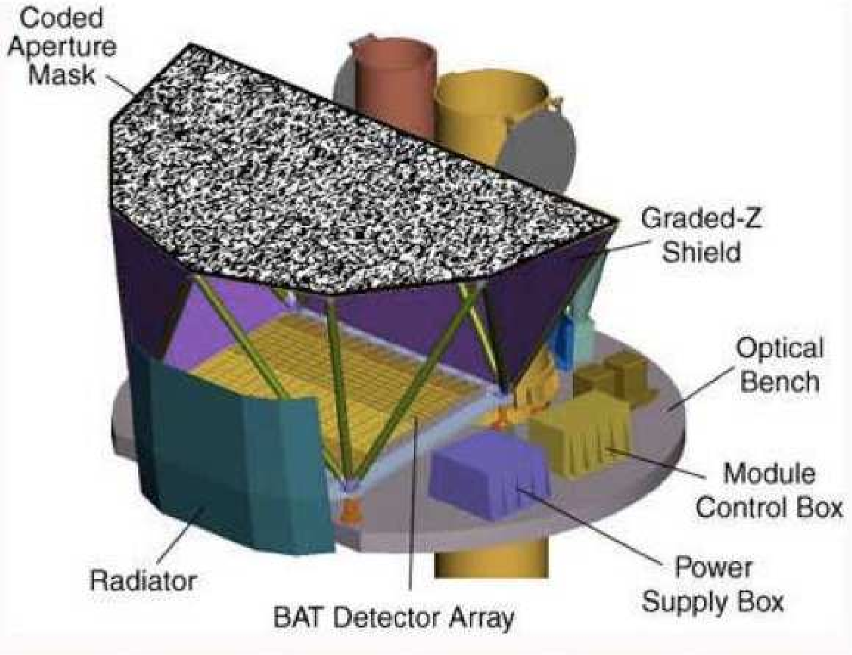

Figure 2.4: A schematic view of the Burst Alert Telescope aboard the *Swift* satellite (credits: http://swift.gsfc.nasa.gov/docs/swift/swiftsc.html).

The BAT Instrument

BAT uses a two-dimensional coded aperture mask and has a large area solid state detector array made of 32768 pieces of 4x4x2 mm CdZnTe (CZT) to form a 1.2x0.6 m sensitive area in the detector plane (fig. 2.4). Groups of 128 detector elements are assembled into arrays, each connected to 128-channel readout Application Specific Integrated Circuits (ASICs). Detector modules, each containing two such arrays, are further grouped into blocks. This hierarchical structure, means that BAT can tolerate the loss of individual pixels, individual detector modules, and even whole blocks without losing the ability to detect sources and determine their locations.

The BAT coded aperture mask is made of approximately 54000 lead tiles mounted on a 5 cm thick composite honeycomb panel; it has an area of 2.7 m, yielding a half-coded FoV of 1.4 steradians.

A graded-Z fringe shield, located both under the detector plane and surrounding the mask and and detector plane, reduces the background from the isotropic cosmic diffuse flux and the anisotropic Earth albedo flux by approximately 95%. The shield is composed of layers of Pb, Ta, Sn, and Cu, which are thicker toward the bottom, nearest the detector plane, and thinner near the mask.

BAT instrument runs in two modes: burst mode, which produces GRBs and X-ray transient positions; and survey mode, which produces hard X-ray survey data. In the survey mode the instrument collects count-rate data in five-minute time bins for 80 energy intervals. When a burst occurs it switches into a photon-by-photon mode.

BAT, operates in the 15-150 keV energy range, has an angular resolution of 17 arcmin and a point source location of 1-4 arcmin; sky images are then searched to detect sources and their positions, with a sensitivity of few mCrab.

The XRT Telescope

XRT is a focusing X-ray telescope with a 110 cm^2 effective area, a 23 arcmin field of view and an 18 arcsec resolution (HPD), operating in the 0.2-10 keV energy range. It uses a grazing incidence Wolter I telescope that focuses the X-rays onto a CCD at a focal length of 3.5 m.

The instrument has three read-out modes: the Imaging Mode, the Windowed Timing Mode and the Photon Counting Mode. The Imaging Mode produces an integrated image by measuring the total energy deposited per pixel, but does not allow spectroscopy. The Windowed Timing Mode has a high time resolution (2.2 ms); it allows spectroscopy for bright sources and is most useful for objects with F$<10^{-7}$ erg cm^{-2}s^{-1}. The Photon Counting Mode is capable of retrieving spectral and spatial information for sources having a flux $\geq 2\times10^{-11}$ erg cm^{-2} s^{-1} in the 0.3-10 keV.

The mirror module is composed of 12 nested gold-coated Ni mirrors; the focal plane camera houses an *XMM*/EPIC MOS CCD (see next section), which has an image area of 600×602 pixels (40 μm×40 μm in size, corresponding to 2.36 arcsec). The XRT structure is made of an optical bench interface flange and a telescope tube composed by two sections: the forward telescope tube, supporting the star trackers and the telescope doors, and the rear section which houses the focal plane camera.

The main scientific requirements of the XRT instrument are rapid and accurate positioning ($<$5 arcsec), moderate resolution spectroscopy ($>$400 eV at 6 keV) and accurate photometry.

2.2.3 *XMM-Newton*

The *XMM-Newton* (X-ray Multi-Mirror Mission - Newton) is an orbiting X-ray observatory, named in honor of Sir Isaac Newton. Originally known as the High Throughput X-ray Spectroscopy Mission, it was launched by the European Space Agency from the Guyana Space Centre at Kourou on 10 December 1999 by an Ariane 5 rocket. It was placed in a very eccentric 48 hour elliptical orbit at 40° of inclination with respect to the equator; at its apogee it is nearly 114,000 kilometres from Earth, while the perigee is only 7,000 kilometres. This particular orbit was chosen so that the main X-ray instruments could be passively cooled to temperatures between -80° and -100°. Scientific operations can only be performed when the satellite is above an altitude of 60 000 km, since the lower part of the orbit passes through the Earth's radiation belts. The *XMM-Newton* mission was realized by a consortium of universities and industrial groups from 14 European countries. It is part of ESA's cornerstone missions within the Horizon 2000 programme The original mission lifetime was two years, it has now been extended until 2012, and technically could operate for much longer. The satellite weighs 3,800 kilograms, is 10 metres long and 16 metres in span with its solar arrays deployed.

XMM-Newton carries on board two types of telescopes: three very advanced and parallel-mounted X-ray telescopes and a 30 cm optical/UV telescope. The three X-ray telescopes use Wolter mirrors to focus the X-rays onto the detector. The mirrors grazing incidence angles vary from 17 to 42 arcminutes, their focal length is 7.5 meters and the diameter of the largest mirror is 70 cm (see Fig. 2.5). The X-ray detectors or cameras are placed at the focal plane of each telescope, which has therefore its own photon imaging camera to record the acquired data; two of the cameras are also equipped with reflection grating spectrometers (RGS) to measure the wavelength, and hence the energy of the incoming X-ray radiation. The high-precision concentric mirrors are delicately nested to offer the largest collecting area possible to catch the elusive X-rays: each telescope has in fact a total mirror geometric effective area of 1550 cm^2 at 1.5 keV, thus reaching 4650 cm^2 in total. The large effective area implies a large sensitivity and the consequent detection and study of a large number of sources. The X-ray telescopes have a Point Spread Function (PSF) of 6” (FWHM), providing a very food angular resolution. In addition, the *XMM* camera can reach moderate (E/Δ 20-50) to high (E/Δ 200-800) spectral resolution depending on the detectors used, thus allowing a high spectroscopic power. Furthermore, the satellite’s highly eccentric orbit, travelling out to nearly one third of the distance to the Moon, enables the observers to make very long and uninterrupted observations thus allowing the study of flux and spectral variability of the source/sources detected.

The co-aligned optical/UV monitor, provides sensitive coverage of the sky region containing the X-ray sources over the 1600-600 Å waveband. All *XMM* instruments can operate simultaneously when conditions are favourable (i.e. brightness constraints); they can also work independently.

the EPIC camera

The XMM-Newton spacecraft is carrying a set of three X-ray CCD cameras, comprising the European Photon Imaging Camera (EPIC, Turner et al. 2001 and Shruder et al. 2001). Two of the cameras are MOS (Metal Oxide Semi-conductor) CCD arrays (referred to as the MOS cameras). They are installed behind the X-ray telescopes that are equipped with the gratings of the Reflection Grating Spectrometers (RGS). The gratings divert about half of the telescope incident flux towards the RGS detectors such that (taking structural obscuration into account) about 44% of the original incoming flux reaches the MOS cameras. The third X-ray telescope has an unobstructed beam; the EPIC instrument at the focus of this telescope uses pn CCDs and

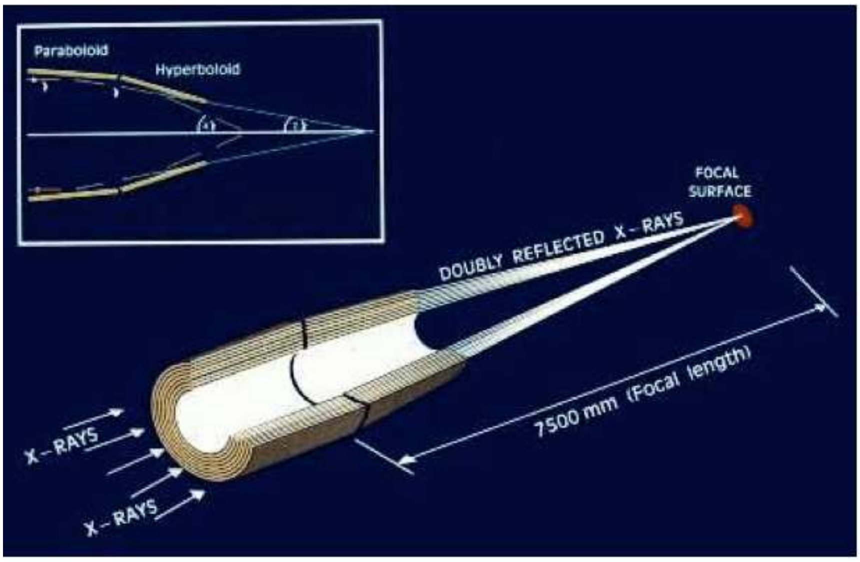

Figure 2.5: The light path in *XMM-Newton*'s open X-ray telescope with the pn camera in focus (not to scale; from the *XMM-Newton* User's Handbook).

is referred to as the pn camera. The EPIC cameras offer the possibility to perform extremely sensitive imaging observations over the telescope's field of view (FOV) of 30 arcmin and in the energy range from 0.15 to 15 keV with moderate spectral and angular resolution.

All EPIC CCDs operate in photon counting mode with a fixed, mode dependent frame read-out frequency, producing event lists, i.e. tables with one entry line per received event, listing (among others) attributes of the events such as the position at which they were registered, their arrival time and their energies. The two types of EPIC, however, differ in some major aspects. This does not only hold for the geometry of the CCD arrays and the instrument design but also for other properties, like e.g., their readout times.

A sketch of the detector layout and the baffled X-ray telescope FOV of the EPIC MOS and pn cameras is shown in figure 2.6.

The two MOS and the pn CCDs operate in photon counting mode, producing an event list which contains every detected photon, its attributes (i.e. x/y position), its arrival time and its energy.

The MOS chip array consists of 7 individual, front illuminated identical CCDs, offset with

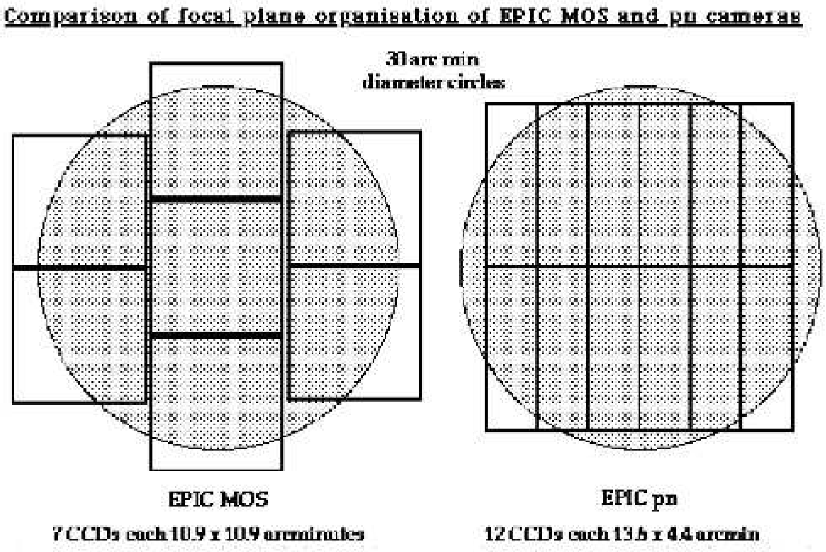

Figure 2.6: A sketch of the field of view of the EPIC MOS and pn cameras. The shaded circle detects a 30′ diameter area (from the *XMM-Newton* User's Handbook).

respect to each other, and each made of 600×600 pixels. The imaging area is $\sim$2.5×2.5 cm^2, so that a mosaic of seven images (1 for each CCD) covers the entire focal plane (62 mm in diameter, corresponding to 28.4′). The pn camera is composed of a single silicon wafer with 12 integrated CCD chips, each made of 64×189 pixels. The EPIC cameras allow several mode of data acquisition.

The observer can also choose to employ an optical blocking filter in the low energy part of the passband, influencing the EPIC effective area. The need for using filters is due to the fact that the EPIC CCDs are also sensitive to infrared, visible and UV light. Indeed, if a source has a high optical flux, the X-ray signal might be contaminated by the optical photons, giving problems when analysing the data. In order to avoid any problem during data analysis, the EPIC cameras are equipped with aluminised optical blocking filters; there are three types of filters: thick, medium and thin.

As far as the background is concerned, in the EPIC cameras it is essentially made of two components, one due to the cosmic X-ray background and one instrumental. The instrumental background is then divided in two: a component due to the detector noise (important below 0.2 keV) and one due to particles interacting with the satellite or the detectors themselves (important above a few keV). Again, the particle induced background can be further subdivided in two more components: an external flaring component with a strong and rapid variability, and a second internal component. The flaring component can be caused by soft photons, funneled towards the detectors by the mirrors. The internal component can be ascribed to high energy particles interacting with the satellite structure and the detectors.

In the EPIC cameras the centre of the on-axis PSF is narrow and does not vary much over a wide energy range (0.1-4 keV); above 4 keV the PSF is only slightly energy dependent. The PSF is not the same for all the detectors, but it varies from $12.5''$ for the pn to $\sim 4''$ for the two MOS cameras. Extended sources in the centre of the FOV could be observed with a spatial resolution of $5''$. One of the problems that can affect the PSF is when pile-up occurs (i.e. when two X-ray photons simultaneously hit the same pixel) and the count rate exceeds a few counts per frame. Another factor affecting the PSF is its dependence on the off-axis angle.

In the analysis of the EPIC observations, all these effect, need to taken into account for a proper treatment of data and a reliable production of source images, spectra and light curves.

2.3 Optical ground based telescopes

Optical spectroscopic work was performed by means of multisite observational campaigns involving a number of different telescopes located in Europe, North-Central, South America and also in South Africa; we also used archival spectra available on line. In the following we give a full list of the optical telescopes used in this thesis and provide a brief description of their main characteristics; the list follows the increasing diameter of each telescope.

Figure 2.7: The Cerro Tololo Inter-American Observatory, Cerro Tololo, Chile.

2.3.1 Cerro Tololo Inter-American Observatory (CTIO)

The Cerro Tololo Inter-American Observatory (see Fig.2.7) is located about 500 km north of Santiago, Chile, about 70 km east of La Serena, at an altitude of 2200 meters. CTIO operates the 4-m Blanco telescope on Cerro Tololo, and the new 4.1-m SOAR Telescope, which is on the adjacent Cerro Pachon, next to the 8-m Gemini Telescope. The CTIO 1.5-m, 1.3-m and 0.9-m telescopes, and the Yale 1.0 m telescope are being operated by the SMARTS Consortium.

For our campaign we use the 1.5-meter telescope mounted on an asymmetrical, off-axis mounting and used on the east side of the pier. It is not possible to reverse the telescope over the pier. All Cassegrain instruments are mounted on an instrument rotator, and thus they may be placed at any position angle on the sky. The instrument we use during our campaigns is the R-C spectrograph, assuming the Grism #13, covering a range of 4000-8000 Å with a slit width matched to the seeing. (`http://www.ctio.noao.edu/telescopes`).

2.3.2 1.52m ‘Cassini’ telescope of the Astronomical Observatory of Bologna

The telescope is located at Loiano, near Bologna. It was designed by the French firm REOSC. Its structure is very different from that of a classic telescope (see Fig.2.8): there is no tube, and the optics are supported by an iron framework. Counterweights balance the telescope, in order to minimize the stress which could compromise pointing and tracking accuracy. The optical system is formed by a main mirror with a diameter of 152 cm, with a central hole, and by a secondary mirror with a diameter of about 60 cm. The secondary mirror is located in front of the main mirror at a distance of 4m, and reflects the light through the hole, into the observing instruments. REOSC also designed the dome, which was built by Comeva of Vicenza. The Ritchey - Chretien optical system has a wide (70-arcminute) corrected field. The building was designed by the Technical Office of the University of Bologna, in a joint project with the Astronomy Department, and relying on the experience developed by REOSC in the Haute Provence (France) and ESO (Chile) buildings. It has 3 floors. The ground floor has a 3.5 m ceiling and was designed to host the mirror-alluminizing equipment. On the first floor are the dark room, with a room for pre-exposure treatment of photographic plates, an office-living room and the control room of the telescope. The second floor hosts the telescope and has a large lifting platform as a general facility during maintenance and observations. The telescope is supported by two concrete pillars, which have independent foundations and no point of contact with the other parts of the building. This prevents that vibrations, produced by the movements of the dome and of the lifting floor, are transmitted to the telescope. The instrument we use during our campaigns is the BFOSC spectrograph plus Grism #4, covering a range of 4000-8000 Å with a slit width matched to the seeing. (`http://www.bo.astro.it/loiano/`).

Figure 2.8: 1.52m ‘Cassini’ telescope, Loiano, Italy.

2.3.3 1.8m ‘Coperinicus’ telescope at the Astrophysical Observatory of Asiago

The telescope, inaugurated in 1973 and dedicated to N. Copernicus, is a classic Cassegrain reflector with a primary mirror of 182cm (see Fig.2.9). It is the main observing facility at the observing site of Cima Ekar (1350 m). It is also the largest astronomical telescope in Italy.

At the 182cm telescope two instruments are available: a low resolution spectrograph and imager (AFOSC) and an high resolution spectrograph (Echelle). The two instruments are complementary for spectral resolution and are therefore mounted in turn at the telescope following the moon cycle (AFOSC being usually available during grey and dark time). For our spectroscopic campaign we use the Asiago Faint Object Spectrograph and Camera (AFOSC) plus Grism #4, covering a range of 3500-7500 Å with a slit width matched to the seeing. It is a focal reducer type spectrograph/camera twin of DFOSC, the instrument installed at Danish 1.54 m telescope at la Silla. It is installed at the Cassegrain focus of the 182 cm telescope. This enables imaging, spectroscopy, a resolution accuracy of 240 up to 3600, and polarimetry, to be performed (`http://www.pd.astro.it/asiago/`).

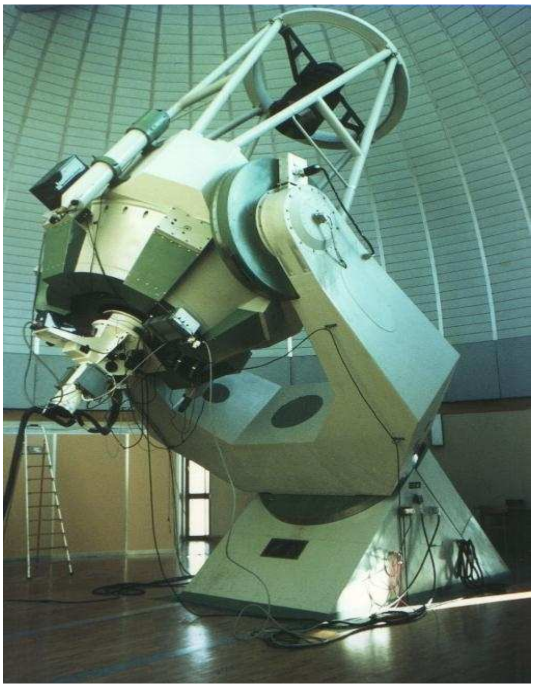

Figure 2.9: 1.8m ‘Coperinicus’ telescope at the Astrophysical Observatory of Asiago, Italy.

2.3.4 1.9m ‘Radcliffe’ telescope at the South African Astronomical Observatory (SAAO)

This telescope was built by Grubb Parsons in 1938-48 for the Radcliffe Observatory, which is near Pretoria (see Fig.2.10). It has a 2-pier asymmetrical mounting. All observing is done with the telescope East of the polar axis; the telescope can no longer be used West of the pier.

The grating spectrograph is available only on the 1.9-m telescope. It employs a SITe CCD chip, using an f/2.2 camera with an 86 mm beam. Most spectrograph functions are automated and are operated from the warm room. Grating angle adjustment, slit width adjustment, comparison beam filters and arc lamp insertion are not automated. The star is acquired viewing the sky via a 45° mirror, which is then moved to permit light to reach the slit area, which is viewed via a transfer lens. The instrument we use during our campaigns is the SpCCD spectrograph plus Grism #7, covering a range of 3500-7500 Å with a slit width matched to the seeing (`http://www.saao.ac.za/home/`).

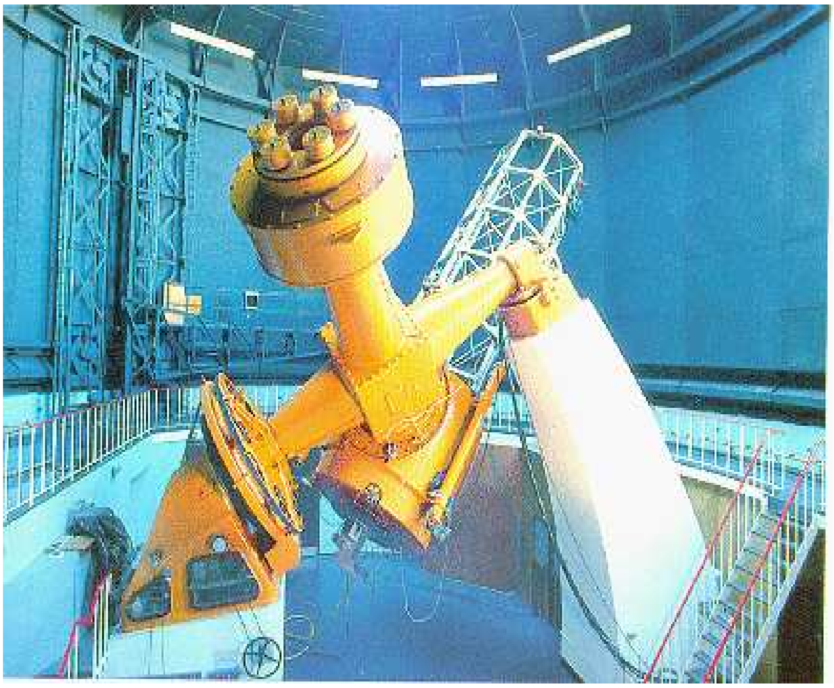

Figure 2.10: 1.9m ‘Radcliffe’ telescope, Sutherland, South Africa.

2.3.5 2.1m telescope of the Observatório Astronómico Nacional in San Pedro Martir

The Observatorio Astronómico Nacional at San Pedro Martir (see Fig.2.11) is located 31° 02’40” N and 115° 28’ 00” W on the summit of the Sierra San Pedro Martir in the Baja California peninsula, Mexico, at 2800 m above sea level. At present, it operates three Ritchie-Chrétien telescopes of diameters 0.84-m, 1.5-m and 2.1-m.

The largest of the telescopes currently at San Pedro Martir, the one used in this thesis (2.1 meters telescope) was constructed between 1974 and 1979, dedicated on September 17, 1979. It has a Ritchey-Chretien design, the dome slit has two segments that can be displaced up or down (1 or both segments) depending on the observed region. It is used for optical spectroscopy from low to high resolution. The instrument we use during our campaigns is the Boller & Chivens spectrograph, covering a range of 3500-7800 Å with a slit width matched to the seeing (`http://www.astrossp.unam.mx/Telescopes/telescopes.html`).

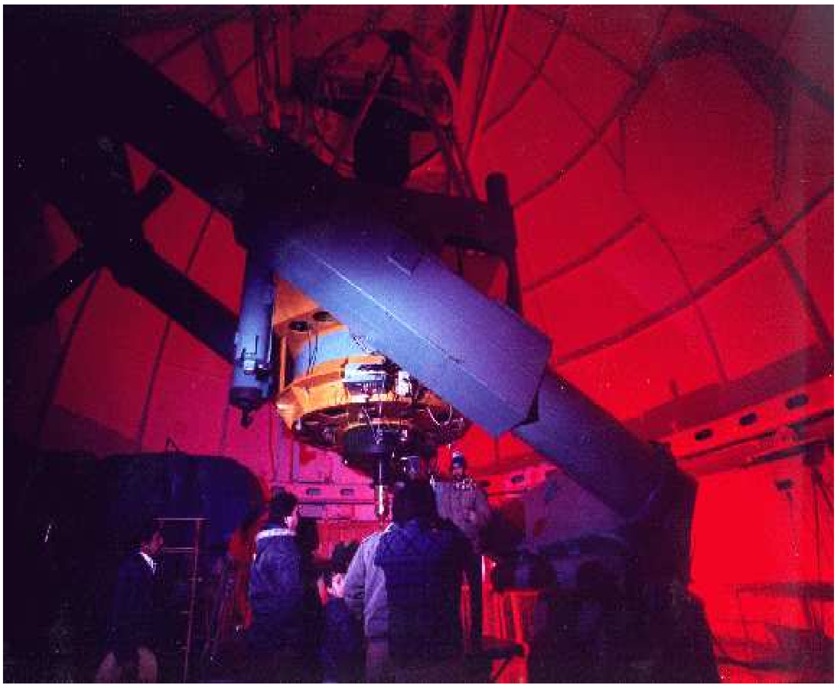

Figure 2.11: 2.1m telescope of the Observatório Astronómico Nacional in San Pedro Martir, Baja California, Mexico.

2.3.6 2.15m 'Jorge Sahade' telescope at the Complejo Astronomico el Leoncito (CASLEO)

The 2.15m 'Jorge Sahade' telescope is placed in the San Juan Province of Argentina (see Fig.2.12). The observatory was established in 1983 by an agreement between several universities and the Argentinian government. Operations began in 1987 and the complex is now the Argentina national facility for ground-based astronomical observations.

For our campaign we use the REOSC instrument. It is an echelle spectrograph that belongs to the Institute d'Astrophysique de Liege in Belgium. It is an instrument able to work from 3500 Å to 7500 Å and in two operating modes: cross-dispersion mode (DC) and single scattering mode (DS). It should be noted that the spectrograph can work beyond the 7000 Å, but it is not designed for it and therefore its efficiency decreases in that range. We used the slit width that match to the seeing (`http://www.casleo.gov.ar/`).

Figure 2.12: 2.15m ‘Jorge Sahade’ telescope at the Complejo Astronomico el Leoncito, Argentina.

2.3.7 3.58m ‘Telescopio Nazionale Galileo’ (TNG) at the Observatory of Roque de Los Muchachos

The Telescopio Nazionale Galileo (TNG) (see Fig.2.13), with a primary mirror of 3.58m, is one of the main national facilities of the Italian astronomical community, and is located at Roque de Los Muchachos Observatory (ORM), in one of the Canarie islands.

It is operated by the Centro Galileo Galilei (CGG) which was created in 1997 by the Consorzio Nazionale per l’Astronomia e l’Astrofisica (CNAA). It has an alt-azimutal mounting. In 2002 it became a part of the Italian National Institute of Astrophysics (INAF) which is ensuring its financial support. TNG is equipped with 5 instruments which are permanently operating on its foci and offer a large variety of observing modes covering the optical and near infrared wavelength ranges and spanning from broad band imaging to high resolution spectroscopy. Our optical spectra come from DOLORES (Device Optimized for the LOw RESolution), LRS in short, a low resolution spectrograph and camera permanently installed at the Nasmyth B focus

Figure 2.13: ‘Telescopio Nazionale Galileo’ (TNG), Roque de Los Muchachos, Spain.

of the Telescopio Nazionale Galileo. We use the Grism LR-B that covers a range of 4000-8000 Å with a slit width matched to the seeing. Its design allows to perform imaging and low resolution spectroscopy observations. The instrument is based on a collimator and on a focal reducer and camera (`http://www.tng.iac.es/`).

2.3.8 3.58m NTT of the European Space Observatory (ESO)

The ESO New Technology Telescope (NTT) (Fig.2.14), is a 3.58m Richey-Chretien telescope which pioneered the use of active optics. The telescope and its enclosure had a revolutionary design for optimal image quality. It is located at La Silla, Chile.

The ESO New Technology Telescope, NTT, was commissioned in 1989, and completely upgraded in 1997. It has an alt-azimutal mounting, and two Nasmyth foci, which host two instruments. SOFI is mounted on Nasmyth A, while since 21 June 2008 EFOSC2 is mounted on Nasmyth B. The pointing error is about 1.5” RMS, but degradation occurs close to zenith and at

Figure 2.14: 3.58m European Space Observatory (ESO), La Silla, Chile.

zenith angle larger than 60 degrees. The pointing is limited to 70deg. zenithal distance, and 3 degrees from zenith. The NTT has a rigid construction due to the reduced mass of the primary mirror and telescope structure compared with classical telescopes. This results in a very accurate pointing of 1.5” r.m.s. over most of the sky. The instrument we use during our campaigns is the EFOSC2 spectrograph plus Grism #13, covering a range of 4000-8000 Å with a slit width matched to the seeing (`http://www.eso.org/sci/facilities/lasilla/telescopes/ntt/`).

2.3.9 4.2m ‘William Herschel’ Telescope (WHT)

The William Herschel Telescope (Fig.2.15), inaugurated in 1987, is one of the largest optical telescopes of its kind in Europe, with a primary mirror of diameter 4.2 m. Its state-of-the-art instrumentation together with the superb sky quality of the Roque de Los Muchachos Observatory

Figure 2.15: 4.2m 'William Herschel' Telescope (WHT) at the Observatory of Roque de Los Muchachos (Canary Islands, Spain).

have made the William Herschel Telescope one of the most scientifically productive telescopes in the world.

The William Herschel Telescope is of classical Cassegrain optical configuration. The paraboloidal primary mirror is made of a glass-ceramic material (Cervit) having near-zero coefficient of expansion over the operating temperature range. It has a clear aperture of 4.2 m and a focal length of 10.5 m (f/2.5). The mirror is a solid piece, with no empty cells to reduce the weight. The instrument we use during our campaigns is the ISIS spectrograph plus Grism R158R, covering a range of 4500-8500 Å with a slit width matched to the seeing (`http://www.ing.iac.es/Astronomy/tele`

2.4 Sloan Digital Sky Survey (SDSS)

The SDSS survey is one of the most powerful survey available now. It obtained deep, multi-color images covering more than a quarter of the sky and created 3-dimensional maps containing more than 930,000 galaxies and more than 120,000 quasars. This survey use a 2.5m telescope sited in

New Mexico at the Apache Point Observatory. The camera mounted on this telescope is able to observe 1.5 square degrees of sky.

During its first phase of operations, 2000-2005, the SDSS imaged more than 8,000 square degrees of the sky in five optical bandpasses, and it obtained spectra of galaxies and quasars selected from 5,700 square degrees of that imaging (http://www.sdss.org/).

2.5 Six-degree Field Galaxy Survey (6dFGS)

The 6dF is a powerful near-infrared-selected redshift and peculiar velocity survey that is complete to over 83% of the southern sky. The observations for this survey were carried out using the Six Degree Field (6dF) fibre-fed multi-object spectrograph at the UK Schmidt Telescope (UKST) over 2001 May to 2006 January (Jones et al. 2004). Target fields covered the $\sim$ 17000 deg of southern sky more than 10° from the Galactic Plane. Over the next 6 years, it mapped nearly the entire southern sky, observing over one hundred thousand galaxies (http://www.aao.gov.au/local/www/6df/).

Chapter 3

Optical follow-up of unidentified hard X-ray selected sources

3.1 Introduction

A number of surveys at energies higher than 10 keV are now available to study the high energy sky. Indeed the surveys performed by IBIS on board *INTEGRAL*, together with those made by BAT on board *Swift*, provide the best sample of objects selected in the hard X-ray band to date (Bird et al. 2010, Krivonos et al. 2010, Cusumano et al. 2010). As already mentioned IBIS and BAT work in similar spectral bands, but concentrate on different parts of the sky: IBIS maps mainly the Galactic plane, while BAT focuses on observations at high Galactic latitudes.

The nature of the sources detected in these surveys is often not confirmed and sometimes just speculated on the basis of their X-ray characteristics; therefore an optical follow-up work of these sources is mandatory. The optical spectra are not only crucial for an accurate classification, but can provide fundamental parameters which together with the X-ray data, can give us fundamental information on these sources.

In this thesis we have selected from the surveys of Cusumano et al. (2010) for BAT and of

Bird et al. (2010) and Krivonos et al. (2010) for IBIS, those objects either without optical identification, not well studied or without published optical spectra. Following the method applied by Masetti et al. (2004, 2006a,b, 2008, 2009) for the optical spectroscopic follow-up of unidentified *INTEGRAL* sources, we determine the nature of 148 selected objects which are listed in Table 3.5.

We show here the spectroscopic results obtained on this sample at various telescopes, thanks to an observational multisite campaign carried out in Europe, North, Central and South America, South Africa plus the use of archival spectra available online, pointing out the method used to perform the optical follow-up observations of these hard X-ray sources and the optical results obtained.

3.2 The Identification method

In order to reduce the IBIS and BAT error boxes, correlations with catalogues at longer wavelengths (soft X-ray, optical, near- and far-infrared, and/or radio) are often needed. For example, cross-correlation of the IBIS 20-100 keV catalogue with the ROSAT database (Voges et al. 1999) indicates a high degree of association (Stephen et al. 2005); the association of an IBIS/BAT source to a soft X-ray counterpart provide the positional accuracy to few arcsecs, thus making the optical searches much easier. This correlation analysis can be extended to a number of X-ray catalogues available on-line in the HEASARC archive[1] (Rosat Bright, Rosat faint, XMM Slew etc.). When cross-correlation with X-ray catalogues did not provide a useful association, we had to rely on follow-up X-ray observation either requested or from archival data. For this particular work we have used *Swift*/XRT and *XMM*/EPIC observations as described in the next chapter.

When a soft X-ray observation of the hard X-ray source field was not available, we performed a cross-correlation analysis of the IBIS/BAT survey lists with radio catalogs such as the NVSS

---

[1] *http://heasarc.gsfc.nasa.gov/db-perl/W3Browse/w3browse.pl*

(Condon et al. 1998), SUMSS (Mauch et al. 2003), and MGPS (Murphy et al. 2007) surveys. Finally, we also considered IBIS/BAT objects that contain within their error box a conspicuous galaxy belonging to the 2MASX archive (Skrutskie et al. 2006), or an emission-line object present in the SIMBAD database.

As a result of this work we obtained a list of possible counterparts for each of the IBIS/BAT high energy emitters. All of these counterparts had coordinates known with a precision of few arcsecs (depending on the catalogue/observation used), thus shrinking the search area by a factor of $\sim 10^4$. Within each 90% error box[2], we often found one counterpart, but in some cases more than one. To limit our follow-up work we choose to observe only those associations that were characterized by a single or very few (3 at most) possible optical objects with magnitudes $R < 20$ in the DSS-II-Red survey[3] (see Fig. 3.1 for an idea of the procedure used from the hard X-ray error box to lower energy association (in this case X-ray) and then to the optical counterpart/s). For all of these sources for which optical spectroscopy could be obtained with reasonable signal-to-noise ratio (S/N) at telescopes with diameter smaller than 4 m, the best optical association is recognized by means of the peculiar spectral features observed (basically, the presence of emission lines). All other candidates were excluded because their spectra did not show any peculiarity (in general they were recognized as Galactic stars) and will not be considered further.

Following the above criterion, we optically follow-up 148 objects belonging to the *INTEGRAL*/IBIS and *SWIFT*/BAT surveys and report the results in the following chapter.

3.3 Optical data reduction

The spectroscopic data secured at the various telescopes discussed in the previous chapter were optimally extracted (Horne 1986) and reduced following standard procedures using IRAF (Image

---

[2] In some cases, where the soft X-ray positional error was given at 1σ confidence level, we rescaled it to the corresponding 90% confidence level assuming a Gaussian probability distribution

[3] `http://archive.eso.org/dss/dss`

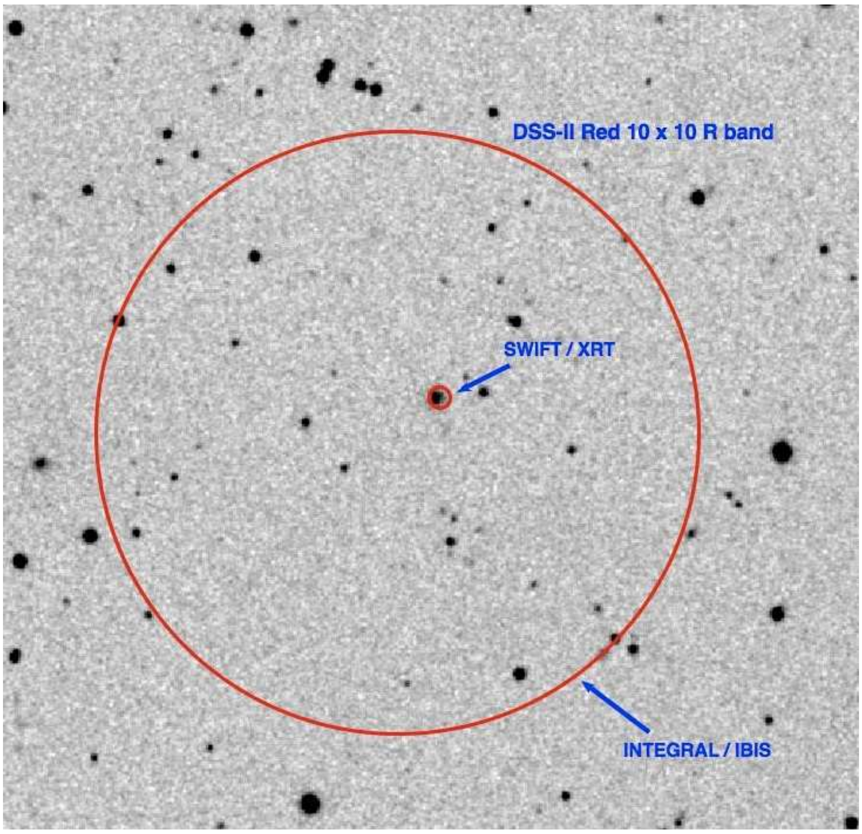

Figure 3.1: The optical image of an *INTEGRAL* source, extracted from the DSS-II-Red survey. The small red circle is the XRT error box ($\sim$ 6 arcsec), while the big one is the IBIS error box ($\sim$ 4 arcmin). It is evident which is the optical counterpart of this hard X-ray source.

Reduction and Analysis Facility). Calibration frames (flat fields and bias) were taken on the day preceding or following the observing night.

There are several steps involved in extracting the optical spectrum of a galactic or extragalactic source in IRAF. In figure 3.2 we report a schematic view of a two-dimensional spectrum (the image obtained after an observation performed by a ground base telescope); the figure shows the dispersion axis along columns and the spatial axis along rows.

To extract a one-dimensional spectrum from a two-dimensional one, we first found the spectrum, examining a cut along the spatial axis and then indicating the object spectrum position. We defined the extraction window and the background windows, by specifying the number of the pixels to the left and to the right of the center of the spatial profile. We did the same for the background region. After that we traced the center of the spatial profile as a function of the dispersion axis, and finally we summed the spectrum within the extraction window, subtracting the sky. At this point we were able to apply the calibration procedures, such as the wavelength calibration and the flux calibration. The wavelength calibration was done, first determining the dispersion solution of the comparison spectrum and then using the dispersion solution to put the object spectrum on a linear wavelength scale. This was obtained using lamps acquired soon after each on-target spectroscopic acquisition; uncertainty on this calibration was $\sim$ 0.5 Å for all cases: this was checked using the positions of background night sky lines. Flux calibration was performed using catalogued spectrophotometric standards. The flux calibration was done observing a spectrophotometric standard star and building a sensitivity function in order to associate a flux value to each pixel.

After these procedures were done we obtained a one-dimensional spectrum, wavelength and flux calibrated.

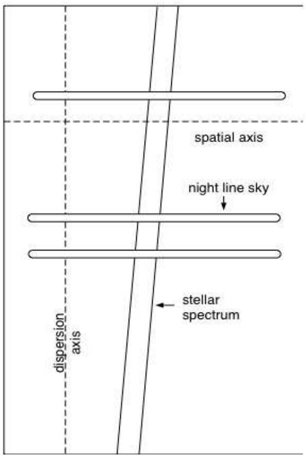

Figure 3.2: A schematic view of a two-dimensional spectrum obtained with a ground base telescope. In figure the main features of this two-dimensional image are reported.

3.4 Classification criteria of optical spectra

We here describe the identification and classification criteria applied for the optical spectra of the 148 sources belonging to the *INTEGRAL*/IBIS (Bird et al. 2010; Krivonos et al. 2010) and *Swift*/BAT (Cusumano et al. 2010) surveys. The optical magnitudes, if not stated otherwise, are extracted from the USNO-A2.0 catalog. To determine the reddening along the line of sight to the Galactic sources of our sample, when possible and applicable, we considered an intrinsic H_α/H_β line ratio of 2.79 (Osterbrock 1989) and inferred the corresponding color excess by comparing the intrinsic line ratio with the measured one by applying the Galactic extinction law of Cardelli et al. (1989). To determine the distances of the compact Galactic X-ray sources of our sample we assumed, for Cataclysmic Variables (CVs) an absolute magnitude $M_V \sim 9$ and an intrinsic color index $(V - R)_0 \sim 0$ mag (Warner 1995), whereas for high-mass X-ray binaries (HMXBs), when applicable, we used the intrinsic stellar color indices and absolute magnitudes as reported in Lang (1992) and Wegner (1994). Although these methods basically provide an order-of-magnitude value for the distance of Galactic sources, as documented in several papers (e.g. Masetti et al. 2004, 2006a, 2006b, 2006c, 2006d, 2007, 2008a, 2008b, 2009, 2010), these estimates are in general correct to within 50% of the refined value subsequently determined with more precise approaches. For the emission-line AGN classification, we used the criteria of Veilleux & Osterbrock (1987) and the line ratio diagnostics of both Ho et al. (1993, 1997) and Kauffmann et al. (2003); for the subclass assignation of Seyfert nuclei, we used the H_β/[O III]λ5007 line flux ratio criterion described in Winkler (1992), and the criteria of Osterbrock & Pogge (1985) for the classification of narrow-line Seyfert 1 galaxies. The spectra of the galaxies shown here (see Appendix A) were not corrected for starlight contamination (see, e.g., Ho et al. 1993, 1997) because of the limited S/N and spectral resolution. In this case, we also do not expect this to affect any of our main results and conclusions. In the following, we consider a cosmology with H_0 = 65 km s^{-1} Mpc^{-1}, Ω_Λ = 0.7, and Ω_m = 0.3; the luminosity distances of the extragalactic objects reported in this thesis were computed for these parameters using the Cosmology Calculator of Wright (2006). In the following sections, we consider all the peculiar object identifications by dividing them into two broad classes, XRBs (including CVs) and AGN listed according to their decreasing distance from Earth. The main observed and inferred parameters for AGN are reported in Tables 3.6, whereas the results of our optical study for CVs and XRBs are instead listed in Table 3.7. In Appendix A we show a large number of spectra for the most interesting sources.

3.5 X-ray Binaries

Twenty seven objects of our sample can be classified as X-ray binaries, given their optical spectral shape and characteristics (see Appendix A), that is, Balmer emission lines at redshift 0 superimposed on an intrinsically blue continuum (in some cases modified by interstellar or local reddening). Table 3.7 collects the relevant optical spectral information about these 27 sources, along with their main parameters (equivalent width and flux for the main lines observed in emission, the optical absorption and the distance) inferred from the available optical data and their classification on the basis of their accretion mechanism and companion star. Of these 27 sources, 18 are CVs and 9 are HMXB (X-ray binaries with an OB type star as companion, where X-ray emission is produced by accretion onto a compact star which passes through an equatorial disk formed by mass loss due to the high spin velocity of the giant companion). The spectra of some sources appear substantially reddened, which is indicative of interstellar dust along their lines of sight. This is quite common in X-ray binaries detected with INTEGRAL (e.g., Masetti et al. 2006b,c,d, 2007, 2008a,b, 2009, 2010). The confirmation of reddening towards these sources comes from either their H_α/H_β line ratio (see table 3.7) or their optical colors.

Particular attention has been devoted to a peculiar source, IGR J19113+1533, that shows optical features similar to IGR J16318-4848 (studied by Filliatre & Chaty 2004); this object is characterised by the presence of [Fe II], H_α and He I in emission in the optical spectrum. We note that, if pointed soft X-ray observations will confirm the association of IGR J19113+1533 with KW97 36-14, this would be the second supergiant B[e]/X-ray binary detected by *INTEGRAL* at hard X-rays. This particular type of X-ray binary has a blue supergiant characterized by forbidden emission lines; it is thought to be in an evolutionary stage intermediate between an OB supergiant and a Wolf Rayet star. Its optical properties have been explained in terms of a two component stellar wind, with the presence of a circumstellar outflowing disk wind (Zickgraf et al. 1985).

3.6 AGN

It is found that 121 out of 148 objects of our sample have optical spectra that allow us to classify them as AGN (see Appendix A for some optical spectra). Table 3.6 lists the relevant optical parameters for these sources: H_α, H_β and [OIII] fluxes, class, redshift, luminosity distance and Galactic color excess. 120 of these AGN exhibit strong, redshifted broad and/or narrow emission lines typical of nuclear galactic activity: 48 of them can be classified as type 1 (broad-line) and 69 as type 2 (narrow line) AGN (see Table 3.6, for their breakdown in terms of subclasses). For

85 AGN in our sample, the redshift value was determined or explicitly published in this thesis for the first time. The redshifts of the remaining sources are consistent with those reported in the literature, i.e., in the Hyperleda[4] (Prugniel 2005) or in the SIMBAD[5] archive. In addition, we slightly corrected the classification of Swift J1473.8-8125 from Seyfert 1.9 (as given in Tueller et al. 2010) to Seyfert 1.2, based on the appearance of its optical spectrum. At this stage, we are unable to say whether this classification mismatch is caused by intrinsic spectral variability of the source in the optical, or due to the different quality of the optical spectra.

3.6.1 XBONGs

In a number of sources, namely IGRJ 02466-4222, Swift J0811.5+0937, IGR J09025-6814 and IGR J17009+3559, the nuclear activity was discovered only thanks to soft X-ray emission detected with *Swift*/XRT, because no emission lines appear in their optical spectra (see Appendix A): we therefore classify them as X-ray bright, optically normal galaxies (XBONG; see Comastri et al. 2002). The 'normal galaxy' nature of these sources are confirmed using the approach of Laurent-Muehleisen et al. (1998). This method uses the Ca II break contrast at 4000 Å (Br4000), as defined by Dressler & Shectman (1987), the presence of other absorption features, such as the G band, the Mg I and the Ca II H+K doublet and the lack of strong Balmer absorption lines, enable us to state that these sources are really 'normal galaxies'. The association of these galaxies with a NVSS radio source (Condon et al. 1998) further points to an AGN nature.

3.6.2 LINERs

LINERs (low ionization nuclear emission-line regions; Heckman 1980) are peculiar AGN, that show particular features in their optical spectra. Their main characteristics are: 1) optical spectra dominated by low ionization state lines: some lines ($[\mathrm{O\,II}]_{\lambda3723}$, $[\mathrm{O\,I}]_{\lambda6300}$, $[\mathrm{N\,II}]_{\lambda6584}$) are stronger

---

[4] `http://leda.univ-lyon1.fr/`

[5] `http://simbad.u-strasbg.fr/simbad/`

than in typical Seyfert 2 galaxies; 2) the permitted emission line luminosities are weak; 3) the emission line widths are comparable with those of Seyfert 2 AGN. Following the above classification criteria we identified, for the first time, LINERs among the unknown-nature hard X-ray sources detected with *INTEGRAL*: they are IGR J10470+2554 and IGR J19118-1707. Two more LINERs, SWIFT J0255.2-0011 and SWIFT J0353.5+3713, were founds among the hard X-ray sources detected by *Swift*/BAT. In particular IGR J10470+2554 appears to display no reddening local to the AGN host. This suggests that this source may be a ‘naked’ LINER. While ‘naked’ Seyfert 2 galaxies, i.e. AGN that lack the broad-line region (BLR) are not unheard (see, e.g., Panessa & Bassani 2002; Bianchi et al. 2008 and Masetti et al. 2008a) the detection of a similar situation in a LINER is quite peculiar, so it is potentially interesting and deserves further study. In three more cases, SWIFT J0041.6+2534, SWIFT J1344.2+1934 and SWIFT J1321.2+0859, the LINER nature cannot be firmly establish. These objects show spectral features that put them in a intermediate place, between Seyfert 2 and LINERs, in the diagnostic diagrams of Ho et al. (1993, 1997) and Kauffmann et al. (2003).

3.6.3 Narrow Line Seyfert 1 AGN

When we examined in detail the optical properties of the AGN sources of our sample, we found the following noteworthy issues for some selected cases. IGR J09094+2735, SWIFT J0923.7+2255 and IGR J16426+6536 can be considered as NLSy1, thanks to their optical characteristics. As already mentioned in section 1.3 they show: 1) full width at half-maximum (FWHM) of the H_β line lower than 2000 km s^{-1}; 2) permitted lines which are only slightly broader than the forbidden lines; 3) the $[\mathrm{O\,III}]_{\lambda 5007}/H_\beta$ ratio < 3; 4) Fe II and other high-ionization emission-line complexes (Osterbrock & Pogge 1985). IGR J00158+5605 could also be classified as a narrow-line Seyfert 1 AGN (NLSy1), given the narrowness of the full width at half maximum (FWHM) of its H_β emission ($\sim$2000 km s^{-1}); however, owing to the absence of the Fe II bumps around 4600 Å and 5200 Å, we opted for a Seyfert 1.5 galaxy classification. Clearly this galaxy needs

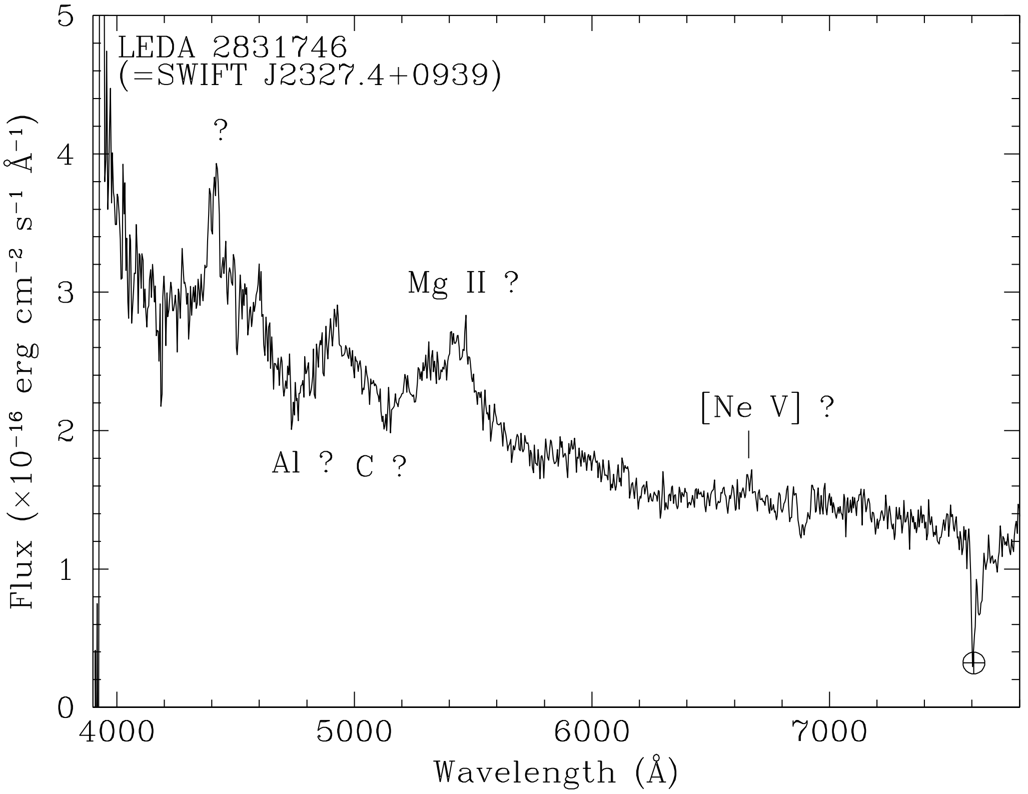

Figure 3.3: Optical spectrum of SWIFT J2327.4+0939, an unidentified source belonging to the *Swift*/BAT survey.

better optical spectroscopy for a definitive classification.

3.6.4 SWIFT J2327.4-2343: very peculiar object

During our classification procedure, we found a peculiar optical spectrum, with optical characteristics not ascribable to any known source typology (see figure 3.3); this object seems to have a Mg II line at a redshift of 0.935 and two lines at 4746 Å and 5137 Å, but it is difficult to understand if they are absorption or emission lines. If they are absorption lines, this source could be a Broad Absorption Line Quasar (BALQSO), with broad high-ionization lines, Al and C in absorption. Unfortunately we do not have the certainty that this is a BALQSO, although the redshift measured suggest that it is an AGN of unclassified type. Other observations in the optical and X-ray band are absolutely essential for better multiwavelength characterization of this AGN.

3.7 Fermi and Chandra follow-up activity

During our follow-up work, we identified and classified two high energy sources not coming form hard X-ray surveys, but from the Fermi and Chandra lists of unidentified objects. The results of our follow-up observations were fundamental for the understanding of both sources and have been fundamental part of the two publications done on each of these sources. Because both results are not related to the main body of the thesis, we choose to add the abstract of both papers as appendix B1 and B2 of the thesis.

3.7.1 Conclusion

We have identified and studied a large number of objects of unknown or poorly explored nature belonging to surveys of the hard X-ray sky (Bird et al. 2010; Cusumano et al. 2010). This has been made possible by using 10 different telescopes sited in the Northern and Southern Hemispheres and archival data from 2 spectroscopic surveys (6dF and SDSS). We reduced and/or analyzed 148 optical spectra of Galactic and extragalactic sources. We found that 121 of them have optical spectral features typical of AGN. Forty eight of these sources exhibit broad and narrow emission lines proper of type 1 AGN, while 69 of them show only narrow emission lines characteristic of type 2 AGN. Inside this extragalactic sample we also found some peculiar AGN, such as 3 NLSy1, that is Seyfert 1 galaxies where the FWHM of the permitted emission lines are slightly broader or comparable to the FWHM of the forbidden narrow emission lines, 4 LINER and 3 objects which have an intermediate classification between LINER and Seyfert 2. The remaining 4 sources do not show signs of any kind of emission lines and we classify them as XBONGs because of their activity at X-ray energies; one object is an AGN of uncertain type.

We found that 27 objects are of Galactic nature; of these 18 are CVs and 9 are X-ray Binaries (HMXBs, sgB[e]). We pointed out the presence of one sgB[e]/X-ray binary, that is a peculiar Be/X-ray binary characterized by the presence of forbidden emission lines (e.g. [Fe II]) related to a circumstellar outflowing spherical disk wind.

The results presented in this chapter demonstrate the high effectiveness of the method of catalog cross-correlation and/or follow-up observations (especially with soft X-ray satellites capable of providing arcsec-sized error boxes, such as Chandra, XMM-Newton or Swift), and optical spectroscopy to determine the actual nature of still unidentified *INTEGRAL* and *Swift* sources. This is a fundamental step if one wants to proceed with population and statistical studies of hard X-ray emitting objects. Within our follow-up activity we have also been able to identify a newly discovered Fermi source and an unidentified Chandra object.

Table 3.1: Log of the spectroscopic observations presented in this thesis. If not indicated otherwise, source coordinates were extracted from the 2MASS catalog and have an accuracy better than 0”.1.

Source	RA (J2000)	Dec (J2000)	Telescope+instrument	λ range Å	UT Date & Time at mid-exposure	Exposure time (s)
IGR J00158+5605	00:15:54.19	+56:02:57.5	Cassini+BFOSC	3500-8700	16 Nov 2009, 19:46	2×1800
IGR J00333+6122	00:33:18.34	+61:27:43.3	WHT+ISIS	5050-10300	05 Jan 2008, 22:51	2×1000
Swift J0034.6−0422	00:34:32.8	−04 24 11	SPM 2.1m+B&C Spec.	3500-7800	11 Dec 2009, 20:14	2×1800
Swift J0038.6+2336	00.38:32.0	+23:36:41	SPM 2.1m+B&C Spec.	3500-7800	20 Sep 2009, 00:19	2×1800
Swift J0041.6+2534	00:41:28.0	+25:29:58	SPM 2.1m+B&C Spec.	3500-7800	29 Jan 2009, 19:17	2×1800
IGR J00465−4005	00:46:20.68	−40:05:49.1	CTIO 1.5m+RC Spec.	3300-10500	12 Sep 2009, 04:22	2×1800
Swift J0059.4+3150	00 59 53.28	+31 49 37.3	SPM 2.1m+B&C Spc.	3450-7650	30 Jun 2008, 10:50	1800
IGR J01054−7253	01:04:42.28	−72:54:03.7	Radcliffe+Gr. Spec.	3850-7200	16 Aug 2009, 03:17	2×1800
Swift J0107.7−1137	01:08:16.1	−11:34:01.5	SPM 2.1m+B&C Spec.	3500-7800	18 Sep 2009, 02:13	2×1800
Swift J0122.3+5004	01:22:34.2	+50:03:18	SPM 2.1m+B&C Spec.	3500-7800	30 Jan 2009, 19:50	2×1800
Swift J0134.1−3625	01 33 57.75	−36 29 35.8	CTIO 1.5m+RC Spc.	3300-10500	02 Jul 2008, 09:02	1200
IGR J01545+6437	01:54:35.29	+64:37:57.5	Copernicus+AFOSC	3500-7800	07 Dec 2008, 22:51	2×1800
Swift J0154.7−2707	01:54:40.2	−27:07:03	SPM 2.1m+B&C Spec.	3500-7800	16 Sep 2009, 02:33	2×1800
Swift J0208.4−7428	02:06:45.17	−74:27:47.7	CTIO 1.5m+RC Spec.	3300-10500	27 Dec 2009, 01:13	2×1200
IGR J02086−1742	02:08:34.95	−17:39:34.8	SPM 2.1m+B&C Spec.	3500-7800	03 Dec 2008, 06:28	2×1800
Swift J0216.3+5128	02:16:26.73	+51:25:25.1	WHT+ISIS	5050-10300	06 Jan 2008, 00:30	2×1800
Swift J0226.7−2819	02:26:25.6	−28:20:55	SPM 2.1m+B&C Spec.	3500-7800	16 Sep 2009, 03:45	2×1800
Swift J0238.3−6118	02:38:41.91	−61:17:21.7	CTIO 1.5m+RC Spc.	3300-10500	17 Nov 2009, 05:12	2×1200
IGR J02466−4222	02:46:37.03	−42:22:01.5	AAT+6dF	3900-7600	30 Aug 2003, 18:06	1200+600
Swift J0248+2626	02:48.59.4	+26:30:39	SPM 2.1m+B&C Spec.	3500-7800	03 Dec 2008, 23:10	2×1800
Swift J0250.3+4645	02:50:25.9	+46:47:28	SPM 2.1m+B&C Spec.	3500-7800	04 Dec 2008, 21:21	2×1800
IGR J02524−0829	02:52:23.39	−08:30:37.5	SDSS+CCD Spc.	3800-9200	23 Dec 2000, 04:07	2700
Swift J0255.2−0011	02:55:12.2	−00:11:01	SPM 2.1m+B&C Spec.	3500-7800	29 Jan 2009, 20:35	2×1800
IGR J03120+5028	03:12:50.1	+50:31:31	Copernicus+AFOSC	3500-7800	18 Sep 2009, 02:44	1800
IGR J03344+1506	03:34:32.77	+15:08:01.2	SPM 2.1m+B&C Spec.	3500-7800	19 Sep 2009, 10:31	2×1800
Swift J0342.0−2115	03 42 03.71	−21 14 39.6	AAT+6dF	3900-7600	30 Nov 2003, 13:34	1200+600
Swift J0347.0−3027	03:47:05.3	−30:23:56	SPM 2.1m+B&C Spec.	3500-7800	20 Sep 2009, 04:21	2×1800
Swift J0350.1−5019	03 50 23.78	−50 18 35.5	CTIO 1.5m+RC Spc.	3300-10500	04 Mar 2008, 01:23	2×1800
Swift J0353.5+3713	03 53 42.5	+37 14 08	SPM 2.1m+B&C Spec.	3500-7800	20 Feb 2009, 14:00	2×1800
IGR J04451−0445	04:44:52.93	−04:46:39.5	SPM 2.1m+B&C Spec.	3500-7800	19 Sep 2009, 11:49	2×1800
IGR J04571+4527	04:57:06.98	+45:27:48.5	SPM 2.1m+B&C Spec.	3500-7800	29 Jan 2009, 07:01	2×1800
Swift J0459.9+2703	04:59:56.2	+27:06:00	SPM 2.1m+B&C Spec.	3500-7800	09 Jun 2009, 09:07	2×1800
Swift J0503.0+2300	05:02:58.2	+22:59:52	SPM 2.1m+B&C Spc.	3450-7650	23 Feb 2009 11:41	2×1800
Swift J0505.7−2348	05:05:45.75	−23:51:14.0	SPM 2.1m+B&C Spc.	3450-7650	03 Feb 2008, 04:04	2×1800
Swift J0519.5−3140	05:19:35.81	−32:39:28.0	AAT+6dF	3900-7600	30 Jen 2003, 10:36	1200+600
IGR J05253+6447	05:24:28.61	+64:44:43.7	Cassini+BFOSC	3500-8700	09 Dec 2009, 22:35	2×1800
RX J0525.3+2413	05:25:22.48	+24:13:31.8	CTIO 1.5m+RC Spec.	3300-10500	29 Feb 2008, 18:36	2×1800
IGR J05270−6631	05:26:14.45	−66:30:45.0	3.6m+EFOSC	3685-9315	02 Jan 2008, 06:19	900
Swift J0535.4+4013	05:35:31.8	+40:11:16	SPM 2.1m+B&C Spec.	3500-7800	09 Jun 2009, 10:15	2×1800
Swift J0543.7−2741	05:43:32.8	−27:39:01	SPM 2.1m+B&C Spec.	3500-7800	03 Dec 2008, 00:42	2×1800
Swift J0544.3+5910	05:44:22.6	+59:07:36	SPM 2.1m+B&C Spec.	3500-7800	04 Dec 2008, 01:17	2×1800
Swift J0544.4−4328	05:44:00.28	−43:25:31.8	CTIO 1.5m+RC Spec.	3300-10500	02 Oct 2009, 00:00	2×1800
Swift J0552.5+5929	05:52:28.0	+59:28:34	CTIO 1.5m+RC Spec.	3300-10500	03 Mar 2009, 09:21	2×1800
Swift j0559.7+5205	05:59:58.9	+52 06 51	SPM 2.1m+B&C Spec.	3500-7800	31 Jan 2009, 20:11	2×1800
IGR J06058−2755	06:05:48.96	−27:54:40.1	CTIO 1.5m+RC Spec.	3300-10500	30 Nov 2009, 02:51	2×1000
IGR J06293−1359	06:29:09.3	−14:04:49	SPM 2.1m+B&C Spec.	3500-7800	05 Dec 2008, 05:38	2×1800
Swift J0640.4−2554	06:40:11.7	−25:53:43	SPM 2.1m+B&C Spec.	3500-7800	04 Dec 2008, 02:17	2×1800
Swift J0640.1−4328	06 40 37.99	−43 21 21.1	CTIO 1.5m+RC Spc.	3300-10500	05 Mar 2008, 1:26	2×1800
IGR J06524+5334b	06:51:59.1	+53:35:00	SPM 2.1m+B&C Spec.	3500-7800	12 Mar 2010, 19:21	2×1800
IGR J06524+5334a	06:52.30.8	+53:31:30	SPM 2.1m+B&C Spec.	3500-7800	13 Mar 2010, 19:29	2×1800
Swift J0654.6+0700	06:54:33.7	+07:03:21	SPM 2.1m+B&C Spc.	3450-7650	14 Mar 2010, 19:09	2×1800
Swift J0727.5−2406	07 27 21.05	−24 06 32.3	TNG+DOLoRes	3800-8000	07 Feb 2008, 23:35	2×1200
Swift J0739.6−3144	07 39 44.69	−31 43 02.5	SPM 2.1m+B&C Spc.	3450-7650	03 Feb 2008, 07:15	2×1800
Swift J0743.0−2543	07 43 14.72	−25 45 50.1	CTIO 1.5m+RC Spc.	3300-10500	04 Mar 2008, 03:56	2×1200
Swift J0746.2−1611	07:46:16.7	−16:11:28	SPM 2.1m+B&C Spc.	3450-7650	11 Mar 2010, 21:44	2×1800
1RXS J080114.6−462324	08:01:17.03	−46:23:27.5	NTT+EFOSC2	3650-9300	01 Jun 2009, 00:31	1200
Swift J0811.5+0937	08 11 30.83	+09 33 50.9	TNG+DOLoRes	3800-8000	08 Feb 2008, 00:51	2×1800
Swift J0814.4+0821	08 14 25.7	+04 20 25	SPM 2.1m+B&C Spc.	3450-7650	20 Jan 2009, 00:56	2×1800
Swift J0820.4−2801	08:20:34.0	−28:05:00	SPM 2.1m+B&C Spec.	3500-7800	13 Mar 2010, 21:23	2×1800
IGR J08262−3736	08:26:13.65	−37:37:11.9	CTIO 1.5m+RC Spec.	3300-10500	30 Nov 2009, 08:18	2×900
Swift J0826.3−7033	08:26:23.5	−70:31:42.5	NTT+EFOSC2	3650-9300	31 May 2009, 23:55	900

Table 3.5: – *continued*

Source	RA (J2000)	Dec (J2000)	Telescope+instrument	λ range Å	UT Date & Time at mid-exposure	Exposure time (s)
IGR J08390−4833	08:38:49.11	−48:31:24.8	CTIO 1.5m+RC Spec.	3300-10500	04 Mar 2008, 05:19	2×1800
Swift J0845.0−3531	08:45:21.38	−35:30:24.2	CTIO 1.5m+RC Spec.	3300-10500	19 Dec 2009, 06:10	2×1800
Swift J0854.7+1502	08:54:29.7	+15:01:36	Copernicus+AFOSC	3500-7800	13 Oct 2007, 03:34	2×1200
Swift J0855.7−2856	08:55:17.4	−28:54:19	SPM 2.1m+B&C Spec.	3500-7800	12 Mar 2010, 04:10	2×1800
IGR J08557+6420	08:55:12.54	+64:23:45.5	SPM 2.1m+B&C Spec.	3500-7800	30 Jan 2009, 07:17	2×1800
Swift J0902.0+6007	09 01 58.37	+60 09 06.2	Copernicus+AFOSC	4000-8000	22 Feb 2008, 21:07	1200+600
IGR J09025−6814	09:02:39.46	−68:13:36.6	CTIO 1.5m+RC Spec.	3300-10500	19 Feb 2007, 06:11	2×1800
Swift J0904.3+5538	09 04 36.97	+55 36 02.6	SDSS+CCD Spc.	3800-9200	29 Dec 2000, 10:48	9000
IGR J09035+5329	09:03:20.8	+53:30:30	SPM 2.1m+B&C Spc.	3450-7650	14 Mar 2010, 23:50	2×1800
IGR J09094+2735	09:09:18.75	+27:37:33.7	SDSS+CCD Spec.	3800-9200	17 Jan 2005, 06:22	2700
IGR J09253+6929	09:25:47.56	+69:27:53.6	Cassini+BFOSC	3500-8700	29 Mar 2008, 21:13	2×1800
Swift J0911.2+4533	09:11:30.00	+45:28:06.0	SDSS+CCD Spc.	3800-9200	07 Feb 2002, 08:24	4803
Swift J0917.2−6221	09:16:09.37	−62:19:29.6	CTIO 1.5m+RC Spc.	3300-10500	04 Mar 2008, 06:02	600
Swift J0917.2−6457	09:17:29.25	−64:56:28.7	CTIO 1.5m+RC Spc.	3300-10500	28 Jan 2010, 00:00	2×1800
Swift J0923.7+2255	09:23:43.01	+22:54:32.4	SPM 2.1m+B&C Spc.	3450-7650	02 Feb 2008, 11:23	1800
Swift J0923.6−2136	09:23:38.8	−21:35:47	SPM 2.1m+B&C Spc.	3450-7650	15 Mar 2010, 22:00	2×1800
Swift J0939.7−3224	09:39:49.74	−32:26:23	SPM 2.1m+B&C Spc.	3450-7650	12 Mar 2010, 22:26	2×1800
Swift J0942.1+2340	09:42:04.5	+23 41 09	SPM 2.1m+B&C Spc.	3450-7650	11 Mar 2010, 23:10	2×1800
Swift J0950.5+7318	09:49:45.96	+73:14:23.2	Cassini+BFOSC	3500-8000	18 May 2009, 20:18	1800
IGR J10147−6354	10:14:15.55	−63:51:50.1	3.6m+EFOSC	3685-9315	02 Jan 2008, 06:44	900
Swift J1017.0−0404	10:17:16.6	−04 04 53	SPM 2.1m+B&C Spc.	3450-7650	30 Jan 2009, 23:56	2×1800
IGR J10470+2554	10:46:42.51	+25:55:53.9	SPM 2.1m+B&C Spec.	3500-7800	03 Dec 2008, 11:51	2×1800
Swift J1049.4+2258	10 49 30.89	+22 57 52.4	Cassini+BFOSC	3500-8000	08 May 2008, 21:17	2×1200
IGR J11098−6457	11:09:47.79	−64:52:45.3	CTIO 1.5m+RC Spec.	3300-10500	04 Mar 2008, 06:44	2×1200
Swift J1115.9+5426	11:15:19.7	+54:23:18	SPM 2.1m+B&C Spec.	3500-7800	20 Jan 2009, 01:16	2×1800
IGR J11225−0419	11:22:24.6	−04:16:10	SPM 2.1m+B&C Spec.	3500-7800	29 Jan 2009, 02:18	2×1800
IGR J11435−6109	11:44:00.3	−61:07:36.5	CTIO 1.5m+RC Spec.	3300-10500	01 Jul 2008, 23:13	2×1200
Swift J1145.3+5859	11:45:33.2	+58:58:41	SPM 2.1m+B&C Spec.	3500-7800	11 Mar 2010, 00:43	2×1800
IGR J11456−6956	11:45:53.62	−69:54:01.8	CTIO 1.5m+RC Spec.	3300-10500	31 Dec 2009, 06:19	2×1800
Swift J1207.5+3355	12:07:32.6	+33:52:42	SPM 2.1m+B&C Spec.	3500-7800	31 Jan 2009, 01:49	2×1800
IGR J12107+3822	12:10:44.28	+38:20:10.2	SDSS+CCD Spec.	3800-9200	13 Apr 2005, 07:12	2300
IGR J12123−5802	12:12:26.24	−58:00:20.5	CTIO 1.5m+RC Spec.	3300-10500	31 Dec 2009, 07:22	2×1800
1ES 1210−646	12:13:14.79	−64:52:30.5	CTIO 1.5m+RC Spec.	3300-10500	04 Mar 2008, 07:26	2×900
IGR J12415−5750	12:41:25.74	−57:50:03.5	CTIO 1.5m+RC Spec.	3300-10500	04 Mar 2008, 08:10	2×1200
Swift J1246.9+5433	12:46:39.9	+54:32:01	SPM 2.1m+B&C Spec.	3500-7800	29 Jan 2009, 3.31	2×1800
IGR J1248.2−5828	12:47:57.84	−58:30:00.2	Radcliffe+Gr. Spec.	3850-7200	13 Aug 2009, 17:56	1800
Swift J1254.8−2655	12:54:56.4	−26:57:04	SPM 2.1m+B&C Spec.	3500-7800	12 Mar 2010, 00:20	2×1800
Swift J1315.1+6042	13:15:42.2	+60:39:44	SPM 2.1m+B&C Spec.	3500-7800	13 Mar 2010, 00:45	2×1800
IGR J13168−7157	13:16:54.28	−71:55:27.1	CTIO 1.5m+RC Spec.	3300-10500	28 Jan 2010, 05:15	2×1200
IGR J13187+0322	13:18:31.24	+03:19:48.9	SDSS+CCD Spec.	3800-9200	22 Jan 2002, 13:07	4800
Swift J1321.2+0859	13:20:59.2	+08:58:45	SPM 2.1m+B&C Spec.	3500-7800	11 Mar 2010, 01:53	2×1800
Swift J1344.2+1934	13:44:15.7	+19:34:00	SPM 2.1m+B&C Spec.	3500-7800	30 Jan 2009, 04:31	2×1800
IGR J13466+1921	13:46:28.5	+19:23:10	SPM 2.1m+B&C Spec.	3500-7800	13 Mar 2010, 02:01	2×1800
Swift J1416.9−1158	14:16:50.0	−11:59:00	SPM 2.1m+B&C Spec.	3500-7800	12 Mar 2010, 01:31	2×1800
IGR J14301−4158	14:30:12.17	−41:58:31.4	AAT+6dF	3900-7600	29 Jun 2003, 12:00	600+1200
Swift J1439.2+1417	14:39:11.9	+14:15:22	SPM 2.1m+B&C Spec.	3500-7800	01 Feb 2009, 04:33	2×1800
Swift J1453.1+2556	14:53:07.9	+25 54 33	SPM 2.1m+B&C Spec.	3500-7800	31 Jan 2009, 05:01	2×1200
Swift J1513.8−8125	15:14:41.92	−81:23:38.0	Radcliffe+Gr. Spec.	3850-7200	13 Aug 2009, 20:37	2×1800
IGR J15311−3737	15:30:51.79	−37:34:57.3	Radcliffe+Gr. Spec.	3850-7200	15 Aug 2009, 19:36	2×1800
Swift J1540.5+1416	15:40:07.8	+14:11:38	SPM 2.1m+B&C Spec.	3500-7800	11 Mar 2010, 03:16	2×1800
Swift J1546.5+6931	15 46 24.33	+69 29 10.0	Cassini+BFOSC	3500-8700	18 May 2009	2×1800
IGR J15549−3740	15:54:46.76	−37:38:19.1	AAT+6dF	3900-7600	12 May 2002, 15:38	1200+600
Swift J1620.5+8103	16:19:19.3	+81:02:48	Cassini+BFOSC	3500-8700	13 May 2009, 22:51	1200
IGR J16287−5021	16:28:27.36	−50:22:42.9	NTT+EFOSC2	3650-9300	31 May 2009, 01:41	1200
IGR J16327−4940	16:32:39.95	−49:42:13.8	Radcliffe+Gr. Spec.	3850-7200	10 Aug 2009, 20:44	2×1800
IGR J16351−5806	16:35:14.1	−58:04:48	Radcliffe+Gr. Spec.	3850-7200	09 Aug 2009, 18:47	2×900
IGR J16426+6536	16:43:04.07	+65:32:50.9	TNG+DOLoRes	3800-8000	04 Feb 2008, 06:11	2×900
1RXS J165443.5−191620	16:54:43.74	−19:16:31.1	SPM 2.1m+B&C Spec.	3500-7800	21 Jun 2009, 06:13	2×1800
IGR J17009+3559	17:00:53.00	+35:59:56.2	Copernicus+AFOSC	3500-7800	16 Oct 2009, 18:04	2×1800
Swift J1733.3+3605	17:33:37.0	+36:31:34	SPM 2.1m+B&C Spec.	3500-7800	14 Mar 2010, 03:09	2×1800

Table 3.5: *– continued*

Source	RA (J2000)	Dec (J2000)	Telescope+instrument	λ range Å	UT Date & Time at mid-exposure	Exposure time (s)
IGR J17404−3655	17:40:26.86	−36:55:37.4	CTIO 1.5m+RC Spec.	3300-10500	02 Jul 2008, 05:36	2×2400
1RXS 175252−053210	17:52:52.0	−05:32:10	SPM 2.1m+B&C Spec.	3450-7650	15 Mar 2010, 03:25	2×1800
IGR J18078+1123	18:07:49.91	+11:20:49.1	SPM 2.1m+B&C Spec.	3500-7800	21 Jun 2009, 18:49	2×1800
IGR J18173−2509	18:17:22.3	−25:08:43	CTIO 1.5m+RC Spec.	3300-10500	02 Jul 2008, 04:04	2×2400
IGR J18249−3243	18:24:55.92	−32:42:57.7	CTIO 1.5m+RC Spec.	3300-10500	04 Mar 2008, 09:21	2×1200
IGR J18308−1232	18:30:49.88	−12:32:18.7	SPM 2.1m+B&C Spec.	3450-7650	29 Jun 2008, 07:49	3×2400
IGR J18308+0928	18:30:50.64	+09:28:41.7	Cassini+BFOSC	3500-8700	18 May 2009, 23:24	2×1200
IGR J18311−3337	18:31:14.75	−33:36:08.5	AAT+6dF	3900-7600	27 Jul 2003, 12:48	1200+600
IGR J19077−3925	19:07:50.36	−39:23:31.9	AAT+6dF	3900-7600	26 Jun 2003, 15:25	1200+600
IGR J19113+1533	19:11:18.83	+15:32:32.8	SPM 2.1m+B&C Spec.	3500-7800	04 Dec 2008, 02:06	1200
IGR J19118−1707	19:11:42.64	−17:10:05.1	AAT+6dF	3900-7600	21 Apr 2004, 18:34	1200+600
1RXS J191928.5−295808	19:19:28.04	−29:58:08.0	AAT+6dF	3900-7600	10 Sep 2002, 10:10	1200+600
IGR J19267+1325	19:26:27.00	+13:22:05.0	SPM 2.1m+B&C Spec.	3450-7650	30 Jun 2008, 06:15	2×2400
IGR J19552+0044	19:55:12.47	+00:45:36.6	Cassini+BFOSC	3500-8700	19 May 2009, 01:58	2×1800
1RXS J211336.1+542226	21:13:35.38	+54:22:32.8	SPM 2.1m+B&C Spec.	3500-7800	22 Jun 2009, 10:21	3×1800
1RXS J211928.4+333259	21:19:29.13	+33:32:57.0	SPM 2.1m+B&C Spec.	3500-7800	04 Dec 2008, 03:12	2×1800
IGR J21347+4737	21:34:20.38	+47:38:00.2	Cassini+BFOSC	3500-8700	11 May 2008, 01:01	2×1800
1RXS J213944.3+595016	21:39:45.1	+59:50:14	SPM 2.1m+B&C Spec.	3500-7800	24 Jun 2009, 10:44	2×1800
Swift J2150.9+1402	21:50:46.8	+14:06:38	SPM 2.1m+B&C Spec.	3500-7800	11 Dec 2009, 19:00	2×1800
IGR J22292+6647	22:29:13.84	+66:46:51.5	TNG+DOLoReS	3800-8000	13 Aug 2008, 01:27	1800
Swift J2254.3+1147	22:54:19.3	+11:46:56	SPM 2.1m+B&C Spec.	3500-7800	16 Sep 2009, 01:22	2×1800
Swift J2319.4+2619	23:19:30.43	+26:15:19.1	SPM 2.1m+B&C Spec.	3500-7800	28 Jun 2008, 09:42	2×1800
Swift J2327.4+0939	23:27:34.0	+09:40:07	SPM 2.1m+B&C Spec.	3500-7800	18 Sep 2009, 01:07	2×1800
Swift J2333.9−2343	23:33:55.2	−23:43:41	SPM 2.1m+B&C Spec.	3500-7800	19 Sep 2009, 07:52	1800
Swift J2341.8+3034	23:41:55.6	+30:34:54	SPM 2.1m+B&C Spec.	3500-7800	03 Dec 2008 , 19:10	2×1800
Swift J2344.9−4245	23:44:44.03	−42:43:21.2	CTIO 1.5m+RC Spec.	3300-10500	23 Sep 2009, 04:19	2×1800
IGR J23524+5842	23:52:22.11	+58:45:30.7	WHT+ISIS	5050-10300	01 Sep 2007, 03:10	2×900

Table 3.6: Main results obtained from the analysis of the optical spectra of the 121 AGNs of the present sample of *INTEGRAL* and *Swift* sources.

Object	F_{H_α}	F_{H_β}	$F_{[\mathrm{OIII}]}$	Class	z	D_L	$E(B-V)_{Gal.}$
IGR J00158+5605	* *	27.7±1.3 [88±4]	30.0±0.9 [94±3]	Sy1.5	0.169	875.5 0.427	
IGR J00333+6122	* *	2.5±0.6 [90±20]	1.76±0.09 [58±3]	Sy1.5	0.105	522.2	1.231
Swift J0034.6−0422	–	1.4±0.5 [1.6±0.6]	17±0.9 [18.7±1.1]	Sy2	0.213	1132.5	0.037
Swift J0038.6+2336	3.7±2.8 [3.8±2.8]	– –	9.3±1.3 [9.2±1.3]	Sy2	0.025	117.5	0.026
Swift J0041.6+2534	11.3±1.9 [13.5±1.9]	– –	– –	Sy2/LINER	0.015	70	0.035
IGR J00465−4005	1.8±0.4 [2.1±0.6]	0.17±0.05 [0.21±0.07]	3.63±0.18 [3.71±0.19]	Sy2	0.201	1061.3	0.011
Swift J0059.4+3150	* *	87±5 [105±6]	37±2 [45±3]	Sy1.2	0.015	84.2	0.061
Swift J0107.7−1137	–	–	13.1±1.4 [12.9±1.4]	Sy2	0.047	224.5	0.024
Swift J0122.3+5004	246±29 [419±32]	50.8±11.6 [101±15]	735±31 [1440±41]	Sy2	0.021	98.4	0.217
Swift J0134.1−3625	9.4±0.3 [9.9±0.4]	in abs. [in abs.]	5.3±2.2 [5.6±2.3]	Sy2	0.029	136.7	0.020
IGR J01545+6437	27±3 [170±20]	2.6±0.3 [41±5]	17.0±0.9 [240±12]	Sy2	0.034	160.9	0.866
IGR J02086−1742	* *	120±12 [126±13]	38.5±1.9 [42±2]	Sy1.2	0.129	651.8	0.028
Swift J0216.3+5128	— —	— —	0.24±0.03 [0.36±0.05]	likely Sy2	0.422	2492.1	0.187
Swift J0226.7−2819	348±35 [244±26]	50.4±13.1 [57.8±13.3]	44.7±3.6 [47.9±3.7]	Sy1.5	0.061	294.4	0.016
Swift J0238.3−6118	– –	– –	7.3±1.9 [7.9±2.1]	Sy2	0.054	259.3	0.023
IGR J02466−4222	in abs. [in abs.]	in abs. [in abs.]	<5.0 [<5.6]	XBONG	0.0695	337.4	0.018
Swift J0248+2626	47±8.6 [64.3±9.1]	3.9±0.9 [6.3±1.3]	21.6±1.6 [34.4±2.1]	Sy2	0.057	274.3	0.158
Swift J0250.3+4645	40.1±2.6 [62.3±2.8]	6.3±1.2 [12.0±1.6]	66.9 ±1.7 [123±3.2]	Sy2	0.021	98.4	0.196
IGR J02524−0829	2.6±0.3 [2.8±0.3]	in abs. [in abs.]	2.4±0.2 [2.7±0.3]	Sy2	0.0168	78.5	0.054
Swift J0255.2−0011	97.4±18.3 [113±18.4]	10±3.2 [12.2±3.3]	25.9±6.5 [29.8±6.5]	LINER	0.0295	139.1	0.072

Table 3.6: *– continued*

Object	F_{H_α}	F_{H_β}	$F_{\mathrm{[OIII]}}$	Class	z	D_L	$E(B-V)_{Gal.}$
IGR J03120+5028	85.9±10.9	11.2±3.2	19.3±2.1	Sy1.5	0.062	299.4	0.745
	[421±64.8]	[170±31]	[179±16]				
IGR J03344+1506	42±2	5.1±0.5	20.7±1.0	Sy2	0.021	98.4	0.316
	[87±4]	[14.0±1.4]	[54±3]				
Swift J0342.0−2115	*	2000±400	400±80	Sy1	0.0139	67.6	0.032
	*	[2700±600]	[460±90]				
Swift J0347.0−3027	112±8.6	11.4±2.2	20.1±1.3	Sy2/HII region	0.095	469.3	0.011
	[118±8.9]	[12.6±2.3]	[20.8±1.4				
Swift J0350.1−5019	38±3	6.9±0.9	11±1	Sy2	0.035	165.8	0.015
	[39±3]	[7.2±0.9]	[11±1]				
Swift J0353.5+3713	35.5±2.8	6±1	12.8±1.6	likely LINER	0.019	88.9	0.536
	[36.7±2.8]	[5±1.2]	[13.2±1.6]				
IGR J04451−0445	5.2±0.5	<0.5	<0.7	likely Sy2	0.076	370.6	0.048
	[5.6±0.3]	[<0.7]	[<0.9]				
Swift J0459.9+2703	37.2±6.6	1.8±0.6	16±1.4	Sy2	0.061	294.4	1.133
	[448±]	[54.5±]	[±]				
Swift J0503.0+2300	699±73	113±22.6	93±7	Sy1.5	0.058	279.3	0.515
	[2670±153]	[600±64]	[436±45]				
Swift J0505.7−2348	38±1	9±1	48±1	Sy2	0.036	172.1	0.040
	[41±1]	[10±1]	[55±1]				
Swift J0519.5−3140	180±20	52±11	320±30	Sy2	0.0126	58.9	0.017
	[190±20]	[59±13]	[350±30]				
IGR J05253+6447	4.5±0.5	in abs.	6.0±0.3	likely Sy2	0.071	345.0	0.190
	[6.7±0.7]	″	[11.1±0.6]				
IGR J05270−6631	—	—	—	Type 1 QSO	0.978	6922.4	0.075
	—	—	—				
Swift J0535.4+4013	133±23.8	20±4.6	31.4±1.8	Sy1.5	0.021	98.4	0.592
	[551±53]	[162± 26]	[31.4±1.8]				
Swift J0543.7−2741	83.9±18.4	107±16.5	22.6±3.1	Sy1.2	0.009	41.8	0.029
	[97.7±18.5]	[112±16.5]	[26.6±3.2]				
Swift J0544.3+5910	3.9±0.4	0.7±0.1	7.1±0.2	Sy2	0.068	329.8	0.274
	[6.4±0.8]	[1.4±0.2]	[15.9±0.8]				
Swift J0544.4−4328	5.4±0.7	1±0.3	4.8±0.4	Sy1.5	0.021	98.4	0.592
	[10.5±1.1]	[2.4±0.2]	[10.8±0.9]				
Swift J0552.5+5929	2280±168	408±61	141±15.2	Sy1.5	0.021	98.4	0.592
	[3500±179]	[724±120]	[246±33]				
Swift j0559.7+5205	150±18.7	14.8±4.9	9.9±3.3	Sy1.5	0.118	591.9	0.223
	[224±28]	[15.2±4.9]	[16±3.6]				
IGR J06058−2755	*	58±6	66±3	Sy1.5	0.090	443.1	0.030
	*	[64±6]	[72±4]				
IGR J06293−1359	34.8±1.7	3.3±0.2	19.0±0.6	Sy2	0.033	156.0	0.323
	[73±4]	[7.4±0.5]	[51.7±1.6]				

Table 3.6: – *continued*

Object	F_{H_α}	F_{H_β}	$F_{[\mathrm{OIII}]}$	Class	z	D_L	$E(B-V)_{Gal.}$
Swift J0640.4−2554	19.5±9	1.5±0.3	23.7±2.3	Sy1.9	0.025	117.5	0.095
	[23.8±9]	[2±0.4]	[31.5±2.3]				
Swift J0640.1−4328	3.1±0.5	0.7±0.3	2.3±0.4	Sy2	0.061	293.9	0.084
	[4.1±0.7]	[3.6±1.7]	[3.0±0.6]				
IGR J06524+5334b	–	–	–	Normal Galaxy	0.062	299.4	0.065
	–	–	–				
IGR J06524+5334a	–	9.1±1.1	3.6±0.2	Sy1.2/1.5	0.301	1678.5	0.062
	–	[10.6±1.6]	[4.0±0.4]				
Swift J0654.6+0700	317±25.5	22.8±5.5	59.1±4.9	Sy1.5	0.024	112.7	0.276
	[590±28]	[62±7]	[137±17]				
Swift J0727.5−2406	*	2.1±0.7	21±1	Sy1.9	0.123	619.0	1.047
	*	[47±7]	[385±17]				
Swift J0739.6−3144	36±2	2.3±0.5	32±1	Sy2	0.026	122.3	0.613
	142±7	[18±4]	[216±5]				
Swift J0743.0−2543	*	11±2	4.5±0.7	Sy1.2	0.023	108.0	0.678
	*	[146±20]	[38±6]				
Swift J0811.5+0937	–	in abs.	–	XBONG	0.286	1582.6	0.026
		[in abs.]					
Swift J0814.4+0821	394±35.3	43.9±7.7	31.9±2.3	Sy1.5	0.034	160.9	0.027
	[433±37]	[49.5± 7.8]	[36.3±5.6]				
Swift J0845.0−3531	*	26.3±1.3	5.4±0.3	Sy1.2	0.137	695.7	0.531
	*	[112±6]	[22.9±1.6]				
Swift J0854.7+1502	7.1±2.1	0.94±0.87	4.9±0.8	Sy2	0.071	345	0.040
	[7.2±0.3]	[1.1±0.8]	[5.5±0.2]				
Swift J0855.7−2856	3.4±0.2	–	–	Sy2	0.073	355.2	0.141
	[4.5± 1.3]						
IGR J08557+6420	6.2±0.4	in abs.	8.8±0.4	likely Sy2	0.037	175.5	0.103
	[7.9±0.6]	″	[12.3±0.6]				
Swift J0902.0+6007	*	52±5	98±5	Sy2	0.012	55.9	0.043
	*	[58±6]	[114±6]				
IGR J09025−6814	in abs.	in abs.	<2.6	XBONG	0.014	63.4	0.101
	[in abs.]	[in abs.]	[<3.8]				
Swift J0904.3+5538	*	30.9±7.9	23.1 ±0.8	Sy1.5	0.0374	177.4	0.021
	*	[36.1±9.9]	[24.5±0.9]				
IGR J09035+5329	0.6±0.2	–	1.6±0.1	Sy2	0.066	319.6	0.015
	[0.6±0.05]		[1.7±0.05]				
IGR J09094+2735	*	4.7±0.3	1.36±0.04	NLSy1	0.2844	1572.4	0.030
	*	[4.8±0.3]	[1.51±0.05]				
Swift J0911.2+4533	4.2±0.2	<0.3	4.4±0.2	Sy2	0.0269	127.1	0.019
	[4.4±0.2]	[< 0.2]	[4.4±0.3]				

Table 3.6: – *continued*

Object	F_{H_α}	F_{H_β}	$F_{[\mathrm{OIII}]}$	Class	z	D_L	$E(B-V)_{Gal.}$
Swift J0917.2−6457	49.8±7.3	8.3±1.4	71.4±2.6	Sy1.9/2	0.086	422.3	0.209
	[85.3±11.2]	[16.6±2.1]	[132±15.9]				
Swift J0917.2−6221	*	1450±40	270±3	Sy1.2	0.057	274.3	0.182
	*	[2380±60]	[518±6]				
Swift J0923.7+2255	*	127±13	92±4	NLSy1	0.034	160.9	0.043
	*	[140±14]	[105±5]				
Swift J0923.6−2136	159±24	6.1±3.9	41.3±2.7	Sy1.5/1.8	0.054		0.290
	[162± 24.3]	[69.5±4.1]	[46±3.4]				
IGR J09253+6929	*	23±5	13.2±0.7	Sy1.5	0.039	185.2	0.290
	*	[55±11]	[31.6±1.6]				
Swift J0942.1+2340	55±19	48.1±11.9	37.1±3.4	Sy1.5	0.022	103.2	
	[81±21]	[70.8±12.4]	[35.8±4.1]				
Swift J0950.5+7318	13.4±2.9	1.6±1.4	26.9±2.6	Sy2	0.058	279.3	0.025
	[13.9±2.9]	[1.1±0.9]	[29.0±2.7]				
IGR J10147−6354	*	37±2	9.8±0.5	Sy1.2	0.202	1067.2	0.314
	*	[81±4]	[21.8±1.1]				
Swift J1017.0−0404	12.4±2.2	1.3±0.7	9.8±0.3	Sy2	0.041	195.0	0.044
	[14.1±1.2]	[1.3±0.4]	[11.4±1.7]				
IGR J10470+2554	21±2	8.2±0.6	15.4±0.8	LINER	0.020	93.7	0.030
	[22±2]	[8.6±0.6]	[17.0±0.9]				
Swift J1049.4+2258	26±1	4.4±0.4	87±1	Sy2	0.033	156.0	0.029
	[29±1]	[4.7±0.5]	[93±1]				
Swift J1115.9+5426	16.8±2.2	1.9±1.1	28±2	Sy2	0.071	345.0	0.013
	[16.5±2.3]	[1.8±0.9]	[28.9±2.4]				
IGR J11225−0419	7±0.6	0.5±0.4	3.2±0.6	Sy2	0.048	229.5	0.056
	[7.9±0.6]	[1.7±0.7]	[3.8±0.7]				
IGR J11456−6956	*	48±2	1.0±0.1	Sy1.2	0.244	1320.2	0.385
	*	[134±7]	[2.4±0.2]				
Swift J1145.3+5858	–	–	–	Type 2 Galaxy	0.008	37.1	0.020
Swift J1207.5+3355	21.3±3.2	3.8±1.1	43.5±1.4	Sy1.5	0.0229	107.5	0.021
	[22.7±3.5]	[4±0.9]	[44.6±2.1]				
IGR J12107+3822	109±7	109±7	64.2±1.9	Sy1.5	0.0229	107.5	0.021
	*	[115±7]	[68±2]				
IGR J12415−5750	*	42±7	88±3	Sy1.5	0.024	113.7	0.609
	*	[300±70]	[588±18]				

Table 3.6: – *continued*

Object	F_{H_α}	F_{H_β}	$F_{[\mathrm{OIII}]}$	Class	z	D_L	$E(B-V)_{Gal.}$
Swift J1246.9+5433	–	–	16.4±4.2 [17.8±4.4]	Sy2	0.017	79.4	0.017
IGR J1248.2−5828	* *	1.1±0.3 [5.8±1.6]	7.8±0.5 [54±4]	Sy1.9	0.028	131.9	0.624
Swift J1254.8−2655	525±65 [660±71]	72.2±29.1 [160±31.1]	72.3±7.3 [103±11.2]	Sy1.5	0.060	289.3	0.075
Swift J1315.1+6042	6.1±0.7 [6.3±0.7]	1.4±0.2 [1.4±0.3]	18.1±3.1 [18.9±3.2]	Sy2	0.132	668.2	0.014
IGR J13168−7157	* *	67±10 [160±20]	47.1±1.4 [103±3]	Sy1.5	0.070	339.9	0.255
IGR J13187+0322	— —	17.2±1.7 [17.2±1.7]	1.5±0.3 [1.5±0.3]	Type 1 QSO	0.6058	3846.2	0.031
Swift J1321.2+0859	60±6.6 [63.8±7.1]	9.9±2.8 [11.5±3.1]	12.6±3.7 [8.7±1.9]	Sy2/LINER	0.033	156	0.029
Swift J1344.2+1934	16.6±1.1 [17.2±1.2]	– –	6.6±0.9 [6.9±0.9]	Sy2/LINER	0.027	127.1	0.025
IGR J13466+1921	147±20 [158±23	30.5±7.6 [28.2±1.7]	12.5±1.9 [13.5±2.1]	Sy 1.2/1.5	0.085	417.1	0.024
Swift J1416.9−1158	132±45 [416±56]	2.8±2 [4.1±1.7]	33.7±4.4 [41.2±2.1]	Sy1.5/1.8	0.099	490.4	0.067
IGR J14301−4158	22.5±1.8 [29±2]	5.7±0.9 [7.6±1.2]	39.6±1.2 [56.1±1.7]	Sy2	0.0387	183.8	0.117
Swift J1439.2+1417	16.5± 3.1 [12.9±3.4]	–	–	Sy2	0.072	350.1	0.019
Swift J1453.1+2556	470±68 [1200±89]	111±22 [115±22.3]	19.7±3.3 [20.6±3.3]	Sy1	0.049	234.4	0.039
Swift J1513.8−8125	* *	103±5 [223±11]	37.3±1.1 [83±2]	Sy1.2	0.069	334.8	0.272
IGR J15311−3737	— —	48±2 [120±4]	6.9±0.3 [16.6±0.5]	Sy1	0.127	640.8	0.320
Swift J1540.5+1416	800±20 18.3 [591±24]	34.1±8.1 [36.3±8.5]	12.2±1.4 [14±1.9]	Sy1.2	0.120	602.8	0.048
Swift J1546.5+6931	181±20 [244±23]	26±4.5 [29±4.8]	97.8±8.6 [113±16]	Sy1.9	0.037	175.5	0.041
IGR J15549−3740	67.7±1.8 [200±6]	7.93±0.12 [36±5]	46±2 [195±10]	Sy2	0.0194	90.8	0.475
Swift J1620.5+8103	24.4±7.5 [27.9±7.8]	2.4±0.8 [4.1±1.5]	19.2±3.9 [23.9±4.5]	Sy2	0.025	117.5	0.046
IGR J16351−5806	360±26 [783±32]	37.2±7.5 [112±13.2]	439±16.7 [1260±58]	Sy2	0.009	41.8	0.335

Table 3.6: – *continued*

Object	F_{H_α}	F_{H_β}	$F_{[\mathrm{OIII}]}$	Class	z	D_L	$E(B-V)_{Gal.}$
IGR J16426+6536	—	1.89±0.09	0.78±0.04	NLSy1	0.323	1821.3	0.021
	—	[2.0±0.1]	[0.81±0.04]				
IGR J17009+3559	—	in abs.	<0.33	XBONG	0.113	565.0	0.018
	—	″	[<0.34]				
Swift J1733.3+3605	6.5±4.2	0.7±0.4	12.9±0.8	Sy2	0.043	204.8	0.041
	[6.6±4.3]	[0.7±0.4]	[14.1±0.9]				
1RXS 175252−053210	166±16.2	15.0±2.6	3.7±0.8	Sy1.2	0.136	690.2	0.995
	[1130±38]	[240±21]	[49.1±4.2]				
IGR J18078+1123	*	64±4	12.6±0.6	Sy1/1.2	0.078	380.9	0.131
	*	[90±6]	[18.6±0.9]				
IGR J18249−3243	*	<0.9	9.6±0.9	Sy1	0.355	2033.2	0.233
	*	[<1.5]	[14.5±1.5]				
IGR J18308+0928	13.1±1.3	<2	16.0±1.6	Sy2	0.019	88.9	0.243
	[26±3]	<4	[33±3]				
IGR J18311−3337	40.2±1.8	6.0±0.6	82±2	Sy2	0.0687	333.3	0.185
	[60±3]	[8.4±0.8]	[141±4]				
IGR J19077−3925	*	4.8±0.7	20.1±1.2	Sy1.9	0.0760	370.6	0.107
	*	[6.2±0.9]	[28.0±1.4]				
IGR J19118−1707	132±4	32±2	83±4	LINER	0.0234	109.9	0.137
	[179±5]	49±3	[126±6]				
1RXS J191928.5−295808	*	42±8	122±6	Sy1.5/1.8	0.1669	863.5	0.139
	*	[56±11]	[183±9]				
1RXS J211928.4+333259	*	10±2	15.2±0.8	Sy1.5	0.051	244.4	0.217
	*	[18±3]	[29.6±1.5]				
1RXS J213944.3+595016	*	3.0±0.2	2.01±0.10	Sy1.5	0.114	570.4	1.271
	*	[112±8]	[72±4]				
Swift J2150.9+1402	41.6±8.1	5.3±1.1	16.1±2.8	Sy2	0.031	146.4	0.131
	[59.7±8.7]	[8.1±1.6]	[26.5±3.2]				
IGR J22292+6647	*	2.25±0.11	1.24±0.06	Sy1.5	0.112	559.6	1.089
	*	[52±3]	[26.3±1.3]				
Swift J2254.3+1147	17.4±5.1	1±0.1	9.7±1.3	Sy2	0.029	136.7	0.093
	[21.4±1.6]	[1.7±0.5]	[11.9±1.3]				
Swift J2333.9−2343	–	–	14.7±2.7	Sy2	0.0475	227.0	0.029
			[16.3±2.8]				
Swift J2341.8+3034	9.7±4.6	–	8.3±2.1	Sy2	0.017	79.4	0.102
	[14.2±5.3]	–	[15.6±2.9]				
SWIFT J2344.9−4245	*	6.9±1.6	62.9±3.6	Sy2	0.112	3778.5	0.017
	*	[64.8±3.7]	[7.2±1.8]				
IGR J23524+5842	—	<0.01	0.06±0.01	likely Sy2	0.164	849.9	1.290
	—	<0.3	[1.9±0.3]				

Table 3.7: Synoptic table containing the main results concerning the X–ray binaries identified or observed in the present sample of *INTEGRAL* and *Swift* sources.

Object	H_α		H_β		He II λ4686		A_V	d	Type
	EW	Flux	EW	Flux	EW	Flux	(mag)	(kpc)	
IGR J01054−7253	7.15±0.15	16.8±0.3	0.47±0.12	2.0±0.5	in abs.	in abs.	∼0.7	60^{b}	B0 III
Swift J0208.4−7428	2.9±0.3	4.5±0.5	in abs.	in abs.	<0.5	<0.2	0.18^{e}	60^{b}	B1 III
IGR J04571+4527	19.4±0.6	10.3±0.3	9.5±0.5	4.8±0.2	3.6±0.4	1.67±0.17	∼0	∼500	CV
1RX J0525.3+2413	9.6 ±0.6	14±0.8	3.5±0.2	6.1±0.5	7.2±0.7	13±0.9	∼0	∼210	CV
Swift J0746.2−1611	35.5±0.9	128±7	32.5±0.8	105±9	19.6±0.5	55.7±5.8	∼0	∼60	CV
1RXS J080114.6−462324	19.9±0.6	7.2±0.2	16.7±0.8	6.5±0.3	9.7±0.7	3.8±0.3	∼0	∼150	CV
Swift J0820.4−2801	51.9±1.2	55.1±3.9	47.7±0.8	60±7.5	12.2±0.5	14.2±2.2	∼0	∼200	CV
IGR J08262−3736	65±2	1050±30	5.5±0.4	96±7	in abs.?	in abs.?	∼3.3	∼6.1	OB V
Swift J0826.3−7033	38.9±1.2	44.1± 4.4	33.6±1.1	44.1±2.9	5.7±1.4	7.4±0.4	∼0	∼90	CV
IGR J08390−4833	27±3	8.6±0.8	8.7±0.9	4.1±0.4	5.2±0.8	2.6±0.4	∼0	∼330	CV
Swift J0939.7−3224	33.3±1.4	19.2±1.2	11.7±0.9	10.9±1.2	6.4±0.4	5.7±1.1	∼0	∼240	CV
IGR J11098−6457	5.2±0.5	8.0±0.8	3.6±0.7	1.9±0.4	<2.0	<1.0	1.23	<20000	CV
IGR J11435−6109	25.8±1.3	39±2	3.5±1.1	2.2±0.7	<2.2	<1.2	5.7	∼8.6	B2 III
1ES 1210−646	in abs.	in abs.	in abs.	in abs.	2.8±0.3	21±2	3.3	∼2.8	B5 V
IGR J12123−5802	20.3±1.0	7.1±0.4	12.7±1.3	5.1±0.5	7.4±0.7	3.5±0.3	∼0	∼190	CV
IGR J16287−5021	52±3	1.75±0.09	19±6	0.23±0.07	15±5	0.16±0.05	3.1	<19	—
IGR J16327−4940	31.3±0.9	370±11	7.6±0.7	3.8±0.4	in abs.	in abs.	11.2	≈2	OB giant
1RXS J165443.5−191620	38.7±1.2	60.9±1.8	18.5±0.9	33.2±1.7	7.5±0.5	13.4±0.9	∼0	∼210	CV
IGR J17404−3655	14.2±0.14	2.5±0.3	<9	<0.9	<6	<0.6	3.1	∼9.1	—
IGR J18173−2509	92±3	25.0±0.8	14.0±1.0	6.9±0.5	7.0±1.0	3.6±0.5	0.73	∼330	CV
IGR J18308−1232	21.9±1.1	7.7±0.4	8.5±0.9	2.2±0.2	3.9±0.9	9.3±2.0	0.67	∼320	CV
IGR J19113+1533	22.5±1.1	159±8	3.6±0.7	5.9±1.2	<1.2	<1.5	7.0	∼9.1	sgB[e]
IGR J19267+1325	63.6±1.9	26.9±0.8	45±3	11.8±0.8	22±2	5.3±0.5	∼0	∼580	CV
IGR J19552+0044	271±8	164±5	264±8	168±5	39±2	60±3	∼0	∼250	CV
1RXS J211336.1+542226	46±2	5.6±0.3	43±3	2.61±0.18	10±2	5.0±1.0	∼0	∼910	CV
IGR J21347+4737	8.1±0.6	5.1±0.4	1.2±0.2	1.2±0.2	1.6±0.4	1.7±0.4	2.2	∼5.8	B3 V
Swift J2319.4+2619	52±2.2	24.8±0.8	46.5±3	29.7±0.2	39.6±2.9	21.1±1.1	∼0	∼210	CV

Note: EWs are expressed in Å, line fluxes are in units of 10^{-15} erg cm^{-2} s^{-1}

Chapter 4

X-ray

4.1 Introduction

In the present chapter, we analyze the X-ray properties of a subsample of objects classified in our optical follow up work discussed in the previous chapter. The sample consists of 94 objects, all AGN of type 1 or 2 for which we have X-ray observations available. In particular we present an X-ray study of 55 *SWIFT*/BAT objects and 39 *INTEGRAL*/IBIS sources (see Table 6.1 and 6.3 respectively). Most of the *SWIFT* objects (34) are AGN of type 2 (note that two sources lie in the borderline region between AGN and LINER or AGN and starburst galaxies), and 15 are of type 1; we consider as type 1 all Seyferts in the range 1-1.5 and as Seyfert 2 all those with higher class (1.8-2). Only in two cases (SWIFT J0923.7-2134 and SWIFT J1416.8-1158) it is difficult to assign the source to one of the two AGN types but in the following we decided to classify these two objects as type 1 also in consideration of their X-ray characteristics (mainly considering their amount of X-ray absorption). As discussed in chapter 2, SWIFT J2327.4+0939 is still unclassified, but we decided to leave it in the sample to better understand its nature and finding some constraints that can help us in defining its class; another source SWIFT J1145.4+5858 is atypical for a Seyfert 2 since we did not detect any permitted emission line, including Hα, in its optical spectrum. Nevertheless, in our discussions we will consider it as a type 2 AGN. Finally we note within the *SWIFT* sample the presence of a couple of peculiar AGNs, namely a LINER and a Narrow Line Seyfert 1 (NLS1); also a type 2 QSO belongs to the sample of *SWIFT* sources. As for the sample of *INTEGRAL* objects, we count 17 AGN of type 2 and 18 of type 1; also in this case we note a few peculiar objects such as two LINERs, one NLSy1 and one XBONG (X-ray bright optical inactive galaxy). The NLSy1 will be treated in the following as type 1 AGN, while all LINERS as well as the XBONG galaxy will be assigned to the type 2 class, since all of them show in their X-ray spectrum absorption in excess to the Galactic one. Although our sample is limited in the number of sources, it could be taken as representative of the population of hard X-ray selected AGN detected both by *SWIFT*/BAT and *INTEGRAL*/IBIS. To show this we have plotted in figures 4.1 and 4.2 the hard X-ray luminosity versus redshift for our objects compared to the samples of AGN reported in the 4th IBIS catalogue (Bird et al. 2010) and in the 54 months Palermo *SWIFT*/BAT catalogue (Cusumano et al. 2010) respectively, i.e. the surveys from which these AGN have been extracted.

It is evident from these figures that our objects are representative of both surveys although they tend to have a slight preference for the brighter part of the AGN population. In any case the considerations that will be done in this work can be taken as characteristic of the whole class of hard X-ray selected AGN.

Most of the sources in our sample were either not known in the X-ray band previously or have been poorly studied at energies below 10 keV, where X-ray observations can be of crucial importance to unveil their properties, define their nature and to quantify the fraction of objects missed by lower energy surveys, such as new Compton thick AGN (see section 1.3.2). Positional location with arcsecond accuracy, which can only be obtained using the capabilities of current X-ray telescopes, is necessary to pinpoint and classify the optical counterpart of these hard X-ray emitters as described in the previous chapter. Furthermore, information in the X-ray band, which is often lacking or inaccurate, is necessary to characterize these sources in terms of spectral

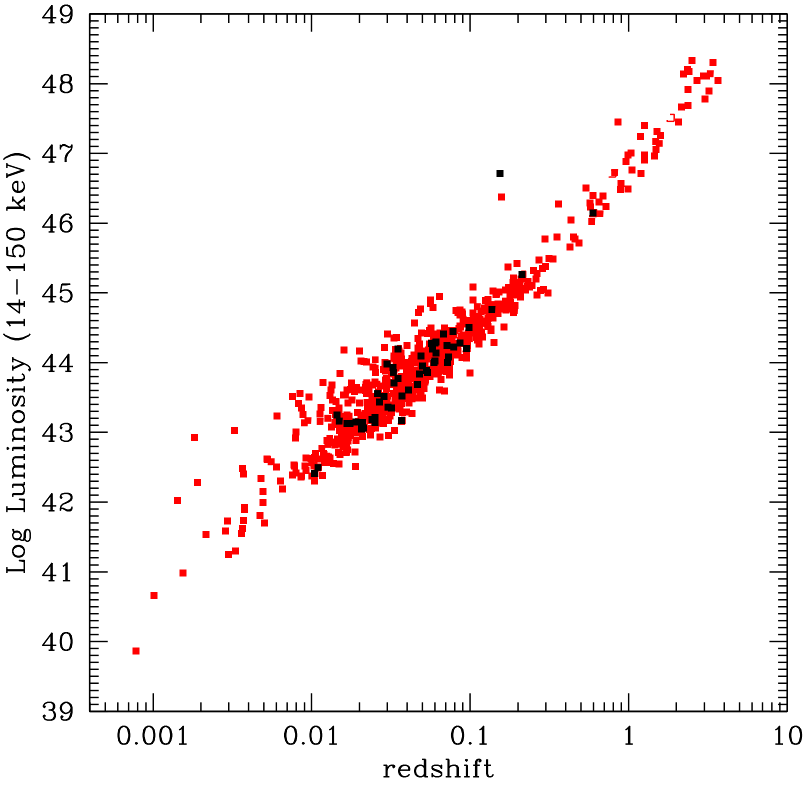

Figure 4.1: Hard X-ray luminosity versus redshift for our *SWIFT* sources (black filled squares) compared to the samples of AGN reported in the 54 months Palermo *SWIFT*/BAT catalogue (red filled squares). This plot shows clear evidence that our AGNs are representative of the sample of AGN in the Palermo catalogue.

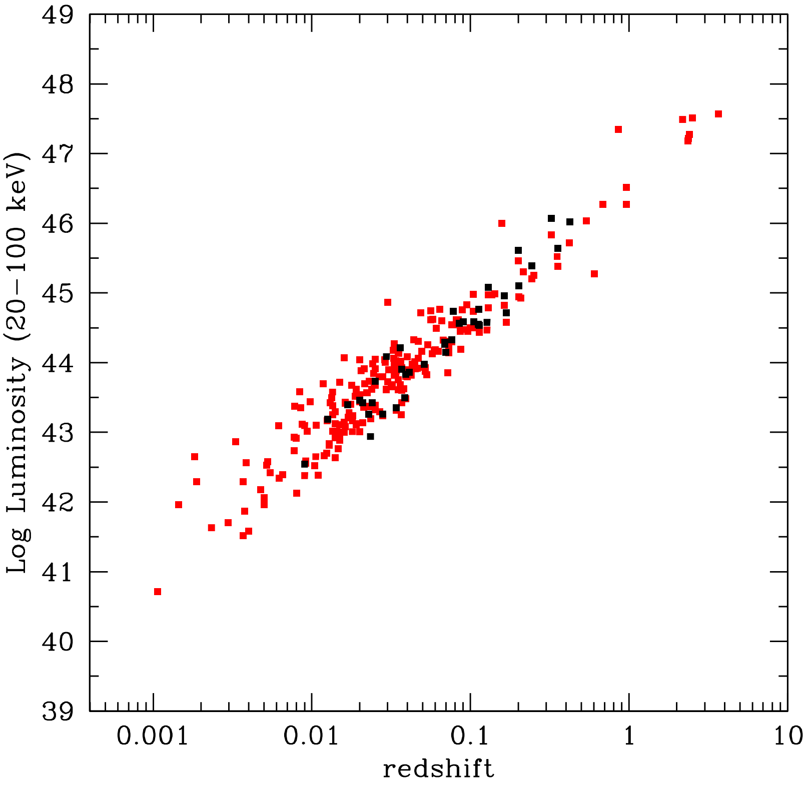

Figure 4.2: Hard X-ray luminosity versus redshift for our *INTEGRAL* sources (black filled squares) compared to the samples of AGN reported in the 4th IBIS catalogue (red filled squares). This plot shows clear evidence that our AGNs are representative of the sample of AGN in the 4th IBIS catalogue.

shape, flux, absorption and variability. In particular, the study of the column density distribution in a sample of AGN selected above 10 keV is important so as to quantify the fraction of objects missed by lower energy surveys, to find new Compton thick AGN or peculiar sources and as an input parameter for synthesis models of the cosmic X-ray background. Furthermore, the X-ray data on our sample of AGN can be compared to their optical properties as obtained in the previous chapter in order to provide a further insight into the problematic of active galaxies: this will be the objective of the next chapter. Ninety four AGN discussed in this chapter have *Swift*/XRT observations available; 9 sources had instead *XMM-Newton* archival data. All these X-ray observations were analyzed first to identify the X-ray and hence the optical counterpart and then to provide X-ray spectral and variability information. In the following sections we will described the data analysis procedure used for both *SWIFT*/XRT and *XMM-Newton*, provide information on the spectral parameters of each object and discuss the overall X-ray properties of our sample.

4.2 Data reduction and analysis

In the following we present the data reduction and analysis of all X-ray observations related to our sample of 94 AGN observed at high energies with the imaging instruments IBIS and BAT respectively on board the *INTEGRAL* and *SWIFT* satellites: information on these observations are given separately for *SWIFT*/BAT and *INTEGRAL*/IBIS sources in Table 6.1 and 6.3. For each source, we report in the first two tables the source name and class, the X-ray instrument used in the observation, the on-source effective exposure, the count rate obtained from the identified X-ray counterpart and the Galactic column density in the source direction. As evident from these tables, the majority of our sources have *SWIFT*/XRT observations available, while only a small set of objects have *XMM-Newton* measurements. Note that in the case of XRT data we have considered only observations where the source was detected with a signal to noise ratio above

5σ, in order to perform a reliable spectral analysis.

4.2.1 SWIFT/XRT Data

For 85 sources in the sample, we use X-ray data acquired with the X-ray Telescope (XRT, 0.3–10 keV, Burrows et al. 2005) on board the *SWIFT* satellite. The XRT data reduction was performed using the XRTDAS standard data pipeline package (XRTPIPELINE v. 0.12.6), in order to produce screened event files. All data were extracted only in the Photon Counting (PC) mode (Hill et al. 2004), adopting the standard grade filtering (0–12 for PC) according to the XRT nomenclature. For each observation we analyzed, with XIMAGE v. 4.5.1, the 0.3–10 keV image to search for sources detected (at a confidence level $> 3\sigma$) within the 90% *INTEGRAL*/IBIS or *SWIFT*/BAT error circles. If more sources were present within these high energy uncertainties, we restricted the image analysis in the 3–10 keV band in order to detect those objects with the hardest spectra (i.e. those with detection above 3 keV), since these are most likely to be the counterparts of the high energy emitting objects. Then, we estimated the X-ray positions using the task XRTCENTROID V.0.2.9 by taking into account the longest pointing for those sources with more than one observation. A few examples of XRT images are shown in figures 4.3 and 4.4 with BAT and IBIS error circles overlapped, respectively; the X-ray positions and relative uncertainties were used to pinpoint the optical counterpart and to perform the optical follow up described in the previous chapter. The X-ray positions are not reported here as they are not very different from the optical positions provided in Chapter 3; as already said all counterparts of the sources discussed here have been found to be associated to AGN as reported in tables 6.1 and 6.3.

Next, we analyzed the spectra of these AGN: events for spectral analysis were extracted within a circular region of radius 20″, centered on the source position; this region encloses about 90% of the PSF at 1.5 keV (see Moretti et al. 2004). The background was taken from source-free regions close to the X-ray source of interest, using circular regions with different radii in order to ensure an evenly sampled background. The source spectrum was then extracted from the

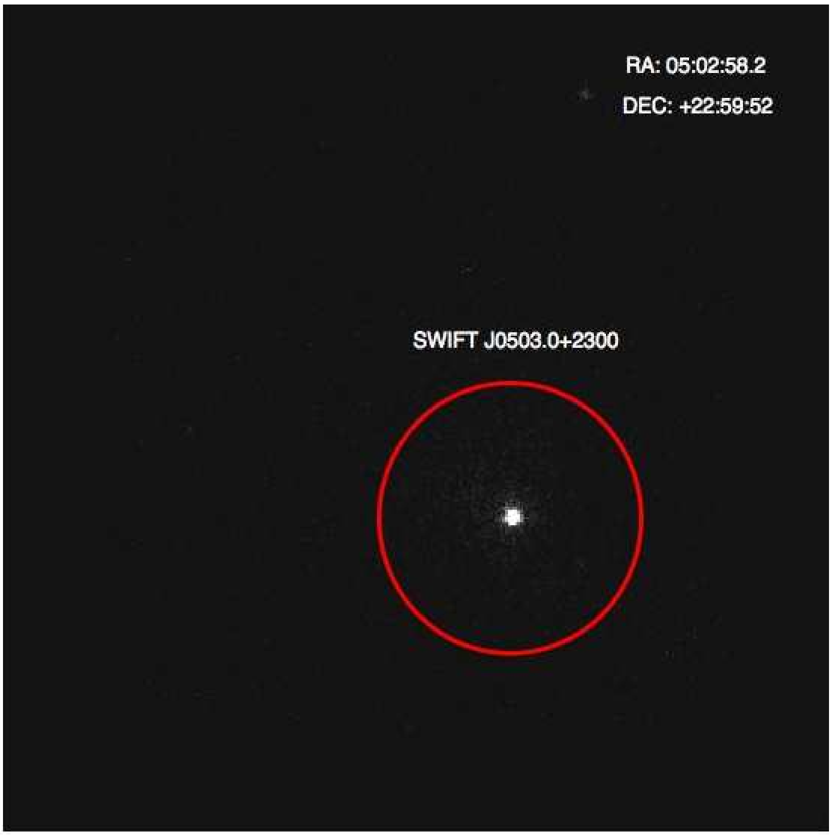

Figure 4.3: XRT image of a *SWIFT*/BAT source, SWIFT J0503.0+2300. It is obtained with XIMAGE in the energy range 0.3-10.0 keV. The red circle shows the BAT error box of radius 4.11'

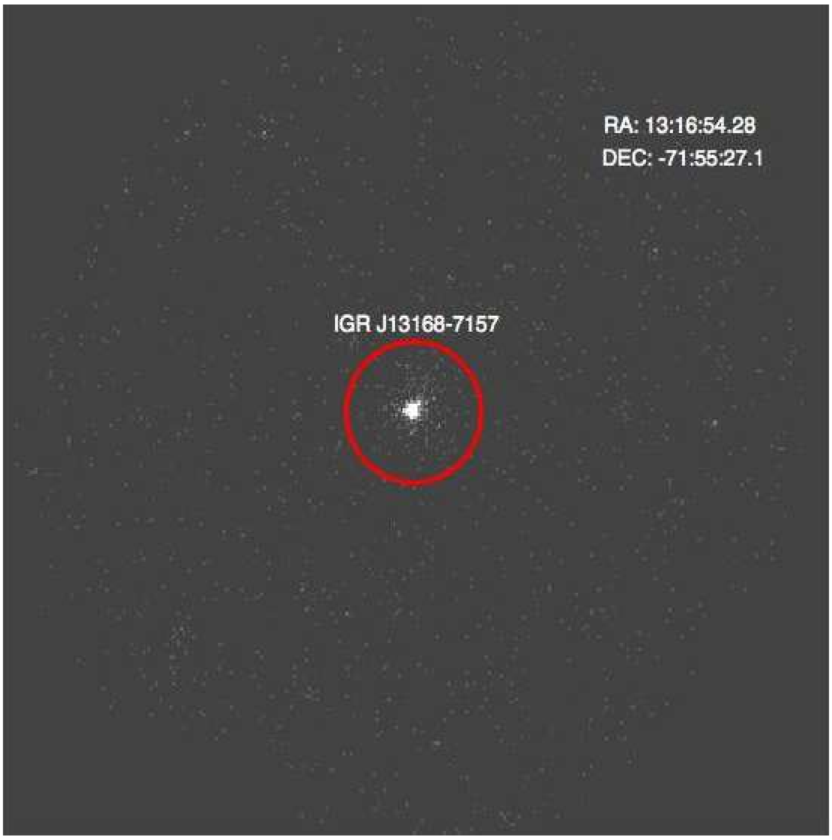

Figure 4.4: XRT image of an *INTEGRAL*/IBIS source, IGR J13168-7157. It is obtained with XIMAGE in the energy range 0.3-10.0 keV. The red circle shows the IBIS error box of radius 2.1’

corresponding event file using the XSELECT V.2.4 software and binned using GRPPHA in an appropriate way, so that the χ^2 statistic could be applied. We used version v.011 of the response matrices and created the relative ancillary response file *arf* using the task XRTMKARF V.0.5.6. The energy band used for the spectral analysis, performed with XSPEC v.12.6.0, depends on the statistical quality of the data and typically ranges from 0.3 to $\sim$6 keV. For objects with more than one pointing available, we either used the longest observation available or we summed together all measurements; this was done in order to improve the statistics and have a reliable estimate of the source spectral parameters. In the first instance, we adopted, as our basic model, a simple power law passing through Galactic absorption (Dickey & Lockman 1990). If this baseline model was not sufficient to fit the data, we introduced extra spectral components as required according to the F-test statistics. Note that in many cases due to the limited statistical quality of the XRT data we have fixed the photon index to 1.8 in order to estimate the intrinsic column density and/or the X-ray flux. The results of this analysis are reported in Tables 6.2 and 6.4, where we list the column density in excess to the Galactic value, the power law photon index, the reduced χ^2 of the best-fit model and the 2–10 keV flux; extra spectral parameters if required are reported in the notes at the end of the Tables. All quoted errors correspond to a 90$\%$ confidence level for a single parameter of interest ($\Delta\chi^2 = 2.71$).

4.2.2 XMM-Newton data

For 9 sources in our sample, we use instead X-ray data acquired with the pn X-ray CCD camera on the EPIC instrument on-board the *XMM-Newton* spacecraft (Struder et al. 2001).

XMM data were processed using the Standard Analysis Software (SAS) version 9.0.0 employing the latest available calibration files. Only patterns corresponding to single and double events (PATTERN$\leq$4) were taken into account and the standard selection filter FLAG=0 was applied. The observations were filtered for periods of high background and the resulting net exposures for each source are reported in Table 6.2 and 6.4. For each observation, we analyzed the *XMM-Newton* EPIC-pn images to search for X-ray sources which fall inside the IBIS/BAT error boxes and are therefore likely counterparts of the high energy emitters. As in the case of XRT observations, a couple of examples of XMM images are shown in figures 4.5 and 4.6 with BAT and IBIS error circles overlapped; the X-ray positions and relative uncertainties were used to pinpoint the optical counterpart and to perform the optical follow up described in the previous chapter. Also the X-ray positions obtained from *XMM* are not reported here as they are practically coincident with the optical positions provided in Chapter 3; as already said all counterparts of the sources discussed here have been found to be associated with AGN. Next we obtained X-ray spectra in the 0.5-12 keV band of the likely associated source.

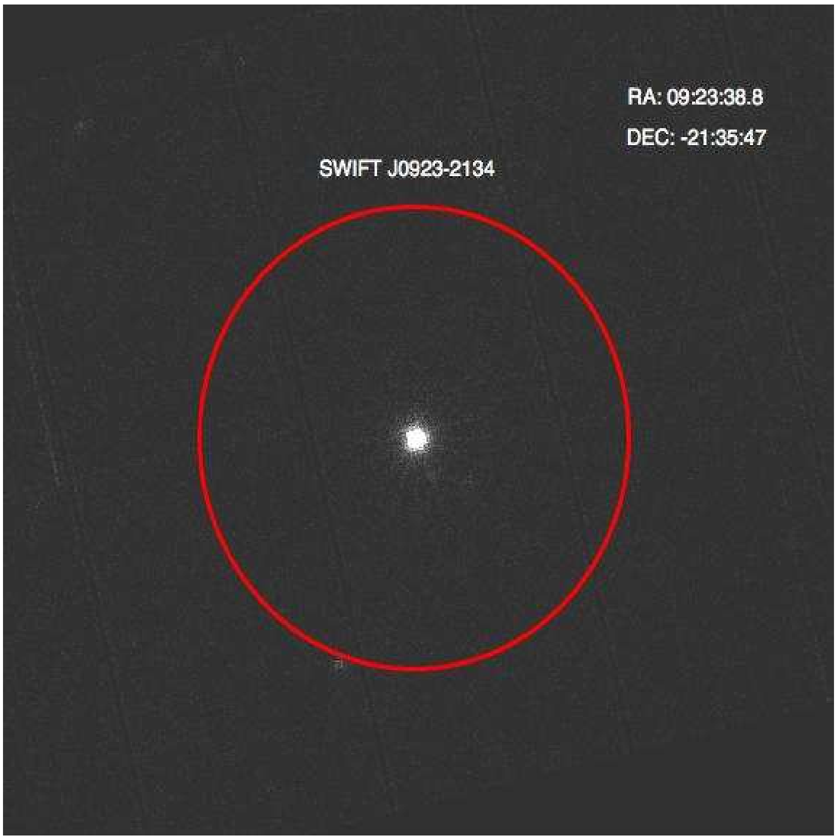

Figure 4.5: XMM image of a *SWIFT*/BAT source, SWIFT J0923-2134. It is obtained with XIMAGE in the energy range 0.3-10.0 keV. The red circle shows the BAT error box of radius 3.94’

Source counts were extracted from a circular regions centered on the source, choosing the

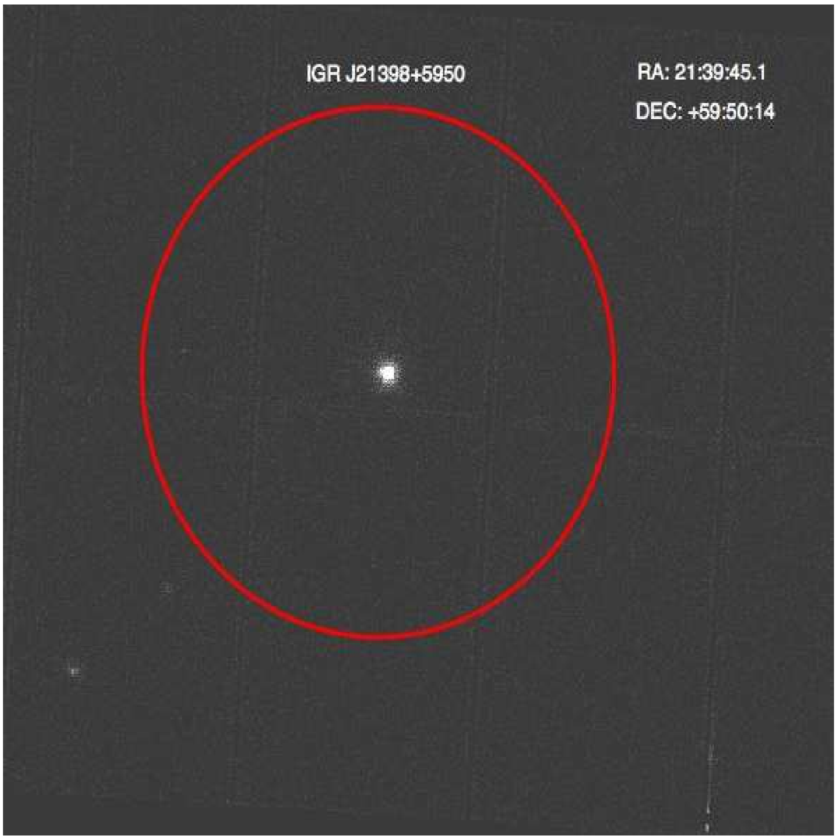

Figure 4.6: XMM image of an *INTEGRAL*/IBIS source, IGR J21398+5950. It is obtained with XIMAGE in the energy range 0.3-10.0 keV. The red circle shows the IBIS error box of radius 4.5’

radius in correspondence of the highest Signal-to-Noise ratio; background spectra were extracted from circular regions close to the source or from source-free regions of 80″ radius. The ancillary response matrices (ARFs) and the detector response matrices (RMFs) were generated using the *XMM* SAS tasks *arfgen* and *rmfgen* while the spectral channels were rebinned in order to achieve a minimum of 20 counts in each bin. Also in this case, the spectral analysis has been performed using XSPEC v.12.6.0 and assuming initially a simple power law passing only through Galactic absorption (Dickey & Lockman 1990); if this baseline model was not sufficient to fit the data, we then introduced extra spectral components as required, according to the F-test statistics. The results of this analysis are reported in Table 6.2 and 6.4, where we list the column density in excess to the Galactic value, the power law photon index, the reduced χ^2 of the best-fit model and the 2–10 keV flux; extra spectral parameters if required are reported in the notes at the end of the Tables. Also in the case of XMM data, quoted errors correspond to 90$\%$ confidence level for a single parameter of interest ($\Delta\chi^2 = 2.71$).

4.3 X-ray spectral results

As evident from the tables, in many cases the statistical quality of the data is poor allowing only a rough evaluation of the basic properties of the source under investigation; when this occurred we have favoured the estimate of the column density with respect to that of the photon index which has been fixed to 1.8. In other cases, the statistical quality of the data was good and in other even excellent allowing a more detailed insight into the X-ray properties of our sources. Examples of the quality of the data analyzed are reported in figures 4.7, 4.8, 4.9, 4.10, 4.11, 4.12 for a few sources (both from the *Swift*/BAT and *INTEGRAL*/IBIS high energy surveys and utilizing XRT and XMM observational data); in each figure the best fit model is reported.

Most objects in our sample are described by a simple absorbed power law, where the absorption is either only Galactic or a mixture of Galactic and intrinsic. The intrinsic absorption

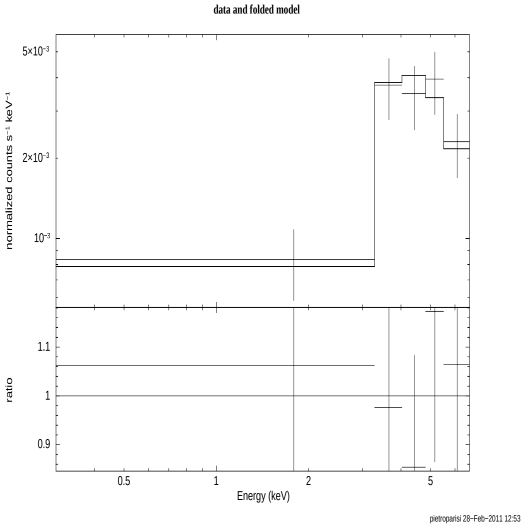

Figure 4.7: Example of a source with a very low statistical quality of XRT data. Top panel shows spectral analysis which refers to SWIFT J0038.5+2336, a *SWIFT*/BAT source. The best fit model found is a `wabs*wabs*pow`, a simple power law passing through both Galactic absorption and intrinsic absorption; the bottom panel shows the data to model ratio which provides an indication of the goodness of the fit.

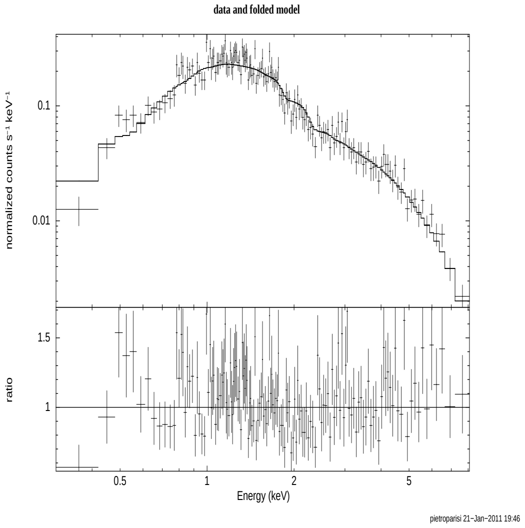

Figure 4.8: Example of a source with a good statistical quality of XRT data. Top panel shows the spectral analysis which refers to SWIFT J0530.0+2300 a *SWIFT*/BAT source. The best fit model found is a `wabs*wabs*pow`, a simple power law passing through both Galactic absorption and intrinsic absorption; the bottom panel shows the data to model ratio which provides an indication of the goodness of the fit.

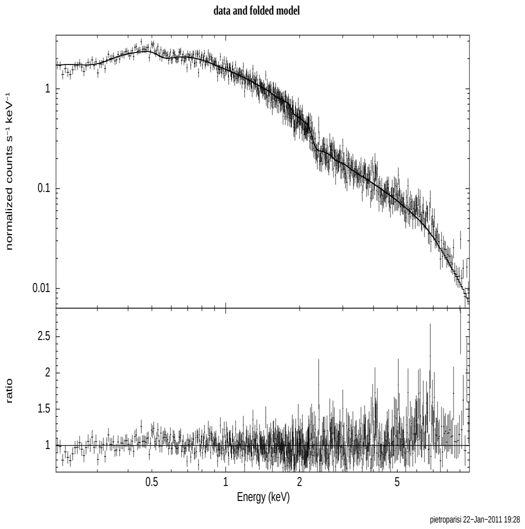

Figure 4.9: Example of a source with a very good statistical quality of XMM data. Top panel shows spectral analysis which refers to SWIFT J0923.7-2134 a *SWIFT*/BAT source. The best fit model found is a `wabs*pow`, a simple power law passing only through the Galactic absorption; the bottom panel shows the data to model ratio which provides an indication of the goodness of the fit.

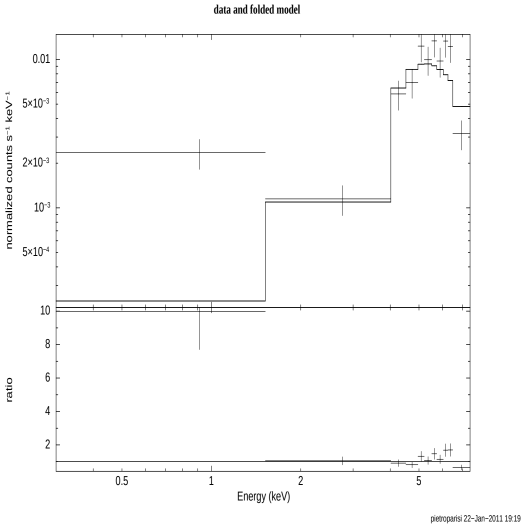

Figure 4.10: Example of a source with a very low statistical quality of XRT data. Top panel shows spectral analysis which refers to SWIFT J0255.2-0011 a *INTEGRAL*/IBIS source. The best fit model found is a `wabs*wabs*pow`, a simple power law with a photon index fixed to 1.8, passing through the Galactic absorption and the local absorption; the bottom panel shows the data to model ratio which provides an indication of the goodness of the fit.

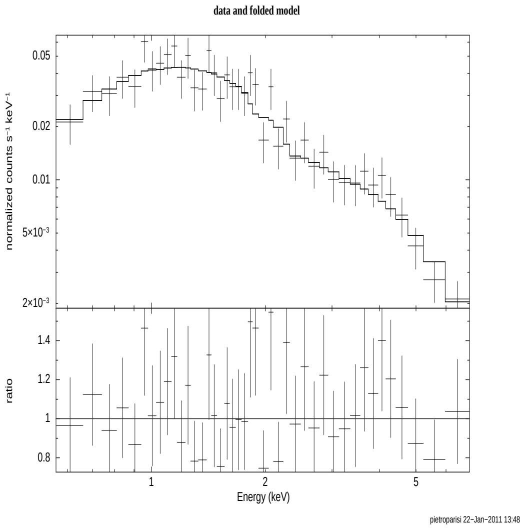

Figure 4.11: Example of a source with a good statistical quality of XRT data belonging to the *INTEGRAL*/IBIS catalogue. Top panel shows the best fit model found for this source, IGR J13168-7157, which is a `wabs*pow`, a simple power law passing only through the Galactic absorption; the bottom panel shows the data to model ratio which provides an indication of the goodness of the fit.

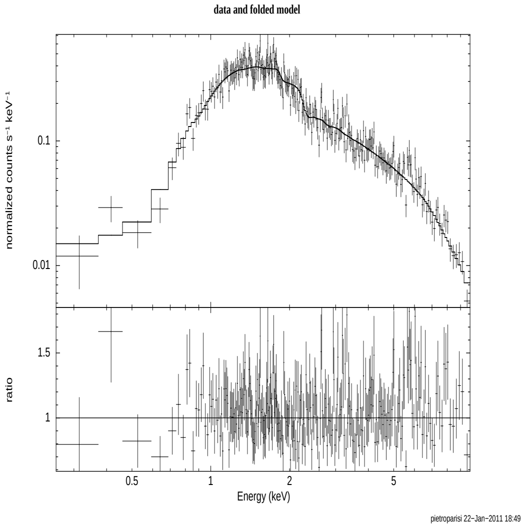

Figure 4.12: Example of a source with a very good statistical quality of XMM data belonging to the *INTEGRAL*/IBIS catalogue. Top panel shows the best fit model found for this source, IGR J21398+5950, which is a `wabs*wabs*pow`, a simple power law passing through both the Galactic absorption and the local absorption; the bottom panel shows the data to model ratio which provides an indication of the goodness of the fit.

is generally one and fully covering the source; alternatively it could be covering the source only partially like in the case of SWIFT J0845.0-3531, SWIFT J0902.+6007, SWIFT J0942.1+2342, SWIFT J1254.8-2655, SWIFT J1416.8-1158, SWIFT J2344.8-4245 and SWIFT J1513.8-8125. In other cases the absorption is even more complex as two absorptions are required of which one covers the source partially while the other could be full (like in SWIFT J0238.3-6161) or partial as well (like in SWIFT J0250.3+4645, SWIFT J0739.6-3144 and IGR J16351-5806). It is interesting to note that the objects which are characterized by peculiar or complex absorption belong to any type of AGN class from type 1 to type 2, but more than one absorber is only found in type 2 sources.

A few objects show a soft X-ray excess component which has been parameterized in a number of ways either with a bremsstrahlung, a black body or a power law component; in some case this second power law has been linked to the primary absorbed continuum by setting the two photon index to the same value. While the first three components are equally found in type 1 and type 2 AGN, the fourth, i.e. the power law with the photon index linked to that of the primary power law, is only found in type 2 Seyferts.

Finally in only 3 sources (SWIFT J1246.9+5433, SWIFT J2341.8+3034 and IGR J16351-5806) we observed emission lines in the 6-7 keV band: in all 3 objects a neutral Kα iron line is observed around 6.4 keV with equivalent width ranging from $\leq$ 0.6 keV to more than 1 keV. These sources are Seyfert 2 with a high column density, in fact IGR J16351-5806 is a Compton thick AGN (Malizia et al. 2009). In these objects it is not unusual to observe iron lines with a high EW due to the fact that while the continuum flux is reduced due to the high intrinsic absorption, the line flux is not absorbed, thus producing a high EW value. In SWIFT J1246.9+5433 we also observe a second line at 6.9 keV most likely associated with Kα resonant line from highly ionized iron; also the equivalent width of this line is high ($\sim$0.5 keV). In the following we will analyze the broad band X-ray spectral properties of our entire sample.

4.3.1 Photon index and column density distributions of the entire sample

Despite the low statistical quality of the data which is evident in some cases, it is still possible to obtain information on the spectral shape of the objects analyzed. In particular, we concentrate here on the photon index distribution and on the absorption properties of the sources in the sample.

The distribution of photon indices for our AGN is shown in figure 4.13; sources where Γ (photon index) was not constrained by the data were not considered. It is well known that the distribution of X-ray spectral slopes of AGN peaks around 1.9 and has a non-negligible dispersion (0.2-0.3, see for example Mateos et al. 2005 and references therein). We obtain a mean Γ value of 1.83 with a standard deviation of 0.34, i.e. most of our objects have spectra close to the canonical AGN value. Flat (Γ <1.5) spectra are far less common, especially in view of the large uncertainties associated with some of the X-ray data; nevertheless they exist in some objects, such as in SWIFT J2327.4+0939 and IGR J12107+3822 (the sources with the flattest spectrum observed in our sample) for which reasonably good quality data are available.

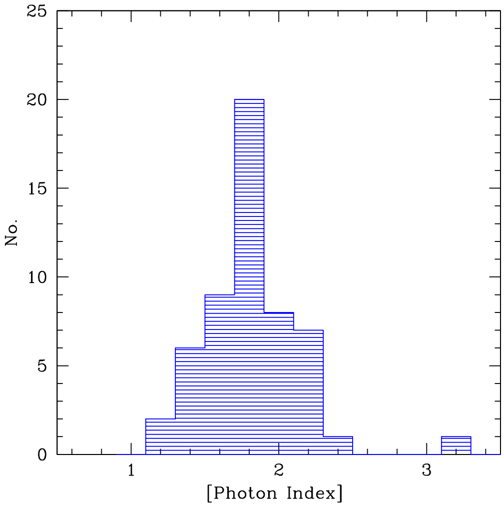

Figure 4.13: Distribution of the photon index of AGN belonging to our sample peaking at 1.83±0.34.

The column density distribution of our sources are shown in figure 4.14 for type 1 AGN, in

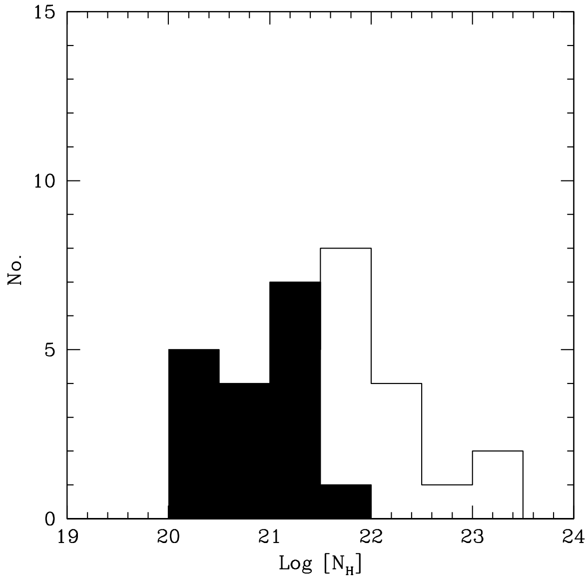

Figure 4.14: Column density distribution for type 1 objects belonging to our sample. The black filled bins represent the sources for which only upper limits of N_H are available.

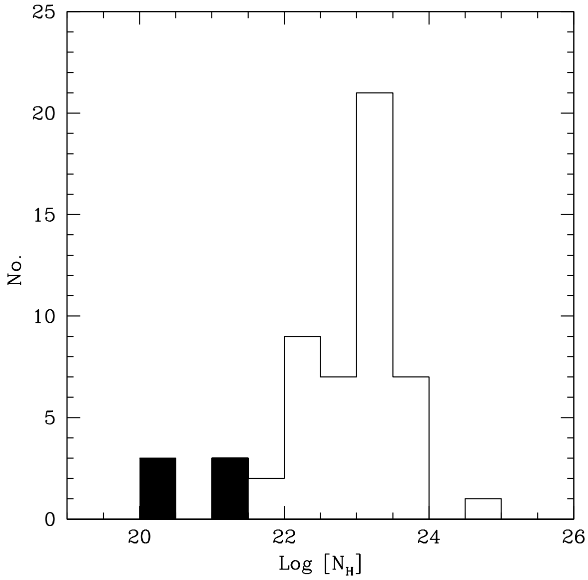

Figure 4.15: Column density distribution in type 2 objects belonging to our sample. The black filled bins represent the sources for which only upper limits of N_H are available.

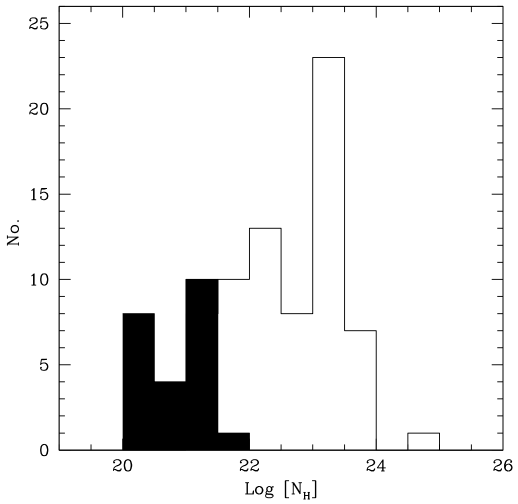

Figure 4.16: Column density distribution for the entire sample of AGN. The black filled bins represent the sources for which upper limits of N$_H$ are available.

figure 4.15 for type 2 AGN and in figure 4.16 for the entire sample of AGN. As we can see from table 6.2 and 6.4, various sources in the sample do not show intrinsic absorption and therefore their Galactic column density has been taken as an upper limit to the value of N$_H$; these sources are reported in the histograms as filled black bins. Furthermore, for those sources showing partial absorption, the measured column density as reported in the Tables has been adopted; in cases where more than one absorber has been found, the higher N$_H$ (partially or totally covering the source) has been plotted.

Absorption in excess of the Galactic value has been measured in 70 objects (around 74% of the sample) and of these more than half (52 objects) have a column density in excess of 10^{22} cm^{-2} (typically taken as the dividing line between absorbed and unabsorbed objects[1].

Absorption in excess of 10^{22} cm^{-2} was found in 22% of type 1 AGN and in 80% of type 2 AGN. Neither of the two NLS1 shows absorption, while all 3 pure LINERs are absorbed as is the source, SWIFT J1321.1+0858, which is in the transition region between Seyfert 2 and LINERs.

---

[1] This N$_H$ value represents the amount of absorbing neutral gas needed to hide the broad emission-line region (BLR), assuming a Milky Way gas-to-dust ratio.

Interestingly the only type 2 QSO in the sample is also heavily absorbed as is the XBONG listed between the INTEGRAL sample. Neither of the two SWIFT objects classified as Seyfert 1.5/1.8 has absorption in excess of 10^{22} cm^{-2} suggesting that their class is closer to that of type 1 rather than 2. This also confirms that our original assignment to the type 1 sample is correct. Clearly, the column density distribution of type 1 and type 2 AGN is significantly different: while type 1 objects cluster in the 10^{21}–10^{22} cm^{-2} range, type 2 sources have a much wider distribution peaking around an N_H value greater than 10^{23} cm^{-2}. In particular, we note that contrary to expectations, a number of type 2 AGN are unabsorbed (8 objects); we also point out that only one source, IGR J16351-5806, is found to be Compton thick (see also Malizia et al. 2009 for a more detailed discussion of this source). Typically in *SWIFT* and *INTEGRAL* AGN surveys the fraction of Compton thick AGN is around 5-10$\%$ (Malizia et al. 2009, Burlon et al. 2011) so that it could be unexpected to find only one source where we would have expected to observe between 5 and 9 of such objects. However, our sample is not complete in any way and it is assembled on the basis of our optical follow up work rather than following any specific selection criterion so that it is posible to have seen only one Compton thick AGN. Alternatively, we did not recognize a few of the type 2 AGN as Compton thick objects and thus we need to find a way to highlight them as discussed in the next section.

4.4 Discussion

The basic hypothesis of the unified theory of AGN is that the X-ray absorption and optical obscuration are heavily related: absorbed AGN should be classified as type 2 in optical (very narrow permitted and forbidden lines, so that in the optical spectra we see only the Narrow Line Region), while unabsorbed ones are expected to be of type 1 (broad permitted lines and narrow forbidden lines are visible, as we see both the Broad and the Narrow Line Regions). This relationship is not always respected as it is evident in our sample where we find absorption in a number of type 1 objects (SWIFT J0226.7-2819, SWIFT J0814.4+0821, SWIFT J0845.0-3531, SWIFT J0904.3+5538, IGR J09253+6929, SWIFT J0942.1+2342, IGR J10147-6354 and IGR J12107+3822). While SWIFT J0845.0-3531 and IGR J10147-6354 are located on the Galactic plane (below 10 degrees in galactic latitude) so that the excess absorption may be due to extra material along the Galactic line of sight, all others are at high galactic latitudes and so are likely to be intrinsically absorbed. These galaxies are all of intermediate type (1.2/1.5); within the standard model of Seyfert nuclei, their absorption can be understood by assuming that they are viewed at somewhat larger inclination angles than a typical type 1 AGN so that our line of sight intercepts thicker material from the torus. Alternatively they can be explained within newly proposed models for the AGN torus (clumpy torus), which will be explored in the next chapter. Further X-ray observations of these objects are clearly desirable because of the constraints that can be derived on the geometrical properties of the absorbing region.

On the other hand, we find in our sample a number of type 2 sources with no absorption as evident in figure 4.15. Even not taking into consideration those objects with poor quality data as in these cases we do not have a proper characterization of the source column density, we still find 3 Seyfert 2 AGN, namely SWIFT J0122.3+5004, SWIFT J0347.0-3025 and SWIFT J2333.9-2343 with an unexpectedly low N_H; this is clearly contrary to the expectation of AGN unified theory. Several authors have reported similar examples of AGN with no broad emission lines and low N_H (Panessa & Bassani 2002, Corral et al 2005). There are various explanations for this discrepancy including the low statistical quality of the X-ray spectra and the non simultaneity of the optical and X-ray observations.

Alternatively, it is possible that these Seyfert 2 are either Compton thick type 2 AGN or ”true” Seyfert 2, i.e. objects where the Broad Line Region is not hidden but likely not present. If the source is Compton thick, the 2–10 keV emission is completely blocked and could be seen as reflected/scattered radiation with no apparent absorption. On the other hand the hard X-ray photons detected above 10 keV are unaffected by absorption as long as $\log N_H$ is below

24.5; for higher column densities, even emission above 20 keV is blocked and can only be seen indirectly. It is possible that in our sample we have not recognized some Compton thick AGN because of the low statistical quality of the X-ray observations used to estimate N_H. To see if this has happened, we can use the diagnostic diagram provided by Malizia et al. (2007). This diagram uses the N_H versus softness ratio $F_{(2-10keV)}/F_{(20-100keV)}$ to look for Compton thick AGN candidates and its validity has recently been confirmed by Ueda et al. (2007) and Malizia et al. (2009): misclassified Compton thick objects populate the part of the diagram with low absorption and low softness ratios. Figure 4.17 shows this diagnostic tool applied to our sample; the $F_{(2-10keV)}/F_{(20-100keV)}$ ratio for all our sources are listed in Table 6.2 and 6.4 along with their basic spectral parameters. The 20-100 keV data have been observed from the IBIS and BAT surveys (Bird et al. 2010 and Cusumano et al. 2010). Note that in the case of BAT data we estimated the 20-100 keV flux from the published 14-195 keV value, assuming a power law of photon index Γ = 2.02 (the reader should refer to the next chapter for 20-100 keV flux values). In the plot of figure 4.17, an indication of decreasing softness ratio as the absorption increases is visible as expected if the 2-10 keV flux is progressively depressed as the absorption becomes stronger. Blue symbols in the figure represent upper limits on the column density both for type 1 and type 2 objects, indicated with red squares and triangles respectively. As anticipated, most of our sources follow the expected trend except for a few objects which have a too low softness ratio for the observed column density, suggesting a Compton thick nature. Indeed, most of these sources are type 2 AGN and can therefore be taken as possible Compton thick candidates. The only exception is the NLSy1 IGR J16426+6536; in this case the anomalous position in the diagram can be explained with strong X-ray variability which is a common characteristic of this type of AGN (see also Panessa et al. 2011); note that IGR J16426+6536 is marked as variable in the survey of Bird et al. (2010).

We therefore suggest that IGR J03344+1506, SWIFT J0122.3+5004, SWIFT J0107.8-1137 and to a lesser extent IGR J01545+6437 are new Compton thick AGN candidates for which

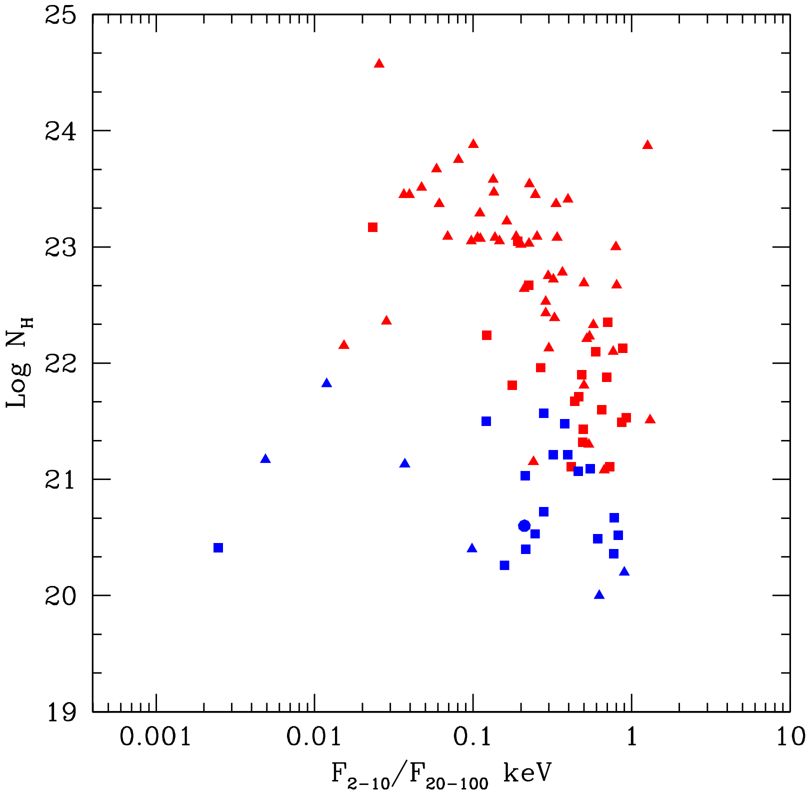

Figure 4.17: Column density plotted against the F2-10 keV/F20-100 keV flux ratio of our sample of AGN. Squares are type 1 objects, triangles are type 2 AGN and the circle is the unclassified source (SWIFT J2327.4+0939). The blue symbols represent those objects for which we only have upper limits of N_H, where no intrinsic absorption has been measured.

further analysis is necessary (i.e. those Seyfert 2 with F$_{(2-10keV)}$/F$_{(20-100keV)}$ below a value of 0.05).

Other indirect arguments can help in discriminating between the Compton thick and Compton thin nature of type 2 AGN, such as the equivalent width of the iron line and the ratio of isotropic versus anisotropic luminosities typically F$_X$/F$_{[OIII]}$[2] (Bassani et al. 1999 and Panessa and Bassani 2002). Unfortunately in all cases mentioned above the X-ray data comes from Swift/XRT observations which do not allow to probe the iron line (XRT has no enough sensibility to detect this feature). We therefore have to rely on the F$_X$/F$_{[OIII]}$ ratio, that can be estimated by combining X-ray and optical information gathered in this work. The $[OIII]$ flux is generally considered a good isotropic indicator of the luminosity because it is produced in the Narrow Line Region, which is not strongly affected by absorption (Bassani et al. 1999, but see next chapter). The F$_X$/F$_{[OIII]}$ ratio has been studied in a large sample of Seyfert 2 galaxies; all Compton thin AGN (type 1 and 2) show ratios higher than 1, while Compton thick sources show ratios below this value (Bassani et al. 1999). Using the $[OIII]$ flux corrected for the host galaxy reddening, we find F$_X$/F$_{[OIII]}$ values of 0.022, 0.13 and 0.06 for IGR J03344+1506, IGR J01545+6437 and SWIFT J0122.3+5004 respectively. Unfortunately in the case of SWIFT J0107.8-1137 we do not have sufficient information to estimate the Balmer decrement and hence to correct the $[OIII]$ flux. The uncorrected $[OIII]$ flux provides loose upper limits which do not clarify the issue. It is evident that in this case, more sensitive X-ray observations, particularly around the iron line could help in confirming Compton thick nature of this object. The identification of at least 3 Compton thick candidates would take to $\geq 4\%$ the fraction of these sources in the sample, a percentage more in line with values reported by other authors.

Two more unabsorbed Seyfert 2, SWIFT J2333.9-2343 and SWIFT J0347.0-3025 are found but they are unlikely to be Compton thick objects as their location is well within the expected region of N$_H$ versus F$_{(2-10)keV}$/F$_{(20-100)keV}$. Indeed, for SWIFT J0347.0-3025 we find a F$_X$/F$_{[OIII]}$

---

[2] The F$_{[OIII]}$ is corrected for reddening in the host galaxy by means of the H$_\alpha$/H$_\beta$ Balmer decrement, see next chapter.

value of 4, compatible with a Compton thin nature while for SWIFT J2333.9-2343 no Hα line is detected to allow the correction of the $[OIII]$ flux. While SWIFT J0347.0-3025 is classified as a composite between Seyfert 2 and starburst so that its optical classification is uncertain and possibly compatible with the observed column density, SWIFT J2333.9-2343 shows a true Seyfert 2 spectrum and so qualifies as a ”true” Seyfert 2 nucleus; indeed the upper limits on the column density cannot explain the occultation of its Broad Line Region. Rather, this region is likely missing in these objects; this type of AGN will be discussed in more detail in the next chapter.

Finally we confirm that a number of type 1 AGN are absorbed with column density in excess of 10^{22} cm^{-2}, but only two (SWIFT J0814.4+0821 and IGR J09253+6929) have unusually high N$_H$ values; both are Seyferts of type 1.5 like NGC4151 and MKN 6 which also are characterized by large intrinsic absorption (see Malizia et al. 2008).

4.5 Conclusions

SWIFT/XRT and *XMM-Newton* follow-up X-ray observations of 94 *SWIFT*/BAT and *INTEGRAL*/IBIS AGN have not only pinpointed their X-ray counterparts allowing the unambiguous optical identification of the hard X-ray source and the determination of their AGN class as found in the previous chapter, but most importantly have allowed the determination of their X-ray spectral properties in many cases reported here for the first time. In particular, for most objects in the sample, photon index, absorption column and X-ray flux have been measured.

We find a mean photon index of 1.83 with a dispersion of 0.34. 74$\%$ of the objects have column densities in excess of 10^{22} cm^{-2} and, as expected, a large fraction of the absorbed sources are within the type 2 AGN sample. We have also used a new diagnostic tool (N$_H$ versus F$_{(2-10)keV}$/F$_{(20-100)keV}$ softness ratio) with which we isolate or find a few peculiar objects: a) two heavily absorbed Seyfert 1 galaxies ; b) 4 Compton thick AGN candidates of which at least 3 are strong cases; and c) at least 1, but possibly 2, examples of ”true” type 2 AGN, i.e. those where the Broad Line Region is not hidden but likely not present.

Chapter 5

Hard X-ray and Optical Properties of Active Galactic Nuclei

5.1 Introduction

There are striking differences in the optical spectra of AGNs. Some show broad (FWHM $>$ 2000 km s^{-1}) permitted and narrow (FWHM$\sim$ 400 km s^{-1}) forbidden emission lines, others exhibit only narrow forbidden emission lines and some only absorption lines. One generally assumes that there is less intrinsic diversity among AGNs than we observe, and that the variety of AGN phenomena is due to a combination of real differences in a small number of physical parameters (like for example the luminosity) coupled with apparent differences which are due to observer-dependent parameters (like the orientation). In the Antonucci et al. (1993) simple unified model for AGNs, it is the geometry of a dusty torus which determines the amount of obscuring material along the observers line of sight to the central X-ray emitting regions, as well as which region (broad-line or narrow-line) one is observing. In this model, broad-line AGN are unobscured sources in which one is seeing down the ionization cone to clouds in high density regions within 0.003 parsecs of the AGN accretion disk. Narrow line AGNs, on the other hand, are observed when the central source is obscured by the circumnuclear material and the emission lines come from lower density clouds at 30-100 parsecs from the accretion disk (see Figure 1.3).

X-ray data alone have long been used to estimate the amount of obscuration between the observer and the nuclear source through a measurement of the intrinsic column density. Then one expects, on the basis of the AGN unified theory, that unobscured objects are optically classified as AGN with broad and narrow emission lines while obscured sources are characterized by narrow emission lines only; objects showing only absorption lines in their optical spectra are normal galaxies which may contain an otherwise hidden AGN. Various studies and some of the findings reported in the previous chapter suggest that the X-ray and optical nuclear absorption do not always match in AGNs. Indeed we have found that a small percentage of our AGN have X-ray spectra that show no absorption but have optical spectra that suggest obscuration; similar cases have been also reported in the literature (see for example Maiolino and Risaliti 2007 for a list of references). The opposite effect, i.e. objects having X-ray spectra that show absorption but have optical spectra that suggest no obscuration, has also been found in our sample and also reported in previous work (again refer to Maiolino and Risaliti 2007 for a set of references). Thus a comparison between X-ray and optical properties of AGN can highlight ‘unconventional’ AGN and give us an insight into unified theory models as well as information on the central engine. Such type of studies have generally been done employing samples of AGN observed in the soft (below 20 keV) X-ray band. Only recently, with the advent of AGN samples detected at higher X-ray energies (above 20 keV), similar studies have been applied to hard X-ray selected objects which are believed to be less affected by the problems related to the absorption. Generally these studies were limited to small sample of objects. Here with our sample of AGN we have the possibility for the first time to study the hard X-ray and optical properties of a statistically significant sample of objects. In the following, we will analyze the hard X-ray emission of our AGN in comparison to their optical R magnitude and [O III] luminosity and further compare the optical versus X-ray absorption; our results will be discussed within the unified model of AGN.

Tables 5.4 and 5.4 provides all information used in this chapter, i.e. the 20-100 keV flux, the R magnitude, the [OIII] flux corrected both for the host galaxy reddening and the E(B-V) values.

5.2 Optical R magnitude versus X-ray flux

A way used in the literature to highlight ‘unconventional’ AGN is the ratio between X-ray 2-10 keV flux and optical magnitude R (defined as Log(F_x/F_{opt}) = Log F_x + 5.5 + R/2.5, see Maccacaro et al. 1988; Barger et al. 2002; McHardy et al. 2003); this is considered to be a fairly reliable indicator of the X-ray source classification. Indeed, the distribution of Log(F_x/F_{opt}) values of most of the spectroscopically identified X-ray selected AGN from ROSAT (Hasinger et al. 1998), ASCA (Akiyama et al. 2003), Chandra (Giacconi et al. 2001) and XMM-Newton (Mainieri et al. 2002; Fiore et al. 2003) surveys fall within $-1<$Log(F_x/F_{opt})<1. Thus a value of Log(F_x/F_{opt}) within these boundaries is a clear sign of AGN activity. However, not all AGN are within these boundaries as a sizable fraction of X-ray selected sources are located outside. Two groups of ‘unconventional’ AGN are often mentioned in the literature (Comastri et al. 2003): the first includes objects that are X-ray weak for their R magnitude and have therefore Log(F_x/F_{opt}) $\leq$-1; the second contains instead AGN that are optically faint and relatively X-ray bright and so have Log(F_x/F_{opt}) $\geq$+1. The first group of objects may contain a few emission line galaxies and some only apparently normal galaxies like the X-ray Bright Optically Normal Galaxies (XBONG) discussed previously. The second group includes objects that are at high redshifts (both absorbed and unabsorbed). It is also interesting to point out that this diagram was never tested with a hard selected sample of AGN such as ours. Herein therefore we use the data collected in the previous chapters to construct the optical R magnitude versus 2-10 keV X-ray flux diagram for our 94 objects (figure 5.1 and tables 6.2,6.4); the two dashed lines in the figure represents the region generally populated by X-ray selected AGN and correspond to Log(F_x/F_{opt}) $\leq$-1 bottom line and Log(F_x/F_{opt}) $\geq$+1 top line. The sources outside these limits can therefore be considered ‘unconventional’ (Comastri et al. 2003).

We find that about half of the sources in our sample have Log(F_x/F_{opt}) ratios typical of AGN and thus fall within the shaded area, while the remaining half are located outside the expected boundaries. Only few of these outliers have Log(F_x/F_{opt}) $\geq$+1 while the majority populate the area characterized by values of Log(F_x/F_{opt}) $\leq$-1. This is somehow an unexpected result since we know through our optical follow up work as well as from the X-ray data analysis and the hard X-ray detection that our objects are all AGN and in fact bright ones. The few objects at high values of the Log(F_x/F_{opt}) ratios, i.e. above +1 are 3 Seyfert 1.5 (IGR J00333+6122, IGR J21398+5950 and IGR J22292+6647), the only unclassified AGN in our sample (SWIFT J2327.4+0939) and the Seyfert 2 galaxy IGR J0216.3+5128: all but one, SWIFT J2327.4+0939, are at redshift $\geq$0.1 and so their location is not so peculiar, but rather is similar to those AGN at high redshift found in X-ray surveys. Of the many sources that have low values of the Log(F_x/F_{opt}) ratios, i.e. below -1 the majority are type 2 AGN including 3 of the 4 Compton thick candidates discussed in the previous chapter (see figure for names); the location of these 3 objects in the diagram reinforce their interpretation as heavily absorbed AGN. Viceversa the two unabsorbed Seyfert 2 which are probably not Compton thick but very likely naked type 2 objects fall within the dashed lines. As a concluding remark we note that in our sample type 1 and type 2 AGN have remarkably different[1]. Log(F_x/F_{opt}) ratios (see for comparison figure 5.2 and 5.3) with the distribution of the second group of AGN significantly shifted towards lower ratios: while type 1 sources have Log(F_x/F_{opt}) ranging from -2.5 to 1.5, type 2 objects go from -4 to 1.5. Using Comastri et al. (2003) nomenclature, we find that optically classified type 2 AGN are more ‘unconventional’ than type 1.

The presence of so many type 2 AGN in the lower part of the diagram shown in figure 5.1 could be interpreted as a mixture of the following two effects: reduction of the X-ray flux due to absorption intrinsic to the source and presence of a bright galaxy around the heavily obscured

---

[1] The results of a K-S comparison test suggest that these values are not drawn from a single population; P =0.0002

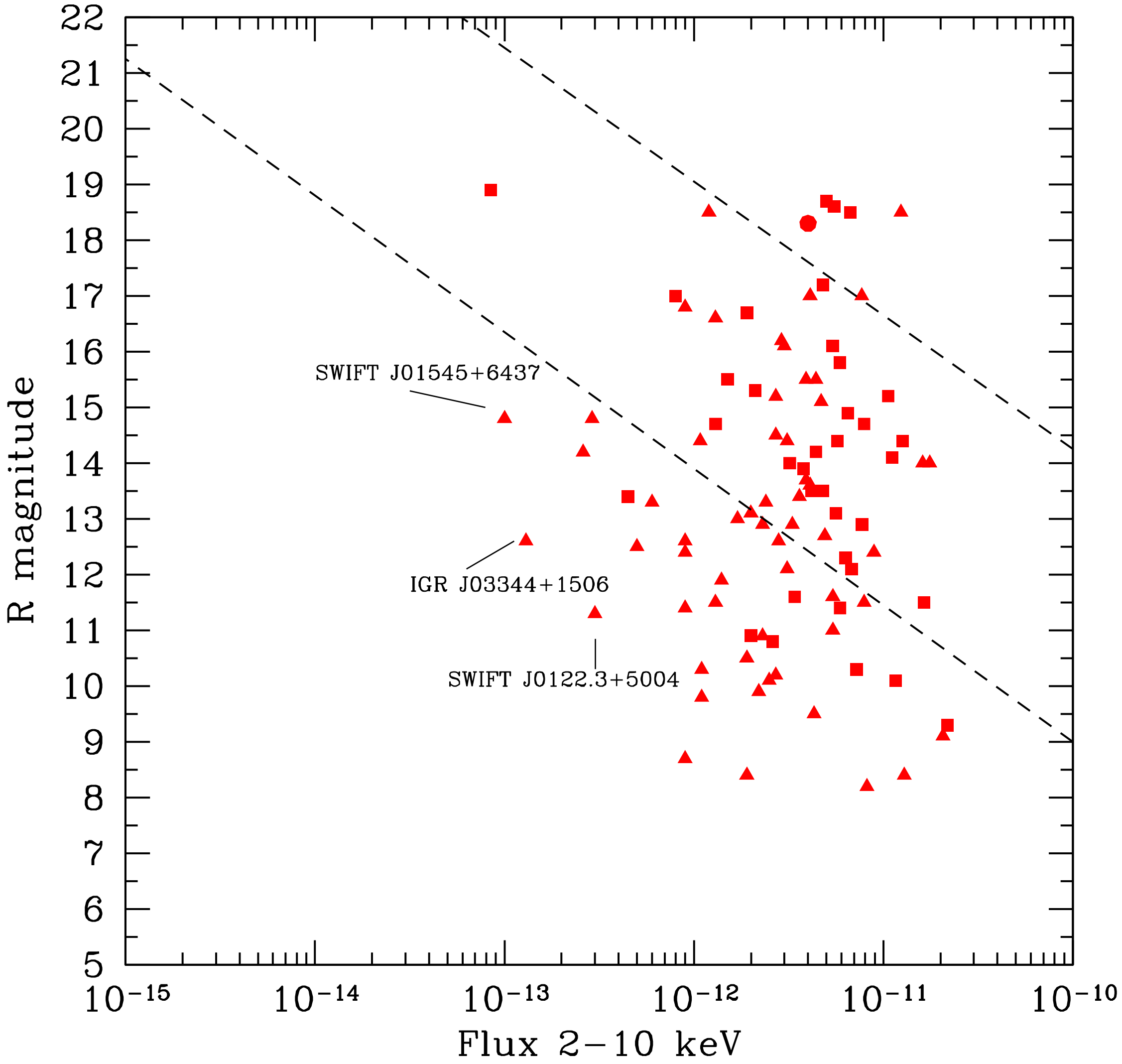

Figure 5.1: The 2-10 keV flux versus R band magnitude for our 94 hard X-ray sources. The squares indicate type 1 AGN, while the triangles refer to type 2 AGN. The only unclassified source in the sample is shown as a circle. Compton thick candidates are emphasized in the plot with their names.

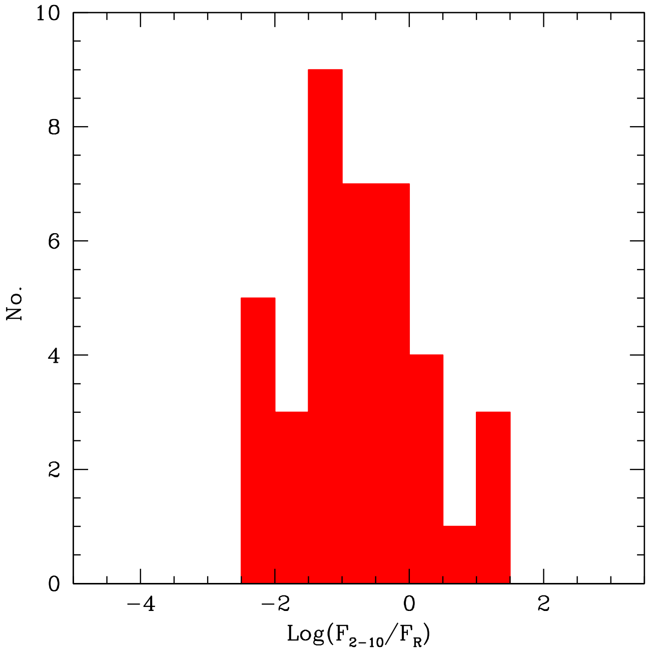

Figure 5.2: This histogram shows the 2-10 keV flux to R flux ratio for type 1 AGN.

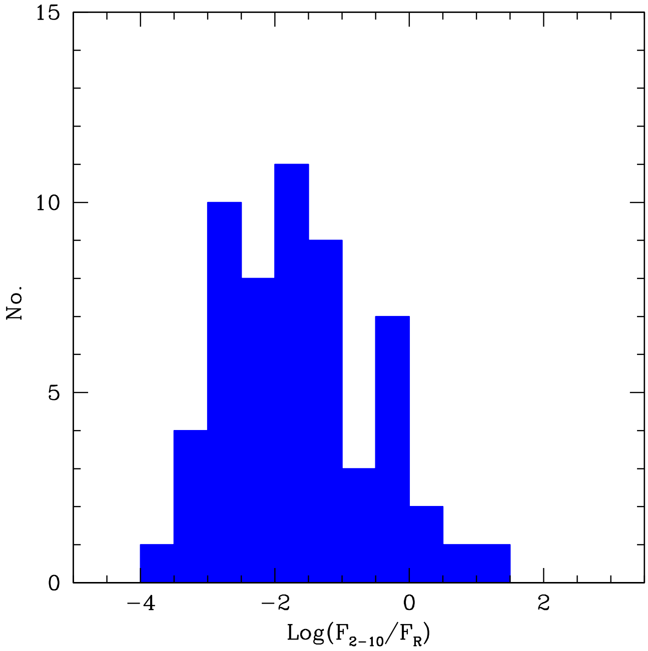

Figure 5.3: This histogram shows the 2-10 keV flux to R flux ratio for type 2 AGN.

AGN which contributes to the R flux. To check for the presence of the first effect we can use our 20-100 keV flux (see Fig. 5.5) instead of the more conventional 2-10 keV flux: the hard X-ray band is in fact by far less affected by absorption and so one would expect to see more overlap in the Log(F_x/F_{opt}) distributions of type 1 and type 2 AGN. This is shown in figure 5.5 where indeed what we observe is that the two distributions are more consistent with each other and only a small excess of type 2 sources fall towards lower values of the hard X-ray versus optical ratios. This small discrepancy can be explained as due to the fact that in the presence of very strong absorption (from a few 10^{23} to 10^{25} cm^{-2} in column density), even the hard X-ray flux is slightly reduced and need to be corrected for this effect. It is also likely that a very bright galaxy particularly visible in nearby objects contributes to the R flux thus reducing the F_x/F_{opt} flux ratio. These two combined effects provide an intrinsically higher 20-100 keV emission and a lower optical nuclear radiation and hence a higher Log(F_x/F_{opt}) ratio then observed. Overall we can conclude that we do not find strong evidences for many of the so called ’unconventional’ AGN and that our hard X-ray selected objects fit quite well within the optical versus X-ray boundaries expected for active galaxies. The few ‘unconventional’ AGN we observed are the unabsorbed Seyfert 2 and few absorbed type 1 AGN.

5.3 [OIII] emission versus hard X-ray continuum

Kauffmann et al. (2003) and Heckman et al. (2004) proposed the use of the luminosity of the [OIII]$_{\lambda 5007}$ (hereafter, [OIII]) line as a tracer of AGN power and hence of its bolometric luminosity. There are many advantages in using the [OIII] line: (1) in AGN it is typically strong and easy to detect; and (2) although it can be excited by both massive stars and AGNs, it has been observed to be relatively weaker in metal-rich, star forming galaxies than in active galaxies. However, the disadvantage is that one needs to assume that [OIII] is an unbiased, orientation independent indicator of the ionizing flux from the AGN. Narrow emission lines are thought to

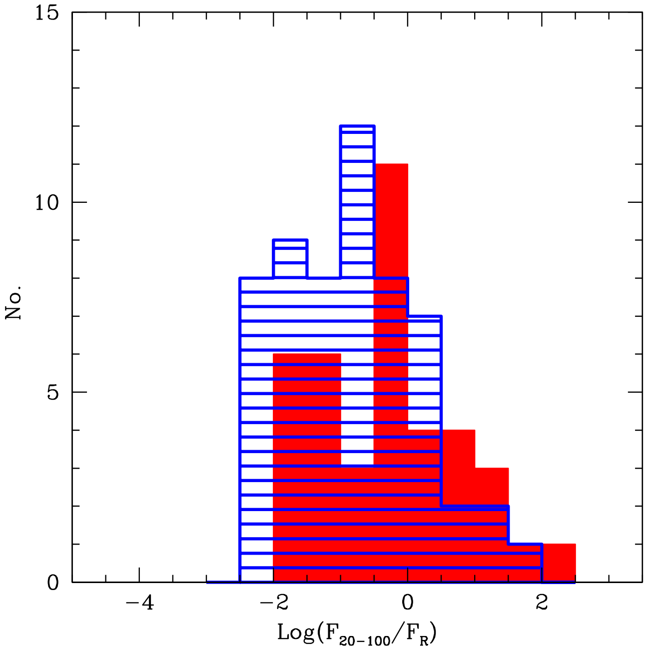

Figure 5.4: This histogram shows the 20-100 keV flux on R flux ratio for type 1 (red histogram) and type 2 (blue histogram) AGN. As it can seen from the figure the two distributions have more similar ranges than obtained using the 2-10 keV flux.

arise in gas excited by ionizing radiation escaping along the polar axis of the obscuring torus. Since the narrow line region lies outside of the dusty circumnuclear material, these lines should not suffer from obscuration by the high column density material (though they may be affected by dust within the host galaxy). AGN activity can also be traced through the 2 - 10 keV luminosity, although this measurement may suffer from absorption. The comparison between these two emissions has often been studied in the literature: although there is some evidence of a correlation between the [OIII] and the X-ray luminosities (e.g., Mulchaey et al. 1994) and, indeed, many researchers have assumed it to be so in their analyses (Netzer et al. 2006; Bongiorno et al. 2010), recent work has called this conclusion into question (e.g., Cocchia et al. 2007; Melendez et al. 2008; Diamond-Stanic et al. 2009) and the issue is still unsettled; clearly this provide evidence that the unified theory of AGN is not working well. Since hard X-rays are able to cut through much of the dust and gas that are around an AGN, they represent a more reliable indicator of the source bolometric luminosities; the 20-100 keV flux is indeed a better way to test the correlation between [OIII] and X-ray luminosities than the 2-10 keV flux. As a matter of facts, Heckman et al. (2005) found a relation between the hard X-ray (3-20 keV) and the observed [OIII] luminosities for a sample of AGN in the RXTE slew survey. But their result has been questioned recently by Melendez et al. (2008) and Winter et al. (2010) using a sample of *Swift*/BAT AGN: indeed both teams found that the [OIII] emission was not correlated with the hard X-ray (14-195 keV) radiation. With our sample of almost 100 objects we are in the position of adding some information to this dispute, by comparing once again the [OIII] luminosities and the 20-100 keV luminosities of our sample.

Following Bassani et al. (1999), we correct large-scale obscuration in the AGN host galaxy using the following equation:

$$F_{[OIII],corr} = F_{[OIII]obs} \times \left[\frac{(H_\alpha/H_\beta)}{(H_\alpha/H_\beta)_0}\right]^{2.94}$$

For the application of this method we can rely on the H_α/H_β ratio for most but not all of our sources, obtained for our optical follow-up work. In some objects the Balmer lines are blended with other lines and need to be deblended before calculating the Balmer decrement. We have done this interactively by carefully choosing each line end points and then by fitting their profile with a gaussian.

For example, in type 1 objects, where the H_α is strongly blended with the forbidden narrow [NII] lines, it is not easy to obtain a reliable H_α/H_β estimate. In these cases, we have also used the H_γ/H_β ratio, taking into account that H_γ is also blended with the [O III]$_{\lambda 4363}$; by comparing the two ratios it is possible to give a more reliable estimate of the extinction. For the intrinsic Balmer decrement we have assumed a value of 2.76 for $H(_\alpha/H_\beta)_0$ and 0.474 for $H(_\gamma/H_\beta)_0$. Besides being necessary for the correction of the [OIII] flux, the Balmer decrement can be used to estimate E(B-V), using the extinction curve of Osterbrock (1989);

$$E(B-V) = a\ Log \left(\frac{H_\alpha/H_\beta}{(H_\alpha/H_\beta)_0} \right),$$

where H_R is the observed Balmer decrement, $H_{R,intr}$ is the intrinsic one, while *a* is a constant which is respectively 2.21 and -5.17 in the case of the H_α/H_β and the H_γ/H_β Balmer decrement. In cases of mismatch between the H_α/H_β and H_γ/H_β values, likely due to the strongly blended nature of the H_α line, we extrapolate the H_α/H_β ratio from the value of the second Balmer decrement, using this value for the redding correction. It is clear that in doing so we introduce large uncertainties which the reader should keep in mind in the following considerations.

The average H_α/H_β for our entire sample is 4.5±3.2 (corresponding to E(B-V) = 0.478 mag), which is very similar to the median H_α/H_β ratio of 5.2±3.1 estimated by Trouille and Barger (2010) in their sample of AGN. If we calculate the mean Balmer decrement for type 2 AGN, we obtain 6.1±3.4; this compares well with the value of 6.5 obtained for the sample of Seyfert 2 reported by Bassani et al. (2009) as well as with the value of 4 reported by Zakamska et al.

(2003) for their SDSS type 2 AGN sample. For type 1 AGN we instead obtain (as expected) a mean Balmer decrement of 2.8±1.8, i.e. similar to the intrinsic H_α/H_β value assumed above. We conclude that, despite all the uncertainties introduced in the calculation, our estimates are reliable and in line with previous studies. We therefore decided to use our calculated mean values (2.8 and 6.1 for type 1 and 2 AGN respectively) in those cases where no information was available from the Balmer decrement.

In figure 5.5 we plot the corrected [OIII] luminosity against the 20-100 keV luminosity for our sample of AGN, to test if there is a correlation between the hard X-ray and [OIII] luminosities. We do not found a significant correlation between these two quantities, also if we use the entire sample of AGN. Using the least-squares (OLS) bisector method (Isobe et al. 1986), we obtained the following relations:

$$Log\, L_{20-100keV} = (0.89 \pm 0.07) \times Log\, L_{[OIII],corr} + (6.41 \pm 3.10)$$

with a correlation coefficient of R^2 of 0.2 for the entire sample;

$$Log\, L_{20-100keV} = (1.02 \pm 0.10) \times Log\, L_{[OIII],corr} + (1.28 \pm 4.11)$$

with a correlation coefficient of R^2 of 0.2 for type 1 objects and

$$Log\, L_{20-100keV} = (0.78 \pm 0.09) \times Log\, L_{[OIII],corr} + (10.96 \pm 3.87)$$

with a correlation coefficient, R^2, of 0.3 for type 2 sources.

Thus the correlation is not evident in all cases and we found a significant scatter in the data. These results are in agreement with those of Meléndez et al. (2008) and Winter et al. (2010). The large scatter observed is more marked for type 2 than for type 1 sources.

This is illustrated in figure 5.6 and 5.7 where we plot the distribution of the [OIII]/$L_{20-100\ keV}$

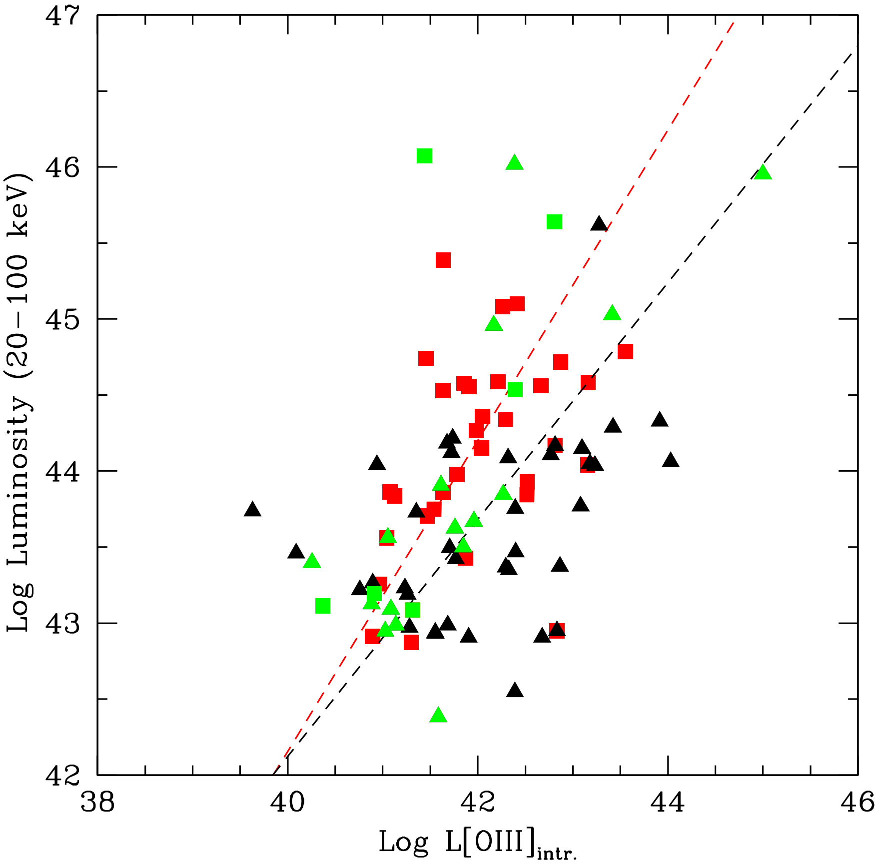

Figure 5.5: Relationship between reddening corrected [OIII] luminosities and 20-100 keV luminosities. In the plot, red squares show type 1 AGN, while black triangles type 2 AGN. The green ones indicate sources with an [OIII] luminosity corrected with the mean value of the Balmer decrement. The red and the black dashed lines indicate respectively the very week correlation seen for the type 1 AGN and type 2 AGN.

ratios for type 1 and 2 sources separately. The scatter observed is probably due to various factors. Because we are dealing with hard X-ray luminosities we expect the effect of absorption to be small but not absent.

Indeed we have seen in the previous section that we have in our sample one Compton thick AGN and few candidate ones: in these sources the correction on the hard X-ray luminosity could be important while in less absorbed objects is less significant but is still present. This could explain the scatter we see in the hard X-ray luminosities as well as the slightly different peak in the distribution of type 1 and 2 objects (figure 5.8): for broad line objects the mean value of Log $L_{20-100\,keV}$ is 44.16±0.76, while for narrow line objects is 43.71±0.76. Note however that the range of observed values is comparable for both types. As for the 20-100 keV luminosities we observed also for $L_{[OIII]}$ a slightly different peak value but similar range of values for type 1 and 2 AGN (figure 5.9): the mean logarithmic [OIII] luminosity is 41.94±0.73 and 42.03±1.03 for Broad Line and Narrow line AGN respectively.

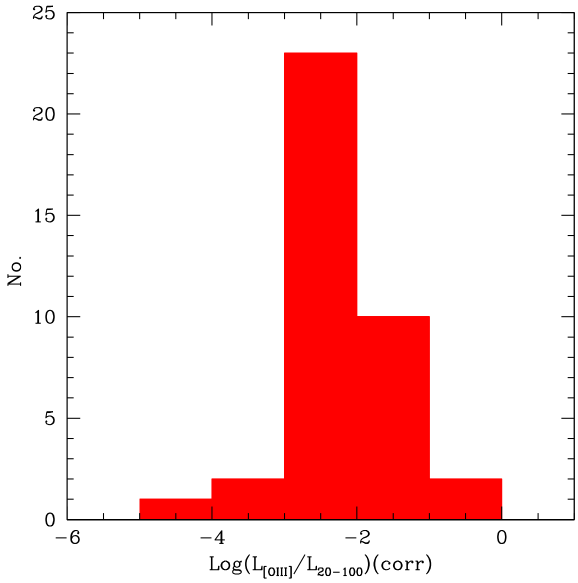

Figure 5.6: Histogram of the log of the ratio of the hard X-ray (20-100) keV to $[OIII]_{\lambda5007}$ luminosities for type 1 AGN. This distribution has a mean of -2.21 dex with a standard deviation of 0.79 dex.

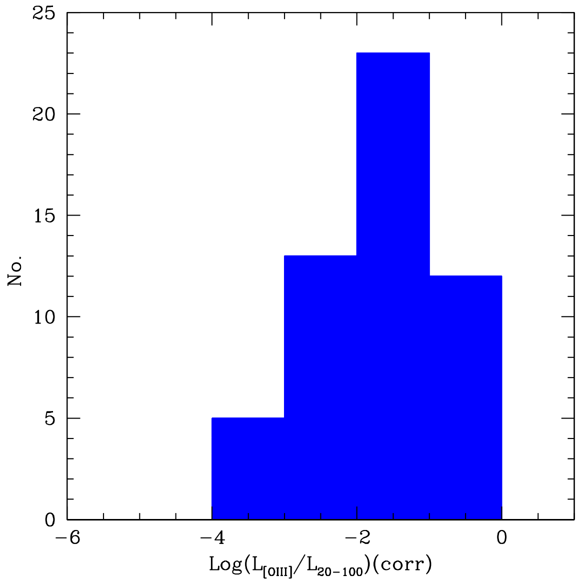

Figure 5.7: Histogram of the log of the ratio of the hard X-ray (20-100) keV to [OIII]$_{\lambda 5007}$ luminosities for type 2 AGN. This distribution has a mean of -1.68 dex with a standard deviation of 0.76 dex.

In this case one possible explanation is that the extinction corrections have large uncertainties due to the quality of the optical data available, the way we estimate the H_α/H_β (and in our case also the H_γ/H_β) ratios and the used of average values for the Balmer decrement in many sources.

Furthermore one must take into account the fact that the hard X-ray and [OIII] luminosities are not simultaneously taken, while AGN are known to be variable both at optical and X-ray wavebands; this could introduce further scattering in the [OIII] and hard X-ray luminosity diagram. Our conclusions are therefore similar to those of Winter et al. (2010) and Melendez et al. (2008), but contrary to these authors we are cautious in suggesting that the unified model of AGN is at risk: there are still too many uncertainties introduced in the reddening correction applied to the [OIII] luminosity to exclude the presence of a correlation. What can be said at the present stage is that the [OIII] luminosity can only be used to predict the hard X-ray luminosity with a large uncertainty. Better quality data, especially in providing the Balmer decrement, are necessary to settle this issue.

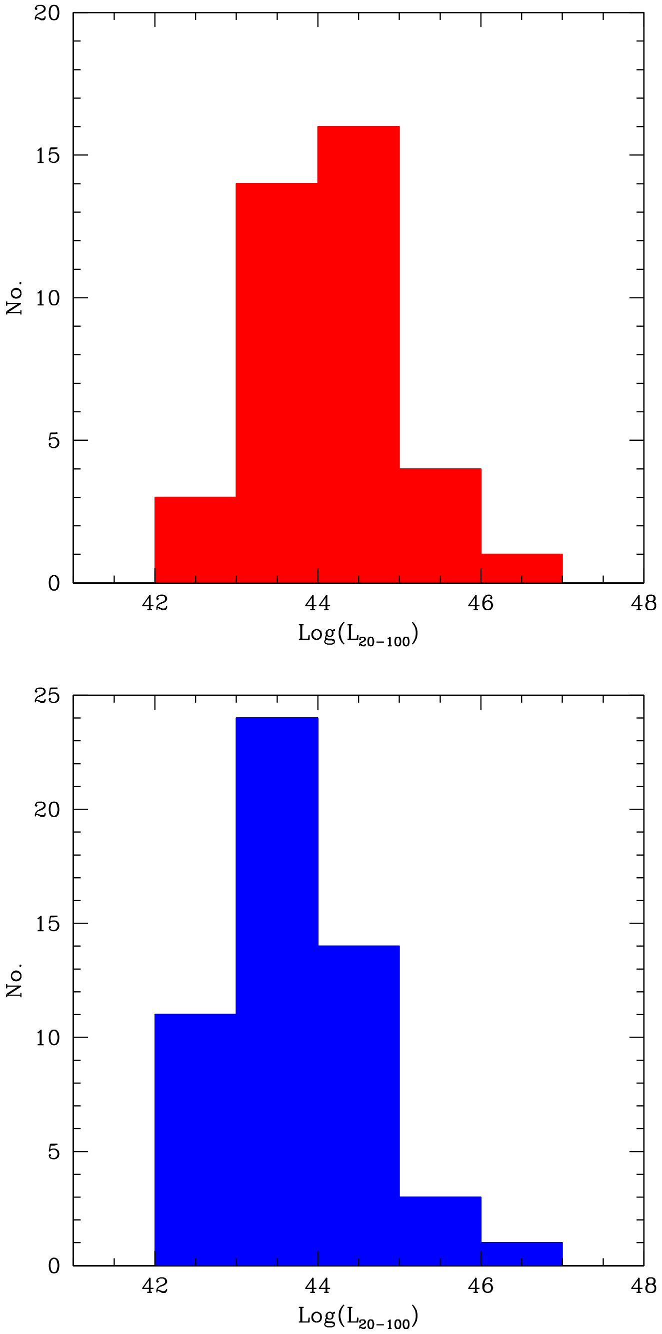

Figure 5.8: Distribution of the 20-100 keV luminosity for Type 1 (red) and Type 2 (blue) AGN. The two distributions have a slightly different peak.

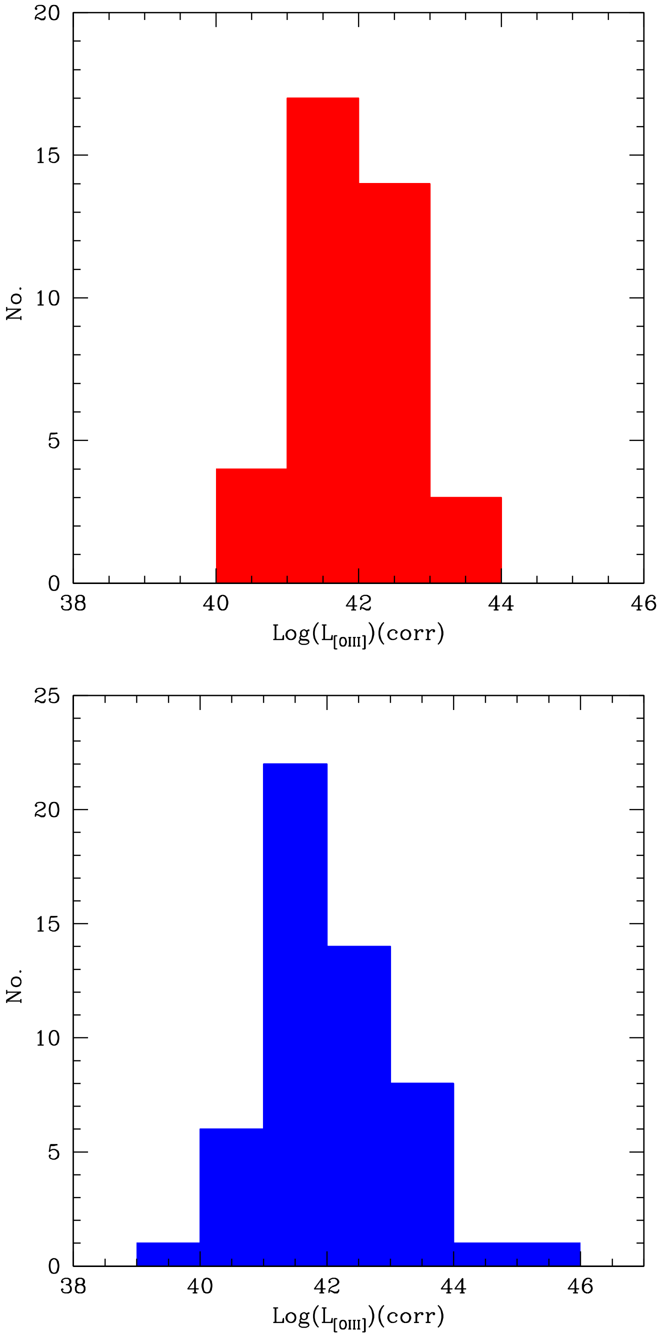

Figure 5.9: Distribution of the [OIII] luminosity for Type 1 (red) and Type 2 (blue) AGN. The two distributions have a slightly different peak.

5.4 Optical versus X-ray extinction

Various studies have shown that X-ray and optical nuclear absorption do not always match in AGNs. In particular, the measured optical extinction seem to be lower than that inferred from the absorption measured in X-rays, assuming a Galactic gas-to-dust ratio (Maiolino et al. 2001, Winter et al 2010); this evidence comes so far from studies done on small samples of AGN. This is an important effect since it could provide important observational consequences such as a mismatch between optical and X-ray classification. From our analysis, we found that the Balmer decrement and hence the reddening E(B-V) is lower in the broad line than in the narrow line sources; this is similar to what observed in X-rays where type 1 objects tend to have lower absorbing column densities than type 2 AGN. Therefore we do not expect a big mismatch between the optical and the X-ray classification. Clearly a one to one comparison is necessary and now possible with our sample of AGN. For this, we use the E(B-V) calculated from the Balmer decrement (see Tab. 5.4 and 5.4) as described in the previous section and the X-ray column density estimated from the X-ray spectra discussed in the previous chapter. Following Maiolino et al. (2001), we choose to show in Figure 5.10 the E_{B-V}/N_H ratio as a function of the 20-100 keV luminosity; the dotted line reported in the figure represents the standard Galactic gas to dust ratio.

We find that the E_{B-V}/N_H ratio is around the Galactic standard for the majority of type 1 sources; the only two exceptions are IGR J12107+3822 and IGR J09253+6929, which have a very low Log (E_{B-V}/N_H). Both have a conspicuous X-ray column density and are intermediate Seyferts (see table 6.4). The first source has a good 2-10 keV spectrum and so we can assume that the value of the X-ray column density is well constrained; this could be an intermediate Seyfert with complex absorption where we see the nucleus not directly, but at some inclination angle so that our line of sight intercepts thicker material from the torus. The second source has a low quality X-ray spectrum with huge errors in the estimate of the N_H and a fixed photon index; it is possible that, with better statistics, its position in the graph shifts to a E_{B-V}/N_H ratio closer

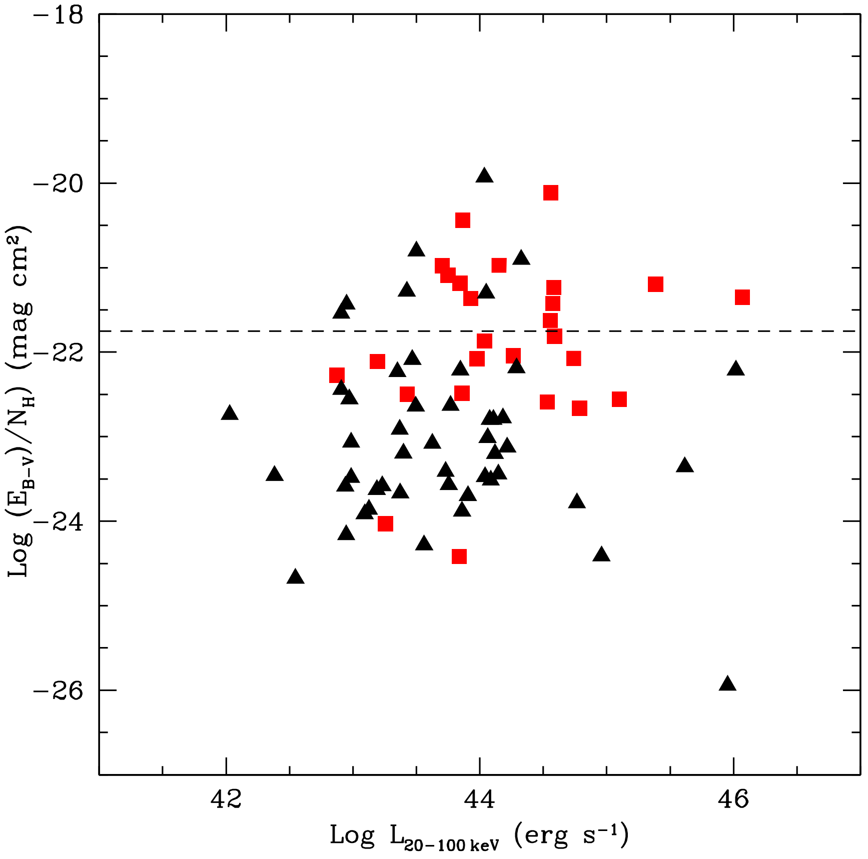

Figure 5.10: This plot shows the E_{B-V}/N_H ratio versus the 20-100 keV luminosity. The dashed line is the Galactic standard value. In the plot red squares show type 1 AGN, while black triangles show type 2 AGN.

to the dotted line.

Concerning the more heavily absorbed X-ray type 2 sources, we observe two typologies: those with an E$_{B-V}$/N$_H$ ratio not very different from the galactic values and those substantially lower than the Galactic standard by a factor of 10-100. In the first group we find seven sources, SWIFT J0107.8-1137, SWIFT J0122.3+5004, IGR J03344+1506, SWIFT J0347.0-3025, SWIFT J0654+0703, IGR J0917-6454 and IGR J19077-3925; three of these (SWIFT J0107.8-1137, SWIFT J0122.3+5004, IGR J03344+1506) are the Compton thick candidates, encountered in the previous chapter; their observed N$_H$ values could be by far much smaller than their true values and so their position in the figure could shift to a lower region. SWIFT J0347.0-3025 is most likely a naked Seyfert 2, i.e. in which the broad line region is not present rather than being hidden; its location in the plot should be similar to that of type 1 AGN. If anything, this confirms the atypical nature of this type 2 AGN. In the second group we found the majority of our type 2 AGN. Thus only 3 type 2 AGN, SWIFT J0654+0703, IGR J0917-6454 and IGR J19077-3925, which are all of intermediate type 1.9, are misplaced with respect to the majority of type 2 AGN. To conclude, we find that, with respect to the work of Maiolino et al. (2001) and more recently Winter et al. (2010), our results are somehow different. In our sample, not all bright AGN, but only a fraction, show a E$_{B-V}$/N$_H$ ratio lower than the Galactic standard; these somehow 'anomalous' objects are in general type 2 objects. Indeed our type 1 AGN show similar amount of reddening in optical and X-rays which strongly suggest that their circumnuclear region has a gas to dust ratio similar to the Galactic one. It is difficult to understand why we get such different results than those of Maiolino et al. (2001) although we note that their sample is much smaller than ours (19 versus 94 AGN) and dominated by intermediate Seyferts (type 1.8-1.9); these objects are similar to Seyfert 2 (and as such have been classified as type 2 in our sample) and so are expected to populate a region much below the Galactic standard line. The fact that we find evidence for a lower E$_{B-V}$/N$_H$ ratio with respect to the galactic value only in type 2 objects clearly points to an effect related to the obscuring torus. As explained by Maiolino et al.

(2001) the dust in the circumnuclear absorbing region could have different characteristics than observed in our Galaxy: the dust grains could be larger therefore being less effective in absorbing optical-UV radiation. Alternatively the X-ray absorbing medium is located in a dust free region, for example due to the sublimation of the dust in regions of high temperatures, which naturally explains a less optical absorption and a reduced E_{B-V}/N_H value.

5.5 Unified theory and obscuring torus

From the above analysis of the optical and X-ray properties of our AGN we conclude that the standard unification theory of AGN still holds, although some modifications may be required to fit all types of objects. One of these modifications maybe a luminosity dependence often discussed in the literature: for example, the disappearance of the broad line region at low luminosities (Tran 2001; Gu & Huang 2002) has been invoked to explain naked Seyfert 2 AGN, i.e. objects where the BLR is not hidden, but simply not present due to the low power of the central engine. A more interesting modification can be the type of torus present in the AGN. From basic considerations, Krolik & Begelman (1988) concluded that the obscuration probably consists of a large number of individually very optically thick dusty clouds. For a long time, the important role of clumpiness was neglected or not fully appreciated and many considerations on absorption have been based on a smooth density torus (see sketch in figure 5.11 for the two types of configuration). Recently clumpy torus models have gained interest as they are able to explain many observational evidences which are incompatible with the smooth density (or doughnut type) torus (Elitzur 2008).

Indeed, because of clumpiness, the difference between type 1 and 2 objects is not truly an issue of orientation but rather of probability of direct viewing of the AGN. In other words, the probability of direct viewing of the central engine decreases away from the axis but is always finite. As a consequence, type 1 sources can be detected from what are typically considered type

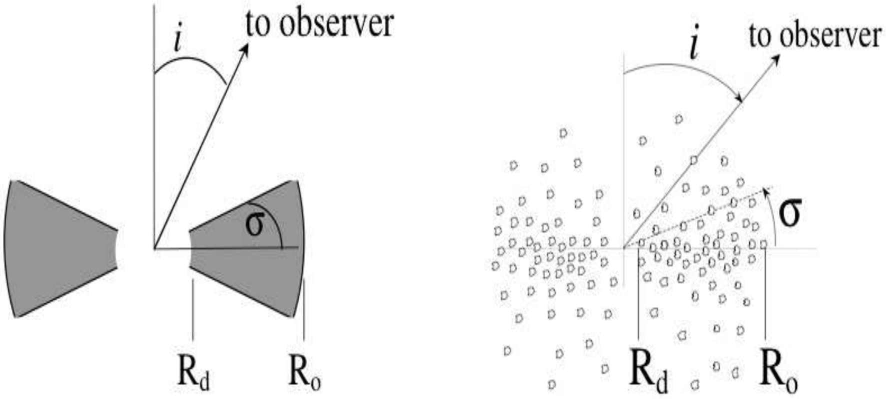

Figure 5.11: This sketch shows the AGN model according to unified model. In the Left part of the figure we have a smooth-density torus, where the observed angle discriminates the type 1 and type 2 AGN. In the right side is shown a clumpy, soft-edge torus (Elitzur 2008).

2 orientations, even through the torus equatorial plane. This might offer an explanation for the few Seyfert 1 galaxies found to show high absorption. Conversely, if a cloud happens to obscure the AGN from an observer, that object would be classified as type 2 irrespective of the viewing angle. Clouds can also move in and out of the line-of-sight, creating or not a clear path to the nucleus: this can explain transition objects which move from type 1 to type 2 spectra with time. Such transitions have been observed in a few sources (see Aretxaga et al., 1999, and references therein). Indeed optical classification is not monitored in time and so an AGN type could be just the result of an occasional change in class. The clumpy torus model could also naturally explain the different absorption observed in X-rays and optical; this is because the torus is a smooth continuation of the broad line region (BLR), not a separate entity. The different radiative signatures merely reflect the change in cloud composition across the dust sublimation radius R_d[2]. In the inner clumpy torus the inner clouds are dust free and contain only gas. This gas is directly exposed to the AGN ionizing continuum, therefore it is atomic and ionized, producing the broad emission lines. The outer clouds are gaseous and dusty; thus gas is shielded from the

---

[2] The radius below which dust is destroyed due to the presence of a strong AGN radiation field

ionizing radiation, and the atomic line emission is quenched; these clouds are molecular, obscure the optical/UV emission from the inner regions and emit mostly in IR. Thus the BLR is located within a radius r $<$ R$_d$, while the torus is simply located in region with a radius r $>$ R$_d$ and a more appropriate designation for it is the 'toroidal obscuration region' (TOR). Since every cloud that attenuates the optical/UV continuum contributes also to the X-ray obscuration, but not the other way round, the X-ray absorbing column may exceed the UV/optical absorbing column, as indeed observed in some sources. In type 1 AGN the optical absorption is low and related to BLR and NLR, but also the X-ray absorption is normally low resulting in a gas to dust ratio similar to our galaxy. In type 2 AGN instead the X-ray absorption, broad line emission, dust obscuration and reprocessing are produced by a single, continuous distribution of clouds. the combination of clumpiness and radius dependent dust-to-gas ratios allow one to find sources with differing X-ray and optical absorption.

The BLR/TOR structure arises naturally in the disk-wind scenario, first proposed by Emmering et al. (1992). In this model, the two classes of clouds simply correspond to different regions of a clumpy wind coming off the accretion disk rotating around the black hole (see Elitzur & Shlosman 2006, and references therein). As the clouds rise away from the disk they expand and lose their column density, limiting the optical thickness of broad-line emission, dust obscuration and continuum emission, resulting in a toroidal geometry for both the BLR and the TOR. Although a theory of clumpy disk winds in AGNs is far from full development, an immediate consequence of this scenario is the prediction that the TOR and BLR disappear at low bolometric luminosities (i.e., low accretion rates; Elitzur & Shlosman 2006; Elitzur 2008) because mass accretion can no longer sustain the required cloud outflow rate, i.e., the large column densities (Elitzur & Shlosman, 2006). As a consequence the BLR and TOR may disappear either together or in sequence; this naturally explains why we see 'naked' Seyefert 2 objects in which the toroidal obscuration has disappeared as well as the BLR. As the outflow diminishes, the accreted mass is no longer fully channeled into the central black hole, but it is rather funneled into the radio jets, whose feeding thus saturates at a high conversion efficiency of accreted mass.

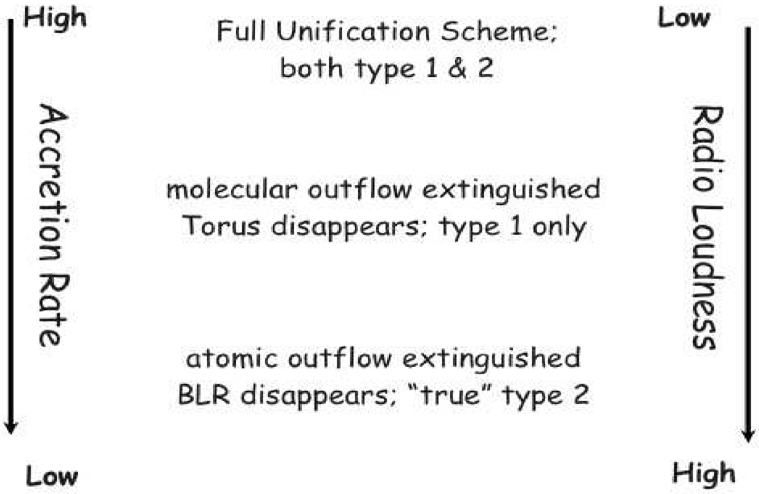

Figure 5.12: Scheme for AGN evolution, taking into account the role of accretion rate.

Indeed, Ho (2002) finds that the AGN radio loudness R = L_{Radio}/L_{Opt} is inversely correlated with the mass accretion rate L/L_{Edd}. This finding is supported by Sikora et al. (2007), who have greatly expanded this correlation and found an intriguing result: R indeed increases inversely with L/L_{Edd}, but only as long as L/L_{Edd} remains 10^{-3}. At smaller accretion rates, the radio loudness saturates and remains constant at $R \sim 10^4$. This is precisely the behaviour expected if, as the outflow diminishes, the jets are fed by an increasingly larger fraction of the accreted mass.

The evolutionary scheme just outlined is sketched in figure 5.12 and provide the basis for the so called Grand Unification Theory for AGN, which requires only the accretion disk and the clumpy outflow, it generates to explain various aspects of AGN observations, including source classification, radio loudness and low luminosity AGN.

5.6 Conclusions

In this chapter we have compared X-ray and optical properties of our hard X-ray selected AGN sample. In particular we have estimated the X-ray to optical flux ratios for our sample compared to those obtained in other, softer X-ray selected samples. We find that about half of our sources have Log(F_{2-10}/F_R) ratios typical of AGN, with only few having Log($F_2 - 10$/F_R) $\geq$+1, while another half populates the area characterized by values of Log(F_x/F_{opt}) $\leq$-1; objects at these low ratios are in general heavily absorbed AGN, including some Compton thick candidates. This suggests that absorption plays an important role. Indeed, when we use the 20-100 keV fluxes instead of the 2-10 keV ones we observe less evidence of this effect: the distribution of Log(F_{20-100}/F_R) for type 1 and 2 AGN are comparable with each other and only a fraction of sources have the logarithms of the ratios below -1. This can be explained either with the presence in these sources of very strong absorption (a few 10^{23}-10^{25} at cm^{-2} in column density) or of a very bright galaxy which may be particularly visible in nearby objects. In the first case we may have not properly corrected the hard X-ray fluxes for the high column density present in mildly and heavily absorbed Compton thick objects, while in the second case the galaxy flux clearly contaminates the nuclear emission. These two combined effects provide higher 20-100 keV emission and a lower optical nuclear AGN radiation and hence a higher observed Log(F_x/F_{opt}) ratio. Overall we can conclude that we do not find strong evidences for many of the so called ‘unconventional’ AGN often discussed in literature and that our hard X-ray selected objects fit quite well within the optical versus X-ray boundaries expected for active galaxies.

Next we investigated if the [OIII] emission line is a reliable indicator of AGN activity as the X-ray continuum. To do this, we first corrected the [OIII] luminosity for large scale obscuration in the host galaxy using the Balmer decrement and then correlated this quantity with the hard X-ray luminosity. The average H_α/H_β for our entire sample is 4.5±3.2 (corresponding to E(B-V) = 0.478 mag); the mean Balmer decrement becomes as expected 2.8±1.8 for type 1 sources and

6.14±3.42 for type 2 objects, in line with previous studies.

In agreement with previous works (Winter et al. 2010; Melendez et al. 2008) we do not find evidence for a strong correlation between the [OIII] and 20-100 keV luminosities using the entire sample or type 1 and type 2 AGN separately. This means that the [OIII] luminosity can only predict the hard X-ray luminosity with a large uncertainty.

Concerning the optical and X-ray extinction, we have compared the X-ray column density estimated from the X-ray spectroscopy with the E(B-V) values evaluated using the Balmer decrement. We find that the E_{B-V}/N_H ratio is generally around the Galactic standard value for the type 1 objects, while for the more heavily absorbed type 2 sources, the E_{B-V}/N_H ratio is lower than the Galactic standard value by a factor of 10-100.

All these findings give support for the clumpy torus model and torus as a wind scenarios. Indeed the clumpy nature of the obscuring material dictates a fundamental change in our approach to some basic issues regarding AGN. Because of clumpiness, the difference between types 1 and 2 is not truly an issue of orientation, but of probability of direct view of the AGN. Since this probability is always finite, type 1 sources can be detected from what are typically considered type 2 orientations. Conversely, if a cloud happens to obscure the AGN from an observer, that object would be classified as type 2 irrespective of the viewing angle.

In the clumpy torus, X-ray absorption, broad line emission, dust obscuration and reprocessing are produced by a single, continuous distribution of clouds. The different radiative signatures merely reflect the change in cloud composition across the dust sublimation radius. The inner clouds are dust free while the outer clouds contain dust.

Dusty material absorbs continuum radiation both in the UV/optical and X-rays, therefore the dusty part also provides X-ray obscuration. But dust-free gas attenuates just the X-ray continuum, so clouds inside the dust sublimation radius will provide additional obscuration only in this band. Hence a different gas to dust ratio in type 2 and type 1 AGN could be a natural consequence of cloud composition/ location. Finally all torus clouds are embedded in a disk wind, whose mass outflow rate diminishes as the accretion rate, i.e., the AGN luminosity, decreases. As this happens, first the torus and then the BLR disappear and the a source can be classified as a naked type 2 AGN.

As the outflow diminishes, the accreted mass is no longer fully channeled into the central black hole, but goes to feed the radio jets: as a consequence the source radio loudness increases. Thus AGN are expected to switch their main dynamic channel for release of excess accreted mass from torus outflow at higher luminosities to radio jets at lower ones, following a behaviour already observed in X-ray binaries.

In this newly developed model, not only the torus width, but also the mean number of clouds are important. Unfortunately it is quite hard to determine both parameters together; meaningful constraints on the torus physical properties can be placed only through a combination of different types of data. Comparisons of UV/optical and X- ray properties in individual sources and in samples of AGN offer especially promising analysis modes for deducing detailed torus properties. The low-luminosity end of AGN also offers a rich variety of interesting phenomena. Detailed observational and theoretical studies of these phenomena would enhance significantly our understanding of the black-hole environment.

Table 5.1: X-ray/optical information of sources belonging to *INTEGRAL*/IBIS catalogue.

Source	$F_{20-100keV}{}^{a}$	R magnitude	$F_{[OIII]}{}^{b}$	$E(B-V)_{intr}$
IGR J00158+5605	0.66	17	9.4	0
IGR J00333+6122	1.38	18.5	5.8	1.23
IGR J00465−4005	3.56	16.6	16.3	1.24
IGR J01545+6437	0.84	14.8	79.4	0.39
IGR J02086−1742	2.75	15.8	4.2	0
SWIFT J0216.3+5128	1.62	18.5	0.4	0.77^{*}
IGR J02524−0829	3.93	11	2.8	0.77^{*}
SWIFT J0255.2−0011	6.12	8.2	104.7	1.16
IGR J03344+1506	2.66	12.6	58.7	0.78
SWIFT J0505.7−2348	5.49	14	18.1	0.39
SWIFT J0519.5−3140	4.34	8.4	51.4	0.13
SWIFT J0605.8−2754	1.9	14.7	72.2	0.75
SWIFT J0640.4−2554	3.83	9.1	0.3	0
SWIFT J0855.6+6425	2.54	12.6	12.9	0.39^{*}
IGR J09253+6929	1.94	13.4	3.8	0.06
IGR J10147−6354	1.07	14.7	2.2	0.48
IGR J10470+2554	3.19	9.9	1.4	0
IGR J11456−6956	1.36	16.1	0.2	1.02
IGR J12107+3822	1.52	11.6	7.8	0.04
IGR J12415−5750	2.04	12.9	57.1	0.09
IGR J12479−5829	1.02	14.8	4.4	0
IGR J13168−7157	1.19	13.9	9.2	1.72
IGR J13415+3033	1.85	10.1	–	0.39^{*}
IGR J13466+1921	2.03	14	25.9	1.39
IGR J14301−4158	0.9	14.5	14.5	0.31
SWIFT J1513.8−8125	1.59	14.1	8.3	0.69
IGR J15311−3737	0.89	16.7	1.7	0.41
IGR J16351−5806	1.96	12.5	1369.8	0.78
IGR J16426+6536	3.45	18.9	0.1	0.12^{*}
IGR J17009+3559	1.77	14.4	–	0.39^{*}
IGR J18078+1123	3.68	14.9	1.9	0.55
IGR J18249−3243	1.02	15.1	1.5	0^{*}

Table 5.4: – *continued*

Source	$F_{20-100keV}$[a]	F_R	$F_{[OIII]}$[b]	E(B-V)$_{intr}$
IGR J18311−3337	1.71	14.2	230.9	0.91
IGR J19077−3925	1.51	13.4	580.1	1.74
IGR J19118−1707	0.71	11.9	28.7	0.27
SWIFT J2118.9+3336	1.55	12.1	9.8	0.39
IGR J21398+5950	1.02	18.7	7.4	0.01*
IGR J22292+6647	1.11	18.6	2.5	0.64
IGR J23524+5842	1.23	18.5	2.0	0.04*

[a] In units of 10^{-11} erg cm^{-2} s^{-1};

[b] In units of 10^{-14} erg cm^{-2} s^{-1};

* The E(B-V)$_{intr}$ is estimated from the mean H_α/H_β values (2.79 for type 1 AGN and 6.14 for type 2 AGN);

Table 5.5: X-ray/optical information of sources belonging to *Swift*/BAT catalogue.

Source	$F_{20-100keV}{}^a$	R magnitude	$F_{[OIII]}{}^b$	$E(B-V)_{intr}$
SWIFT J0034.6−0422	0.81	16.8	19.6	0^*
SWIFT J0038.5+2336	0.68	10.9	9.7	0.39^*
SWIFT J0059.4+3150	2.57	10.3	4.6	0.01^*
SWIFT J0107.8−1137	0.61	13.3	13.5	0.39^*
SWIFT J0122.3+5004	0.81	11.3	477.1	0.39
SWIFT J0134.1−3625	1.89	8.4	5.9	0.39^*
SWIFT J0154.7−2707	0.95	14.2	55.1	0.11
SWIFT J0226.7−2819	0.81	13.5	4.8	0.41
SWIFT J0238.3−6116	0.61	12.7	8.3	0.39^*
SWIFT J0248.7+2626	1.81	13.6	161.5	1.26
SWIFT J0250.3+4645	0.81	15.5	80.1	0.61
SWIFT J0342.0−2115	2.82	9.3	47.5	0.01^*
SWIFT J0347.0−3025	0.48	16.1	75.5	1.17
SWIFT J0350.1−5019	1.91	12.1	8.0	0.65
SWIFT J0353.5+3713	1.15	12.9	23.4	0.94
SWIFT J0459.9+2703	1.29	16.2	1197.6	1.05
SWIFT J0503.0+2300	1.36	14.4	177.6	0.46
SWIFT J0505.7−2348	4.41	14	17.6	0.38
SWIFT J0535.4+4013	0.75	15.3	20.0	0.20
SWIFT J0544.3+5910	1.36	15.5	4.2	0.45
SWIFT J0552.5+5929	1.02	13.1	39.7	0.54
SWIFT J0640.1−4328	1.23	12.9	0.9	0.41
SWIFT J0654.5+0703	0.68	12.4	518.9	1.19
SWIFT J0739.6−3144	1.53	11.4	473.6	1.01
SWIFT J0814.4+0821	1.36	10.8	4.1	0
SWIFT J0845.0−3531	0.68	17.2	0.9	0.57
SWIFT J0855.8−2855	0.54	15.2	14.3	0.39^*
SWIFT J0902.0+6007	0.75	9.8	119.6	0.39^*
SWIFT J0904.3+5538	0.48	13.5	2.5	1.05^*
SWIFT J0911.2+4533	0.81	13.1	4.6	0.39^*
SWIFT J0917.2−6221	1.91	11.5	83.9	0
SWIFT J0917.2−6454	0.61	17	82.1	0.59
SWIFT J0923.7−2134	0.81	12.3	5.0	0.38
SWIFT J0923.7+2255	1.9	10.1	11.0	0.33
SWIFT J0942.1+2342	0.75	10.9	7.1	0
SWIFT J1017.0−0404	0.75	13.7	63.7	1.31

Table 5.4: – *continued*

Source	$F_{20-100keV}$ [a]	F_R	$F_{[OIII]}$ [b]	E(B-V)$_{intr}$
SWIFT J1049.4+2258	2.27	12.6	99.0	0.77
SWIFT J1115.3+5425	0.48	13.3	98.5	1.15
SWIFT J1145.4+5858	0.75	9.5	–	0.39*
SWIFT J1207.5+3355	0.81	13	37.1	0.69
SWIFT J1246.9+5433	1.9	8.7	18.7	0.39*
SWIFT J1254.8−2655	0.81	11.4	38.1	0.85
SWIFT J1321.1+0858	0.68	10.2	6.8	0.67
SWIFT J1416.8−1158	0.88	14.4	7.9	0
SWIFT J1439.2+1417	0.95	14.4	–	0.39*
SWIFT J1453.0+2553	1.29	15.2	2.1	1.21
SWIFT J1540.3+1415	0.61	15.5	3.0	0
SWIFT J1546.5+6931	0.27	12.4	11.3	0.39*
SWIFT J1620.3+8101	0.68	11.6	33.9	0.87
SWIFT J2150.9+1402	0.75	10.5	2.6	0
SWIFT J2254.3+1146	1.22	11.5	103.1	1.46
SWIFT J2327.4+0939	1.9	18.3	–	–
SWIFT J2333.9−2343	0.88	11.5	17.1	0*
SWIFT J2341.8+3034	1.36	10.3	16.4	0.39*
SWIFT J2344.8−4245	0.61	17	68.0	0.01*

[a] In units of 10^{-11} erg cm^{-2} s^{-1};

[b] In units of 10^{-14} erg cm^{-2} s^{-1};

[*] The E(B-V)$_{intr}$ is estimated from the mean H_α/H_β values (2.79 for type 1 AGN and 6.14 for type 2 AGN);

Chapter 6

Conclusions

In this thesis we have selected a sample of unidentified and unclassified hard X-ray sources detected by the imagers IBIS and BAT on board of the *INTEGRAL* and *Swift* satellites. Through cross-correlation with catalogues in other wavebands, or by means of X-ray follow-up observations we have been able to identify the most likely counterparts of these hard X-rays objects and as a consequence to reduce their positional uncertainty from arcmin to arcsec. This procedure allowed us to identify the optical counterparts and to proceed with their classifications by means of optical follow-up spectroscopic observations.

With the above procedure we have been able to identify 148 recently detected hard X-ray sources of which 39 belong to the IBIS survey and 55 belong to the BAT one. In particular we found that 121 objects are AGN, while 27 are X-ray binaries.

Optical continuum spectra, emission line properties and distances are some of the information provided for all these sources. Of the 121 AGN, 48 show optical spectra typical of type 1 AGN while 69 display spectra characteristic of type 2 AGN; 4 objects have optical spectra of normal galaxies and have been classified as XBONG (X-ray bright optical normal galaxies). Within the AGN population we found mainly Seyfert 1 and 2, a few Narrow Line Syefert 1, some Liners and only one source which could not be classified properly. Of the 27 X-ray binaries, 18 are CV and 9 are HMXB (one of these is a sg[Be] X-ray binary).

For 94 of the objects identified as AGN, we have also done X-ray spectroscopic studies by means of *Swift*/XRT and *XMM*/Epic observations. This allows us to provide an estimate of the mean spectral index (which is found to be 1.83±0.3) and of the X-ray absorption. We found that 74% of these AGN have a column density in excess of 10^{22} cm^{-2} and that the majority of these absorbed sources are type 2 objects. We also used a new diagnostic diagram, which employes the X-ray column density versus the $F_{2-10\ keV}/F_{20-100\ keV}$ flux ratio to isolate peculiar AGN. As a result we found: a) two heavily absorbed Seyfert 1; b) four Compton thick AGN candidates; c) two Seyfert 2 likely to be naked type 2 objects, i.e. sources in which the BLR is not present. Finally, in the last part of the thesis we have compared the optical properties of these 94 AGN with their X-ray characteristics and discussed our overall results within the framework of the recently proposed clumpy torus models and disk-wind scenario.

We started comparing the X-ray luminosities (2-10 keV) and 20-100 keV) with the R magnitudes to look for the so called unconventional AGN, i.e. those which are not compatible with the unified theory. Overall, we did not find too many objects behaving unconventionally and even these sources could be explained in terms of unaccounted X-ray absorption and bright host galaxies.

We did not find a significant correlation between the corrected [OIII] and hard X-ray flux either employing the total sample or type 1 and type 2 objects separately. This means that the [OIII] can predict the hard X-ray luminosity with a large uncertainty.

Finally we compare optical versus X-ray absorption providing evidence that, while both absorption match in type 1 AGN, their ratio is lower in type 2 AGN, most likely due to changing conditions of dust in the torus of these AGN.

While some of our results seemed, in first instance, in disagreement with the Unified Theory of AGN, they found a natural explanation in the framework of clumpy model and disk-wind scenario. In particular, we can explain the observations of peculiar sources such as absorbed type

1 AGN, naked seyfert 2 galaxies and a different optical versus X-ray absorption ratio in type 1 and type 2 objects. Dedicated studies both in the X-ray and optical waveband of these peculiar AGN could provide further information on these objects and a practical test of our proposed scenario.

Table 6.1: *SWIFT*/BAT sample of AGN and log of their X-ray observations.

Source	Class	Instrument	Exposure [a]	Count rate [b]	$N_{\mathrm{H}}(Gal)^c$
SWIFT J0034.6−0422	Sy2	XRT	8471	5.1±0.8	0.35
SWIFT J0038.5+2336	Sy2	XRT	5331	13.5±1.6	0.30
SWIFT J0059.4+3150	Sy1.2	XMM	30880	235.4±2.8	0.52
SWIFT J0107.8−1137	Sy2	XRT	15040	19.5± 1.1	0.25
SWIFT J0122.3+5004	Sy2	XRT	8430	8.9±1.0	1.36
SWIFT J0134.1−3625	Sy2	XRT	11560	9.1±0.9	0.20
SWIFT J0154.7−2707	Sy1/1.2	XRT	6624	117.7±4.2	0.15
SWIFT J0226.7−2819	Sy1.5	XRT	10290	99.2±3.1	0.17
SWIFT J0238.3−6116	Sy2	XRT	5637	65.9±3.4	0.24
SWIFT J0248.7+2626	Sy2	XRT	5156	14.0±1.7	1.03
SWIFT J0250.3+4645	Sy2	XRT	10180	42.3±2.0	1.47
SWIFT J0342.0−2115	Sy1	XRT	10140	457.3±6.7	0.23
SWIFT J0347.0−3025	Sy2/HII region	XRT	8150	108.2± 3.7	0.10
SWIFT J0350.1−5019	Sy2	XRT	13980	20.4±1.2	0.12
SWIFT J0353.5+3713	LINER	XRT	8647	31.8 ± 1.9	1.68
SWIFT J0459.9+2703	Sy2	XRT	9321	17.9 ± 1.4	3.10
SWIFT J0503.0+2300	Sy1.5	XRT	9229	419.3 ± 6.8	2.26
SWIFT J0505.7−2348	Sy2	XRT	10280	130.4±3.6	0.21
SWIFT J0535.4+4013	Sy1.5	XRT	16190	45.2 ± 1.7	3.74
SWIFT J0544.3+5910	Sy2	XRT	10430	41.4 ± 2.0	1.58
SWIFT J0552.5+5929	Sy1.2	XRT	7767	259.7 ± 5.8	1.24
SWIFT J0640.1−4328	Sy2	XRT	18840	10.6 ± 0.7	0.55
SWIFT J0654.5+0703	Sy1.9	XRT	12770	193.2 ± 3.9	2.91
SWIFT J0739.6−3144	Sy2	XMM	20630	79.0±2.1	4.31
SWIFT J0814.4+0821	Sy1.5	XRT	4470	13.3 ± 1.7	0.32
SWIFT J0845.0−3531	Sy1.2	XRT	9153	84.1 ± 3.0	2.71
SWIFT J0855.8−2855	Sy2	XRT	7198	38.7±2.3	1.29
SWIFT J0902.0+6007	Sy2	XRT	9363	8.3±0.9	0.44
SWIFT J0904.3+5538	Sy1.5	XRT	12840	136.5±3.3	0.22
SWIFT J0911.2+4533	Sy2.0	XRT	14930	8.8±0.8	0.12

Table 6.1: – *continued*

Source	Class	Instrument	Exposure[a]	Count rate[b]	$N_{\mathrm{H}}(Gal)$ [c]
SWIFT J0917.2−6221	Sy1.2	XRT	12870	264.1±4.5	1.58
SWIFT J0917.2−6454	Sy1.9/2	XRT	5354	96 ± 4.2	1.33
SWIFT J0923.7−2134	Sy1.5/1.8	XMM	13150	3329 ± 16	0.47
SWIFT J0923.7+2255	NLSy1	XRT	9093	403.2±6.7	0.31
SWIFT J0942.1+2342	Sy1.5	XRT	5302	76.1±3.8	0.26
SWIFT J1017.0−0404	Sy2	XRT	8231	34.8±2.1	0.37
SWIFT J1049.4+2258	Sy2	XRT	22600	7.3±0.6	0.19
SWIFT J1115.3+5425	Sy2	XRT	4701	12.7±1.6	0.08
SWIFT J1145.4+5858	likely Sy2	XRT	8858	43.6±2.2	0.13
SWIFT J1207.5+3355	Sy2	XRT	8678	11.4±1.2	0.14
SWIFT J1246.9+5433	Sy2	XMM	15090	46.7±1.8	0.14
SWIFT J1254.8−2655	Sy1.5	XRT	5855	174.2 ± 5.5	0.66
SWIFT J1321.1+0858	Sy2/LINER	XRT	7789	948.4±1.1	0.17
SWIFT J1416.8−1158	Sy1.5/1.8	XRT	4722	251.6±7.3	0.56
SWIFT J1439.2+1417	Sy 2	XRT	5265	31.4±2.4	0.14
SWIFT J1453.0+2553	Sy1	XRT	5424	366.81±8.2	0.33
SWIFT J1540.3+1415	Sy1.2	XRT	6770	60.3 ±3.0	0.34
SWIFT J1546.5+6931	Sy1.9	XRT	9950	4.3±0.7	0.31
SWIFT J1620.3+8101	Sy2	XRT	9506	31.2±1.8	0.46
SWIFT J2150.9+1402	Sy2	XRT	5352	8.3±1.3	0.62
SWIFT J2254.3+1146	Sy2	XRT	6630	17.9±1.7	0.50
SWIFT J2327.4+0939	?	XRT	5674	70.7±3.5	0.40
SWIFT J2333.9−2343	Sy2	XRT	8958	285.6±5.7	0.16
SWIFT J2341.8+3034	Sy2	XMM	11220	57.7±3.0	0.58
SWIFT J2344.8−4245	type 2 QSO	XRT	8430	145.3 ± 4.2	0.15

[a] In units of seconds;

[b] In units of 10^{-3} counts s^{-1};

[c] In units of 10^{21} cm^{-2}

Table 6.2: Sample of the *INTEGRAL*/IBIS AGN and log of their X-ray observations.

Source	Class	Instrument	Exposure [a]	Count rate [b]	$N_{\rm H}(Gal)$ [c]
IGR J00158+5605	Sy 1.5	XRT	4028	30.4 ± 2.8	3.14
IGR J00333+6122	Sy 1.5	XRT	6021	86.1 ± 3.8	5.55
IGR J00465−4005	Sy 2	XRT	11510	5.6 ± 0.7	0.345
IGR J01545+6437	Sy 2	XRT	4428	2.5 ± 0.8	6.67
IGR J02086−1742	Sy 1.2	XRT	4939	161.0 ± 5.7	0.254
SWIFT J0216.3+5128	Sy 2	XRT	16400	170.5 ± 3.2	1.42
IGR J02524−0829	Sy 2	XRT	15430	40.8 ± 5.9	0.460
SWIFT J0255.2−0011	Sy 2	XRT	6803	32.6±2.2	0.58
IGR J03344+1506	Sy 2	XRT	4317	3.3 ± 0.9	1.48
SWIFT J0505.7−2348	Sy 2	XRT	9305	141.8 ± 3.9	0.212
SWIFT J0519.5−3140	Sy 2	XRT	8794	375.9 ± 6.5	0.175
SWIFT J0605.8−2754	Sy 1.5	XRT	3875	236.9±7.8	0.24
SWIFT J0640.4−2554	Sy 1.9	XRT	14130	419.2 ± 5.4	1.07
SWIFT J0855.6+6425	likely Sy 2	XRT	5591	5.09±0.98	0.47
IGR J09253+6929	Sy 1.5	XRT	5282	2.2 ± 0.7	0.489
IGR J10147−6354	Sy 1.2	XRT	4520	19.1 ± 2.1	3.10
IGR J10470+2554	LINER	XRT	11550	21.7 ± 1.4	2.51
IGR J11456−6956	Sy 1.2	XRT	9149	151.5 ± 4.1	1.62
IGR J12107+3822	Sy 1.5	XMM	6809	282.3±6.4	0.18
IGR J12415−5750	Sy 1.5	XRT	12840	136.6 ± 3.3	3.01
IGR J12479−5829	Sy 1.9	XRT	5566	30.7 ± 2.3	2.97
IGR J13168−7157	Sy 1.5	XRT	7448	93.5±3.6	1.62
IGR J13415+3033*	Sy 2	XMM	28212	199.7 ± 3.5	0.137
IGR J13466+1921	Sy 1.5	XRT	9478	101.2±3.3	0.18
IGR J14301−4158	Sy 2	XRT	5521	37.2 ± 2.6	0.748
SWIFT J1513.8−8125	Sy 1.2	XRT	5312	161.0±5.5	0.94
IGR J15311−3737	Sy 1	XRT	4569	57.1 ± 3.6	1.08
IGR J16351−5806	Sy 2	XMM	21514	85.0 ± 2.3	2.28

Table 6.3: – *continued*

Source	Class	Instrument	Exposure [a]	Count rate [b]	$N_{\rm H}(Gal)$ [c]
IGR J16426+6536	NLSy1	XRT	5099	3.4 ± 0.9	0.258
IGR J17009+3559	XBONG	XRT	4872	5.7 ± 1.1	0.179
IGR J18078+1123	Sy 1/1.2	XRT	9867	158.7±14.0	0.74
IGR J18249−3243	Sy 1	XRT	4592	112.2 ± 5.0	1.18
IGR J18311−3337	Sy 2	XRT	4152	3.6 ± 1.1	1.05
IGR J19077−3925	Sy 1.9	XRT	4776	90.3 ± 4.4	0.737
IGR J19118−1707	LINER	XRT	4615	5.9 ± 1.2	0.827
SWIFT J2118.9+3336	Sy 1.5	XRT	5856	116.8±4.5	1.33
IGR J21398+5950	Sy 1.5	XMM	8333	910.0±10.6	5.69
IGR J22292+6647	Sy 1.5	XRT	19600	84.7 ± 2.1	4.81
IGR J23524+5842	Sy 2	XRT	5878	10.7 ± 1.4	5.06

[a] In units of seconds;

[b] In units of 10^{-3} counts s^{-1};

[c] In units of 10^{21} cm^{-2};

[*] Although this source is not in our sample of optically identified objects, we included it here because it is identified with the type 2 AGN MKN 268 and we have X-ray data available

Table 6.4: Spectral analysis of the *SWIFT*/BAT AGN sample. Frozen parameters are written in square brackets; errors are given at the 90 per cent confidence level.

Source	${N_{\rm H(intr)}}^{a}$	Γ^{b}	χ^2/ν	${F_{(2-10\ {\rm keV})}}^{c}$	$\frac{F_{(2-10\ {\rm keV})}}{F_{(20-100\ {\rm keV})}}$
SWIFT J0034.6−0422	$11.7^{+6.7}_{-4.5}$	[1.8]	1.35/1	0.09±0.01	0.111
SWIFT J0038.5+2336	$11.9^{+5.8}_{-3.6}$	[1.8]	0.82/2	0.23 ± 0.01	0.338
SWIFT J0059.4+3150	–	1.69 ± 0.03	322.7/250	0.72±0.01	0.280
SWIFT J0107.8−1137	–	$1.84^{+0.39}_{-0.34}$	14.1/14	0.06 ± 0.01	0.098
SWIFT J0122.3+5004	–	$1.9^{+0.43}_{-0.46}$	6.4/3	0.03 ± 0.01	0.037
SWIFT J0134.1−3625	75^{+34}_{-21}	[1.8]	1.1/4	0.19±0.03	0.101
SWIFT J0154.7−2707[1]	$0.51^{+0.52}_{-0.32}$	$1.63^{+0.32}_{-0.26}$	38.5/44	0.44 ± 0.03	0.463
SWIFT J0226.7−2819[2]	$1.25^{+0.44}_{-0.36}$	$1.81^{+0.25}_{-0.23}$	42.9/43	0.48 ± 0.02	0.592
SWIFT J0238.3−6116°	$4.71^{+4.29}_{-3.16}$ [0.8]	$2.28^{+1.01}_{-0.78}$	13.5/19	0.49 ± 0.03	0.803
SWIFT J0248.7+2626	$34.9^{+16.9}_{-11.7}$	[1.8]	3.5/3	0.41±0.01	0.227
SWIFT J0250.3+4645^{-}	$1.7^{+0.8}_{-1.6}$ [0.9]	$1.5^{+0.6}_{-0.5}$	29.12/22	0.44 ± 0.02	0.543
SWIFT J0342.0−2115	–	2.05 ± 0.04	224.7/160	2.17±0.07	0.769
SWIFT J0347.0−3025	–	1.74 ± 0.09	51.7/40	0.30 ± 0.02	0.625
SWIFT J0350.1−5019	$16.77^{+4.86}_{-3.80}$	[1.8]	14.9/18	0.31±0.02	0.163
SWIFT J0353.5+3713	$3.37^{+0.76}_{-0.63}$	[1.8]	19.5/16	0.33 ± 0.02	0.287
SWIFT J0459.9+2703	$10.76^{+2.71}_{-1.95}$	[1.8]	6.9/9	0.29 ± 0.02	0.225
SWIFT J0503.0+2300	$0.34^{+0.03}_{-0.02}$	2.08 ± 0.08	151.8/149	1.26 ± 0.04	0.926
SWIFT J0505.7−2348	6.0 ± 0.5	$1.4^{+0.3}_{-0.4}$	96.3/61	1.61±0.05	0.366
SWIFT J0535.4+4013	–	1.82 ± 0.11	48.6/44	0.21 ± 0.01	0.28
SWIFT J0544.3+5910	$2.67^{+0.56}_{-0.35}$	[1.8]	13.2/19	0.39 ± 0.02	0.287
SWIFT J0552.5+5929	–	2.13 ± 0.06	83.9/85	0.56 ± 0.02	0.549
SWIFT J0640.1−4328	$12.2^{+2.8}_{-2.1}$	[1.8]	9.3/11	0.23 ± 0.02	0.187
SWIFT J0654.5+0703	$0.32^{+0.05}_{-0.04}$	1.8 ± 0.1	97.9/103	0.89 ± 0.02	1.309
SWIFT J0739.6−3144^{+}	47^{+13}_{-12} [0.7]	$2.20^{+0.38}_{-0.23}$	174/151	0.091±0.003	0.059
SWIFT J0814.4+0821	$11.29^{+8.37}_{-4.22}$	[1.8]	3.0/2	0.26±0.04	0.191
SWIFT J0845.0−3531*	$2.23^{+1.08}_{-0.97}$ [0.7]	$1.9^{+0.39}_{-0.33}$	46/34	0.48 ± 0.02	0.706
SWIFT J0855.8−2855	$0.64^{+0.36}_{-0.27}$	$1.55^{+0.41}_{-0.36}$	15.8/15	0.27±0.02	0.5
SWIFT J0902.0+6007*	$11.34^{+4.55}_{-4.56}$ [0.9]	[1.8]	4.2/5	0.11 ± 0.02	0.147
SWIFT J0904.3+5538*	$1.36^{+0.56}_{-0.37}$ [0.6]	$2.01^{+0.20}_{-0.19}$	27.2/24	0.42±0.02	0.875
SWIFT J0911.2+4533	$28.4^{+8.4}_{-6.4}$	[1.8]	10.7/11	0.20±0.02	0.247
SWIFT J0917.2−6221	0.31±0.09	1.38±0.11	176.3/139	1.64±0.03	0.863
SWIFT J0917.2−6454	$0.12^{+0.09}_{-0.08}$	$1.75^{+0.23}_{-0.21}$	14.9/22	0.41±0.001	0.672
SWIFT J0923.7−2134	–	1.77±0.01	753.1/664	0.63±0.01	0.778
SWIFT J0923.7+2255	–	1.95±0.05	124.0/139	1.16±0.04	0.611
SWIFT J0942.1+2342*	$0.92^{+0.76}_{-0.47}$ [0.7]	$2.23^{+0.44}_{-0.48}$	21.7/16	0.20±0.02	0.267
SWIFT J1017.0−0404	$1.61^{+1.02}_{-0.63}$	$1.52^{+0.62}_{-0.48}$	11.3/11	0.39±0.03	0.52

Table 6.2: – *continued*

Source	$N_{\mathrm{H(intr)}}{}^{a}$	Γ^{b}	χ^2/ν	$F_{(2-10\ \mathrm{keV})}{}^{c}$	$\frac{F_{(2-10\ \mathrm{keV})}}{F_{(20-100\ \mathrm{keV})}}$
SWIFT J1049.4+2258[3]	$28.5^{+13.7}_{-10.5}$	[1.8]	17/7	0.09±0.01	0.04
SWIFT J1115.3+5425	$4.9^{+2.5}_{-1.6}$	[1.8]	0.8/2	0.24±0.04	0.5
SWIFT J1145.4+5858	$2.13^{+0.41}_{-0.35}$	[1.8]	23.8/17	0.43±0.03	0.573
SWIFT J1207.5+3355	$4.35^{+4.5}_{-3.2}$	$1.62^{+1.73}_{-1.35}$	1.2/2	0.17±0.02	0.21
SWIFT J1246.9+5433[4]	$32.1^{+4.5}_{-4.2}$	$1.48^{+0.12}_{-0.51}$	36.8/34	0.09 ± 0.01	0.047
SWIFT J1254.8−2655*	$0.13^{+0.28}_{-0.04}$, $[0.7]$	$1.78^{+0.20}_{-0.15}$	42.8/44	0.59 ± 0.03	0.728
SWIFT J1321.1+0858	$25.6^{+14.8}_{-8.7}$	[1.8]	4.4/3	0.27 ± 0.04	0.397
SWIFT J1416.8−1158*	$0.40^{+0.34}_{-0.31}$ $[0.5]$	$2.2^{+0.25}_{-0.24}$	60.2/50	0.57 ± 0.03	0.648
SWIFT J1439.2+1417	$2.44^{+0.91}_{-0.67}$	[1.8]	17.2/9	0.31 ± 0.03	0.326
SWIFT J1453.0+2553	–	1.72±0.05	73.8/87	1.06±0.07	0.822
SWIFT J1540.3+1415	–	$2.0^{+0.14}_{-0.13}$	18.4/18	0.15±0.01	0.246
SWIFT J1546.5+6931	$23.2^{+18.6}_{-9.7}$	[1.8]	1.2/1	0.09±0.02	0.333
SWIFT J1620.3+8101	$10.1^{+2.1}_{-1.6}$	[1.8]	9.6/13	0.54±0.03	0.794
SWIFT J2150.9+1402	$12.2^{+8.3}_{-4.9}$	[1.8]	0.4/1	0.19±0.03	0.253
SWIFT J2254.3+1146	$11.9^{+4.3}_{-2.9}$	[1.8]	6.8/6	0.13±0.03	0.107
SWIFT J2327.4+0939	–	1.2±0.1	11.1/18	0.40±0.03	0.211
SWIFT J2333.9−2343	–	1.67±0.04	97/104	0.79±0.03	0.898
SWIFT J2341.8+3034[5]	$56.5^{+15.5}_{-10.4}$	$2.02^{+0.16}_{-0.15}$	25.0/28	0.11±0.01	0.081
SWIFT J2344.8−4245*	$73.9^{+112.7}_{-42.1}$ $[0.8]$	$1.82^{+0.21}_{-0.28}$	78.6/50	0.77 ± 0.23	1.262

[a] In units of 10^{22} cm^{-2};

[b] The square brackets in the Γ column indicate that we used a fixed value due to the low statistic of the data

[c] In units of 10^{-11} erg cm^{-2} s^{-1};

[*] Best-fit model requires a partial covering model;

[+] Best-fit model requires two partial covering models. Reported in table the partial covering with higher N$_H$. The second partial covering has a N$_H$ of $14^{+2.3}_{-1.9}$ $[0.9]$;

[°] Best-fit model requires a partial covering model and a photoelectric absorption model with $N_H = 1.05^{+0.64}_{-0.66}$ cm^{-2};

[−] Best-fit model requires two partial covering models. Reported in table the partial covering with higher N$_H$. The second partial covering has a N$_H$ < 3.7 $[0.9]$;

[1] Best-fit model includes a bremsstrahlung component with a $kT = 0.20^{+0.11}_{-0.06}$ keV;

[2] Best-fit model includes a bremsstrahlung component with a $kT = 0.32^{+0.12}_{-0.08}$ keV:

[3] Best-fit model includes a bremsstrahlung component with a $kT = 0.52^{+0.24}_{-0.14}$ keV;

[4] Best-fit model includes a black body component with a $kT = 0.29^{+0.04}_{-0.04}$ keV and two zgauss models with $E = 6.38^{+0.03}_{-0.02}$ keV and $6.92^{+0.11}_{-0.3}$ keV with EW respectively of 597 ± 8 eV and 500 ± 23 eV;

[5] Best-fit model requires a second power law component, having the same photon index of the primary absorbed power law and passing only through the Galactic column density and a zgauss model with $E = 6.37 \pm 0.06$ and $EW < 625$ eV;

Table 6.3: *SWIFT*/XRT and *XMM-Newton* spectral analysis results of the averaged spectra belonging to *INTEGRAL*/IBIS catalogue. Frozen parameters are written in square brackets; errors are given at the 90 per cent confidence level.

Source	${N_{\rm H(intr)}}^a$	Γ^b	χ^2/ν	${F_{(2-10\ {\rm keV})}}^c$	$\frac{F_{(2-10\ {\rm keV})}}{F_{(20-100\ {\rm keV})}}$
IGR J00158+5605	–	2.30 ± 0.34	3.7/6	0.081 ± 0.008	0.121
IGR J00333+6122	$0.80^{+0.50}_{-0.44}$	$1.77^{+0.34}_{-0.32}$	12.5/22	0.67 ± 0.03	0.486
IGR J00465−4005^d	$28.1^{+10.7}_{-9.1}$	$2.50^{+0.35}_{-0.44}$	3.5/9	0.13 ± 0.02	0.037
IGR J01545+6437	–	[1.8]	3.8/3	0.010 ± 0.003	0.012
IGR J02086−1742	–	1.54 ± 0.09	42.2/36	0.59 ± 0.03	0.215
SWIFT J0216.3+5128	$1.26^{+0.16}_{-0.14}$	1.89 ± 0.12	110.1/118	1.24 ± 0.02	0.765
IGR J02524−0829	$12.1^{+3.5}_{-2.9}$	$2.29^{+0.73}_{-0.69}$	26.4/26	0.54 ± 0.25	0.137
SWIFT J0255.2−0011	$37.9^{+7.1}_{-3.5}$	[1.8]	32.6/9	0.82±0.06	0.134
IGR J03344+1506	–	[1.8]	2.6/4	0.013 ± 0.032	0.005
SWIFT J0505.7−2348^d	$5.2^{+1.1}_{-1.0}$	$1.36^{+0.24}_{-0.15}$	66.3/54	1.76 ± 0.05	0.321
SWIFT J0519.5−3140^d	$5.6^{+3.5}_{-2.0}$	1.99 ± 0.12	161.7/128	1.29 ± 0.03	0.297
SWIFT J0605.8−2754	$0.13^{+0.07}_{-0.06}$	$1.84^{+0.18}_{-0.17}$	44.2/52	0.79 ± 0.05	0.416
SWIFT J0640.4−2554	0.20 ± 0.02	1.76 ± 0.06	216.3/224	2.06 ± 0.03	0.538
SWIFT J0855.6+6425^d	$19.6^{+4.5}_{-3.9}$	[1.8]	5.9/8	0.28±0.02	0.11
IGR J09253+6929	$14.8^{+28.0}_{-11.0}$	[1.8]	0.22/2	0.045 ± 0.013	0.023
IGR J10147−6354	$1.73^{+0.93}_{-0.57}$	[1.8]	17.9/27	0.13 ± 0.01	0.121
IGR J10470+2554	$12.4^{+4.6}_{-3.8}$	$3.16^{+1.23}_{-1.07}$	8.2/12	0.22 ± 0.01	0.069
IGR J11456−6956	–	1.74 ± 0.10	71.8/53	0.54 ± 0.02	0.397
IGR J12107+3822$^+$	$4.63^{+1.16}_{-0.99}$	$1.20^{+0.08}_{-0.09}$	77.3/69	0.34±0.01	0.223
IGR J12415−5750	–	1.63 ± 0.08	68.3/76	0.77 ± 0.02	0.377
IGR J12479−5829	$2.28^{+0.74}_{-0.57}$	[1.8]	9.4/14	0.029 ± 0.002	0.028
IGR J13168−7157	–	1.59 ± 0.10	25.5/42	0.38±0.02	0.319
IGR J13415+3033	$29.70^{+3.51}_{-2.01}$	$1.97^{+0.16}_{-0.18}$	426/397	0.25 ± 0.01	0.135
IGR J13466+1921	–	1.73±0.07	61.1/62	0.32±0.02	0.158
IGR J14301−4158	$1.36^{+0.76}_{-0.46}$	$1.83^{+0.76}_{-0.46}$	5.5/11	0.27 ± 0.02	0.3
SWIFT J1513.8−8125*	$0.76^{+0.24}_{-0.35}$ [0.6]	$1.35^{+0.26}_{-0.21}$	65/50	1.11±0.04	0.698
IGR J15311−3737	–	1.73 ± 0.16	8.4/11	0.19 ± 0.01	0.213

Table 6.4: – *continued*

Source	$N_{\mathrm{H(intr)}}{}^{a}$	Γ^{b}	χ^2/ν	$F_{(2-10\ \mathrm{keV})}{}^{c}$	$\frac{F_{(2-10\ \mathrm{keV})}}{F_{(20-100\ \mathrm{keV})}}$
IGR J16351−5806⁻	370^{+480}_{-170} $[0.9]$	$1.78^{+0.08}_{-0.07}$	88.7/85	0.050 ± 0.004	0.026
IGR J16426+6536	–	[1.8]	3.5/5	0.0085 ± 0.0021	0.002
IGR J17009+3559	$23.7^{+16.0}_{-12.0}$	[1.8]	2.2/4	0.108 ± 0.022	0.061
IGR J18078+1123*	$0.65^{+0.46}_{-0.39}$ $[0.5]$	$1.68^{+0.20}_{-0.19}$	52.6/67	0.65±0.03	0.177
IGR J18249−3243	–	1.55 ± 0.12	30.3/23	0.47 ± 0.02	0.461
IIGR J18311−3337	$1.40^{+5.03}_{-1.10}$	[1.8]	3.2/6	0.026 ± 0.008	0.015
IGR J19077−3925	$0.14^{+0.10}_{-0.08}$	$1.78^{+0.24}_{-0.22}$	11.4/18	0.36 ± 0.02	0.24
IGR J19118−1707	$10.4^{+8.10}_{-5.00}$	[1.8]	2.2/4	0.14 ± 0.03	0.2
SWIFT J2118.9+3336	$0.47^{+0.12}_{-0.47}$	$1.60^{+0.22}_{-0.21}$	29.3/29	0.68±0.04	0.439
IGR J21398+5950	0.21 ± 0.05	1.68 ± 0.05	278.8/260	0.50±0.01	0.490
IGR J22292+6647	$0.27^{+0.11}_{-0.09}$	$1.84^{+0.17}_{-0.16}$	56.5/71	0.55 ± 0.01	0.495
IGR J23524+5842[d]	$11.2^{+9.2}_{-5.5}$	[1.8]	15.5/10	0.12 ± 0.02	0.098

[a] Where not specified in units of 10^{22} cm^{-2};

[b] The square brackets in the Γ column indicate that we used a fixed value due to the low statistic of the data

[c] In units of 10^{-11} erg cm^{-2} s^{-1};

[d] Best-fit model requires a second power law component, having the same photon index of the primary absorbed power law, and passing only through the Galactic column density.

[*] Best-fit model requires a partial covering model;

[+] Best-fit model requires a second power law component, having a photon index of $\Gamma = 1.81^{+0.27}_{-0.22}$

[−] Best-fit model requires a mekal model with $kT = 0.62 \pm 0.05$ keV, two partial covering models with the second and lower N$_H = 5.8 \pm 2.2 \times 10^{23}$ cm^{-2} and a zgauss model with $E = 6.39 \pm 0.02$ keV and EW of 136^{+50}_{-38} eV

Chapter 7

Appendix A

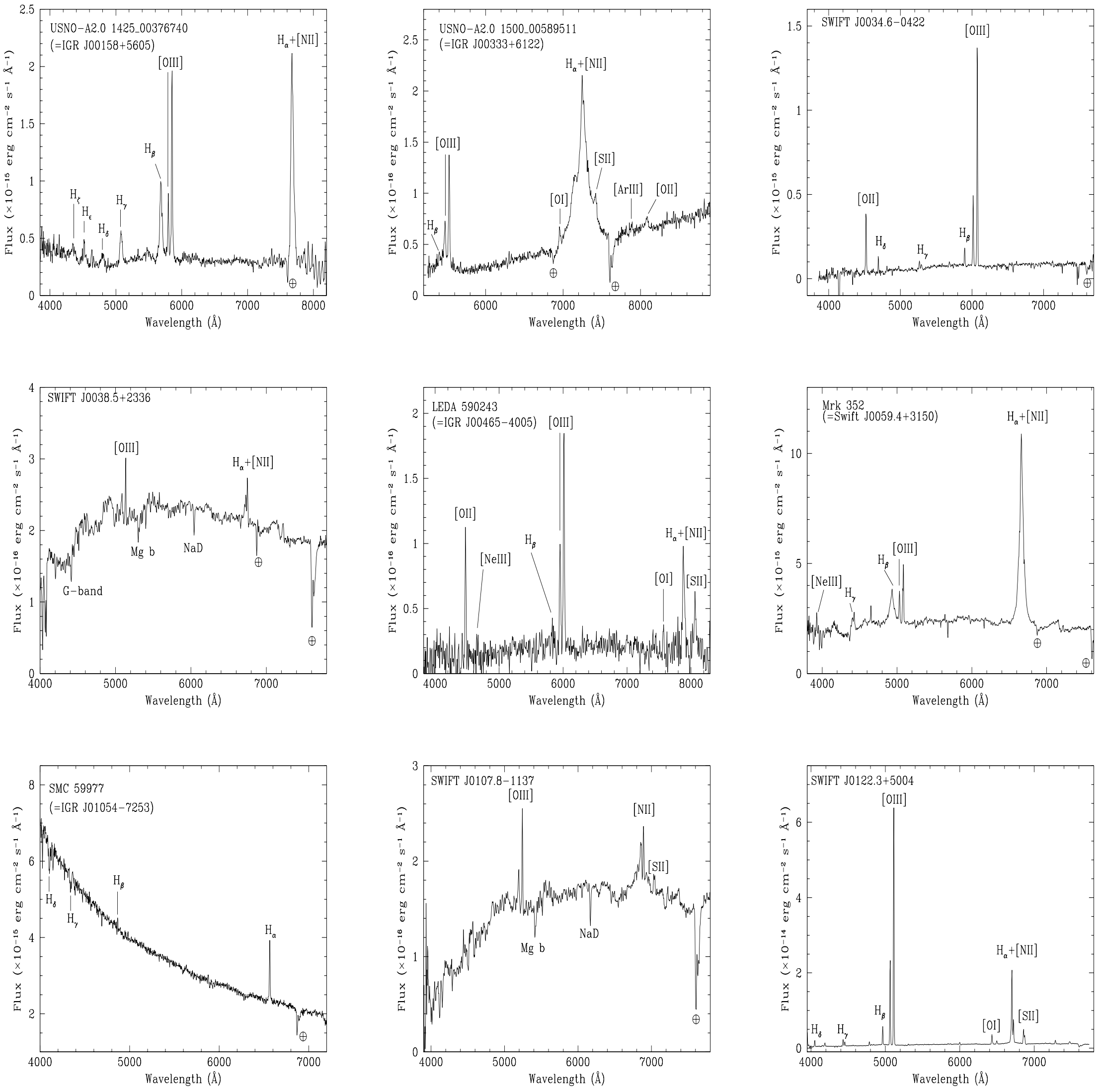
USNO-A2.0 1425_00376740
(=IGR J00158+5605)
USNO-A2.0 1500_00589511
(=IGR J00333+6122)
SWIFT J0034.6-0422
SWIFT J0038.5+2336
LEDA 590243
(=IGR J00465-4005)
Mrk 352
(=Swift J0059.4+3150)
SMC 59977
(=IGR J01054-7253)
SWIFT J0107.8-1137
SWIFT J0122.3+5004
H_α+[NII]
H_β
H_γ
H_δ
H_ϵ
H_ζ
H_α
[OIII]
[OII]
[OI]
[SII]
[NII]
[ArIII]
[NeIII]
G-band
Mg b
NaD
⊕
Flux ($\times 10^{-15}$ erg cm^{-2} s^{-1} Å^{-1})
Flux ($\times 10^{-16}$ erg cm^{-2} s^{-1} Å^{-1})
Flux ($\times 10^{-14}$ erg cm^{-2} s^{-1} Å^{-1})
Wavelength (Å)

Figure 7.1

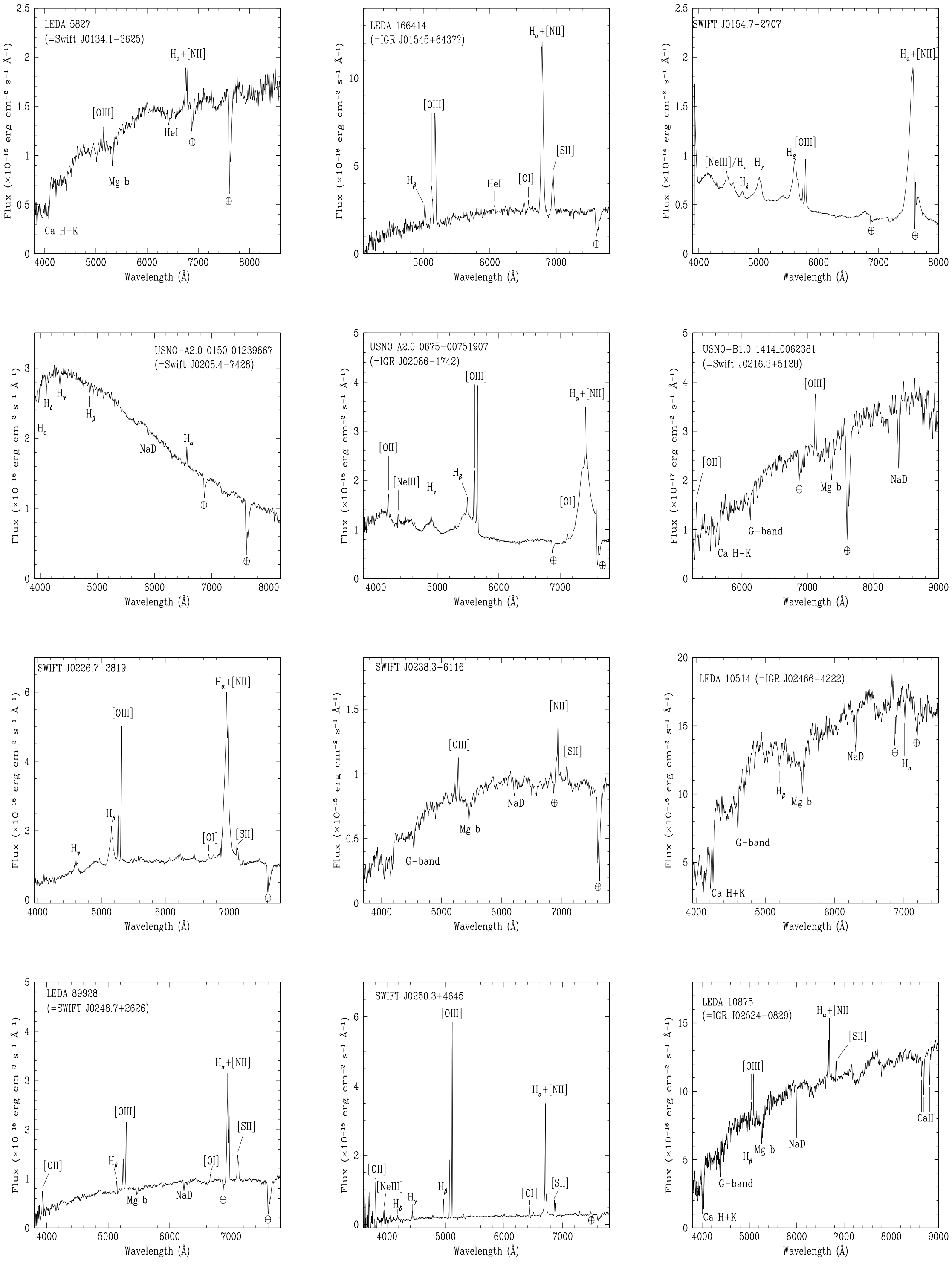
LEDA 5827
(=Swift J0134.1-3625)
LEDA 166414
(=IGR J01545+6437?)
SWIFT J0154.7-2707
USNO-A2.0 0150_01239667
(=Swift J0208.4-7428)
USNO A2.0 0675-00751907
(=IGR J02086-1742)
USNO-B1.0 1414_0062381
(=Swift J0216.3+5128)
SWIFT J0226.7-2819
SWIFT J0238.3-6116
LEDA 10514 (=IGR J02466-4222)
LEDA 89928
(=SWIFT J0248.7+2626)
SWIFT J0250.3+4645
LEDA 10875
(=IGR J02524-0829)
Hα+[NII]
[OIII]
[OII]
[NeIII]
[NeIII]/Hε
[OI]
[SII]
[NII]
Hβ
Hγ
Hδ
Hε
Hα
HeI
Mg b
NaD
G-band
Ca H+K
CaII
⊕
Flux (×10⁻¹⁵ erg cm⁻² s⁻¹ Å⁻¹)
Flux (×10⁻¹⁶ erg cm⁻² s⁻¹ Å⁻¹)
Flux (×10⁻¹⁴ erg cm⁻² s⁻¹ Å⁻¹)
Flux (×10⁻¹⁷ erg cm⁻² s⁻¹ Å⁻¹)
Wavelength (Å)

Figure 7.2

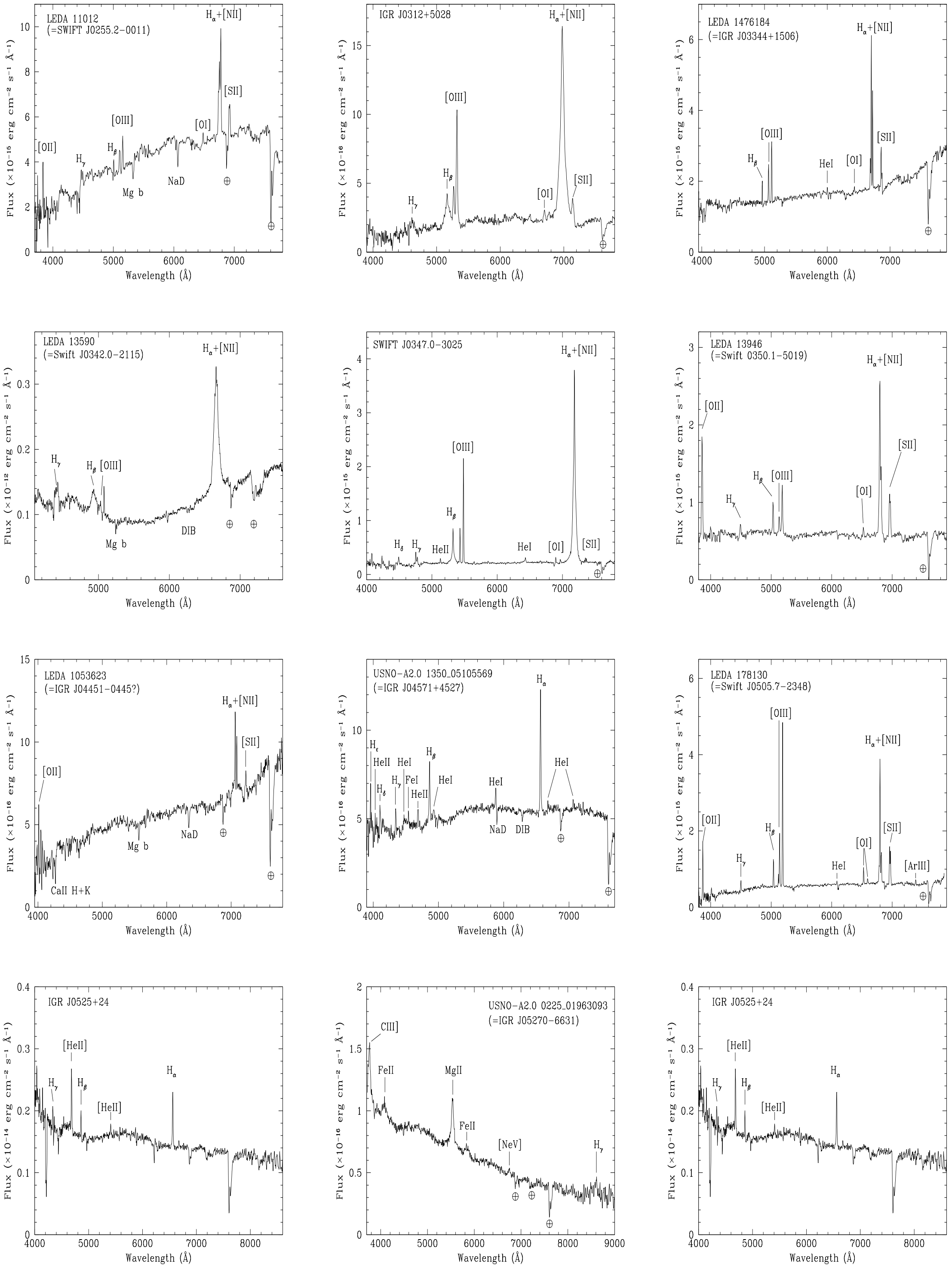
LEDA 11012
(=SWIFT J0255.2-0011)
H_α+[NII]
[SII]
[OI]
[OIII]
H_β
H_γ
[OII]
NaD
Mg b
IGR J0312+5028
[OIII]
H_β
H_γ
[OI]
[SII]
LEDA 1476184
(=IGR J03344+1506)
HeI
LEDA 13590
(=Swift J0342.0-2115)
DIB
SWIFT J0347.0-3025
H_δ
HeII
LEDA 13946
(=Swift 0350.1-5019)
LEDA 1053623
(=IGR J04451-0445?)
CaII H+K
USNO-A2.0 1350_05105569
(=IGR J04571+4527)
H_α
H_ϵ
FeI
LEDA 178130
(=Swift J0505.7-2348)
[ArIII]
IGR J0525+24
[HeII]
USNO-A2.0 0225_01963093
(=IGR J05270-6631)
CIII]
FeII
MgII
[NeV]
Flux (×10⁻¹⁵ erg cm⁻² s⁻¹ Å⁻¹)
Flux (×10⁻¹⁶ erg cm⁻² s⁻¹ Å⁻¹)
Flux (×10⁻¹² erg cm⁻² s⁻¹ Å⁻¹)
Flux (×10⁻¹⁴ erg cm⁻² s⁻¹ Å⁻¹)
Wavelength (Å)

Figure 7.3

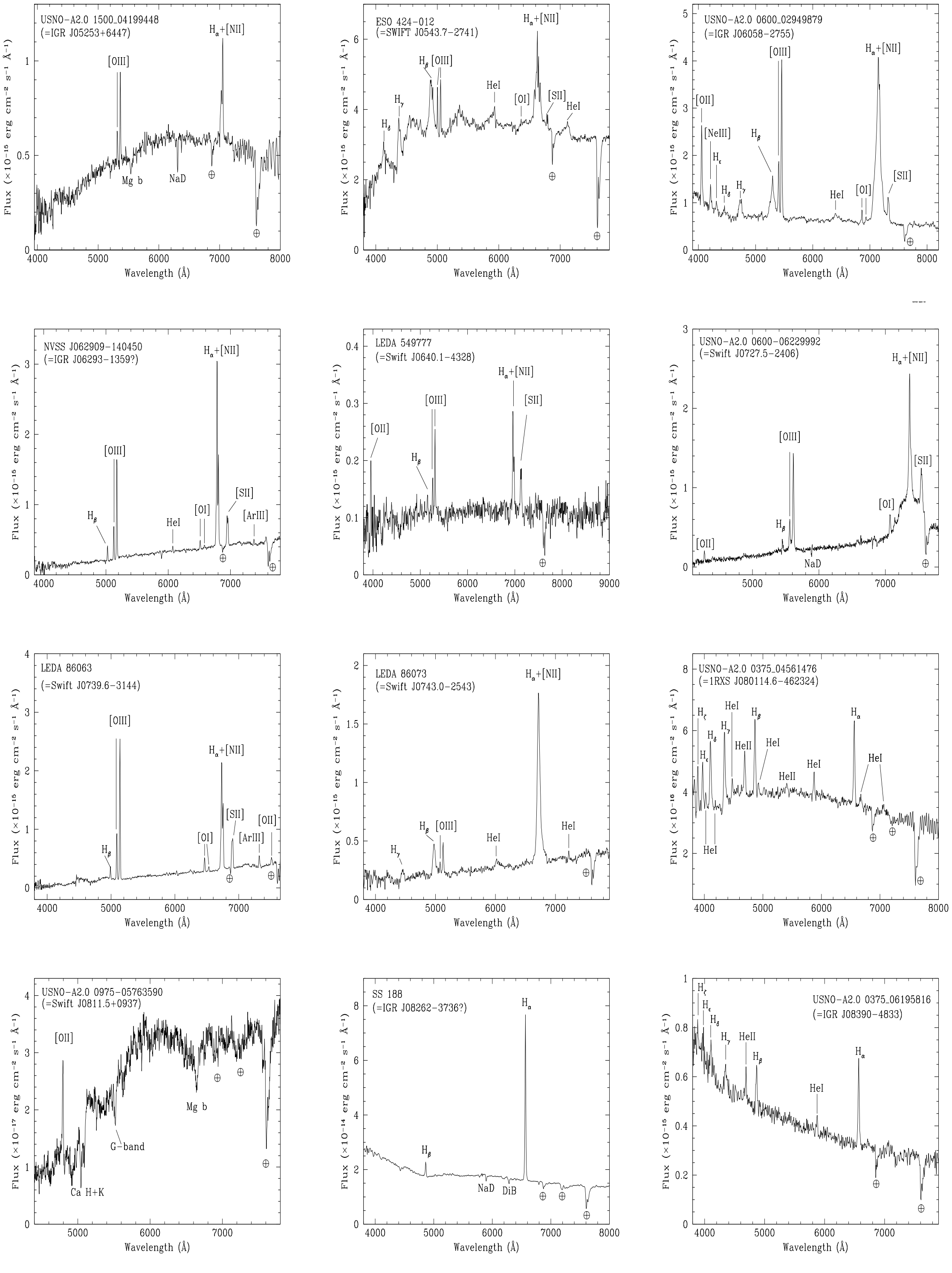
USNO-A2.0 1500_04199448
(=IGR J05253+6447)
[OIII]
H_α+[NII]
Mg b
NaD
⊕
ESO 424-012
(=SWIFT J0543.7-2741)
H_α+[NII]
H_β [OIII]
H_γ
H_δ
HeI
[OI]
[SII]
USNO-A2.0 0600_02949879
(=IGR J06058-2755)
[OII]
[NeIII]
H_ϵ
H_δ
H_γ
[OIII]
[OI]
[SII]
NVSS J062909-140450
(=IGR J06293-1359?)
[ArIII]
LEDA 549777
(=Swift J0640.1-4328)
USNO-A2.0 0600-06229992
(=Swift J0727.5-2406)
LEDA 86063
(=Swift J0739.6-3144)
LEDA 86073
(=Swift J0743.0-2543)
USNO-A2.0 0375_04561476
(=1RXS J080114.6-462324)
H_ζ
H_α
HeII
USNO-A2.0 0975-05763590
(=Swift J0811.5+0937)
G-band
Ca H+K
SS 188
(=IGR J08262-3736?)
DiB
USNO-A2.0 0375_06195816
(=IGR J08390-4833)
Flux ($\times10^{-15}$ erg cm^{-2} s^{-1} Å^{-1})
Flux ($\times10^{-16}$ erg cm^{-2} s^{-1} Å^{-1})
Flux ($\times10^{-17}$ erg cm^{-2} s^{-1} Å^{-1})
Flux ($\times10^{-14}$ erg cm^{-2} s^{-1} Å^{-1})
Wavelength (Å)
4000
5000
6000
7000
8000
9000

Figure 7.4

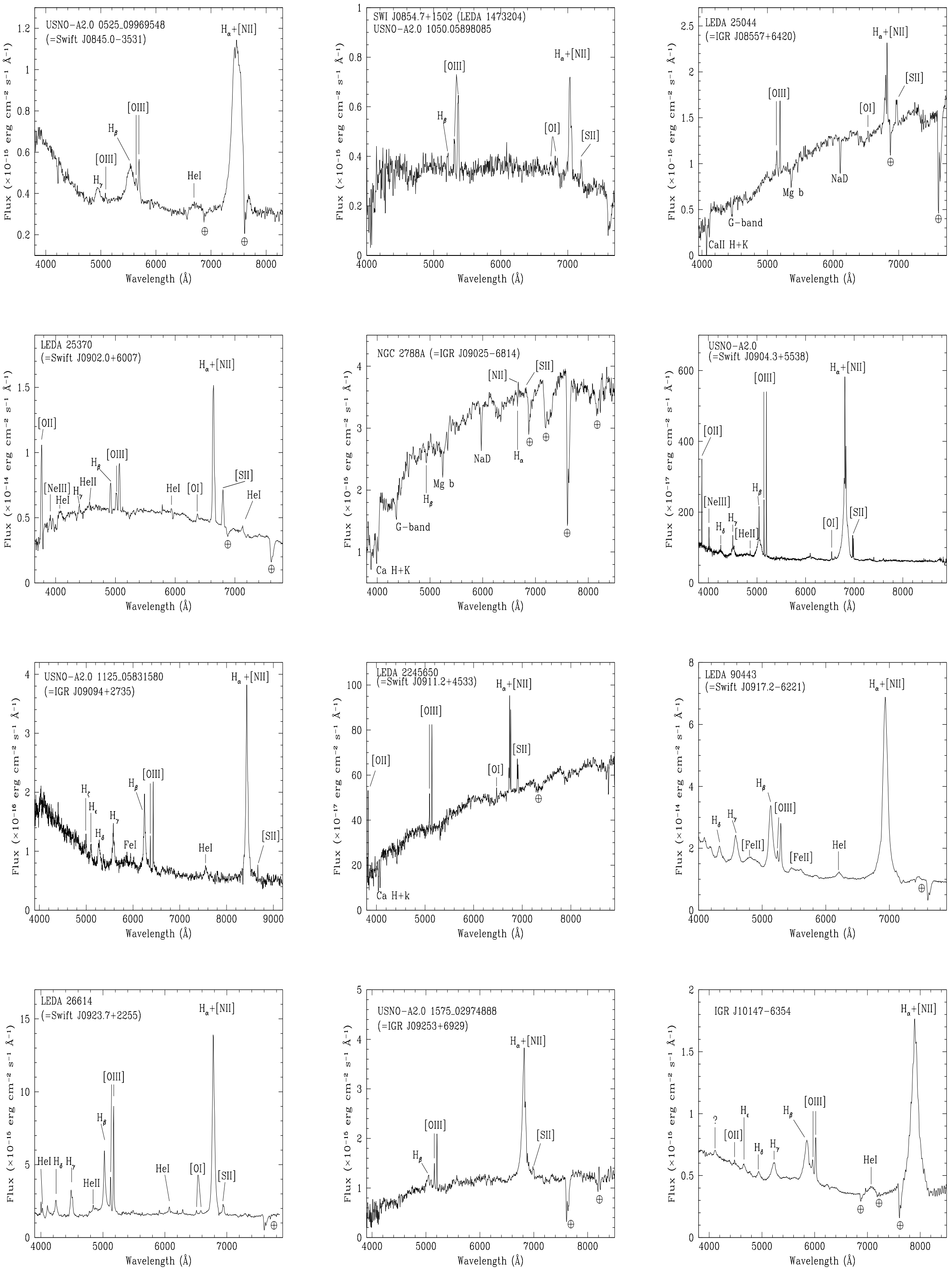USNO-A2.0 0525_09969548
(=Swift J0845.0-3531)
Hα+[NII]
[OIII]
Hβ
[OIII]
Hγ
HeI
⊕
Flux ($\times10^{-15}$ erg cm^{-2} s^{-1} Å^{-1})
Wavelength (Å)
SWI J0854.7+1502 (LEDA 1473204)
USNO-A2.0 1050.05898085
[OIII]
Hβ
Hα+[NII]
[OI]
[SII]
LEDA 25044
(=IGR J08557+6420)
Hα+[NII]
[SII]
[OIII]
[OI]
Mg b
NaD
G-band
CaII H+K
LEDA 25370
(=Swift J0902.0+6007)
Hα+[NII]
[OII]
[OIII]
Hβ
HeII
[NeIII]
HeI
Hγ
HeI
[OI]
[SII]
HeI
Flux ($\times10^{-14}$ erg cm^{-2} s^{-1} Å^{-1})
NGC 2788A (=IGR J09025-6814)
[NII]
[SII]
NaD
Hα
Mg b
Hβ
G-band
Ca H+K
USNO-A2.0
(=Swift J0904.3+5538)
Hα+[NII]
[OIII]
[OII]
[NeIII]
Hδ
Hγ
[HeII]
Hβ
[OI]
[SII]
Flux ($\times10^{-17}$ erg cm^{-2} s^{-1} Å^{-1})
USNO-A2.0 1125_05831580
(=IGR J09094+2735)
Hα+[NII]
[OIII]
Hβ
Hζ
Hε
Hδ
Hγ
FeI
HeI
[SII]
Flux ($\times10^{-16}$ erg cm^{-2} s^{-1} Å^{-1})
LEDA 2245650
(=Swift J0911.2+4533)
Hα+[NII]
[OIII]
[OII]
[OI]
[SII]
Ca H+k
LEDA 90443
(=Swift J0917.2-6221)
Hα+[NII]
Hβ
[OIII]
Hδ
Hγ
[FeII]
[FeII]
HeI
LEDA 26614
(=Swift J0923.7+2255)
Hα+[NII]
[OIII]
Hβ
HeI
Hδ
Hγ
HeII
HeI
[OI]
[SII]
USNO-A2.0 1575_02974888
(=IGR J09253+6929)
Hα+[NII]
[OIII]
Hβ
[SII]
IGR J10147-6354
Hα+[NII]
?
[OII]
Hε
Hδ
Hγ
Hβ
[OIII]
HeI

Figure 7.5

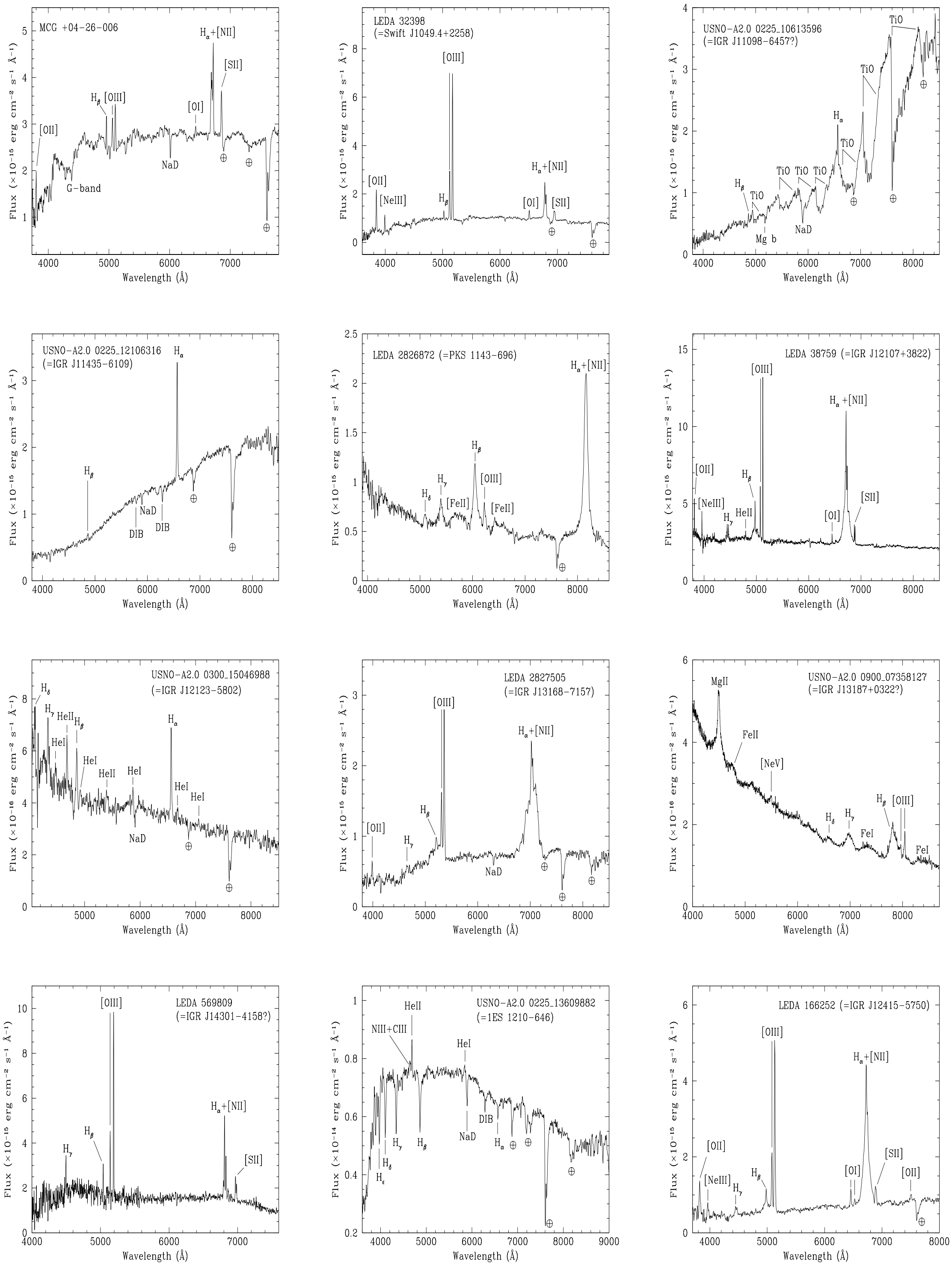
MCG +04-26-006
LEDA 32398 (=Swift J1049.4+2258)
USNO-A2.0 0225_10613596 (=IGR J11098-6457?)
USNO-A2.0 0225_12106316 (=IGR J11435-6109)
LEDA 2826872 (=PKS 1143-696)
LEDA 38759 (=IGR J12107+3822)
USNO-A2.0 0300_15046988 (=IGR J12123-5802)
LEDA 2827505 (=IGR J13168-7157)
USNO-A2.0 0900_07358127 (=IGR J13187+0322?)
LEDA 569809 (=IGR J14301-4158?)
USNO-A2.0 0225_13609882 (=1ES 1210-646)
LEDA 166252 (=IGR J12415-5750)
[OII]
[NeIII]
H_ε
H_δ
H_γ
H_β
H_α
H_α+[NII]
[OIII]
[OI]
[SII]
[FeII]
FeII
FeI
MgII
[NeV]
HeI
HeII
NIII+CIII
G-band
Mg b
NaD
DIB
TiO
⊕
Flux (×10⁻¹⁵ erg cm⁻² s⁻¹ Å⁻¹)
Flux (×10⁻¹⁶ erg cm⁻² s⁻¹ Å⁻¹)
Flux (×10⁻¹⁴ erg cm⁻² s⁻¹ Å⁻¹)
Wavelength (Å)

Figure 7.6

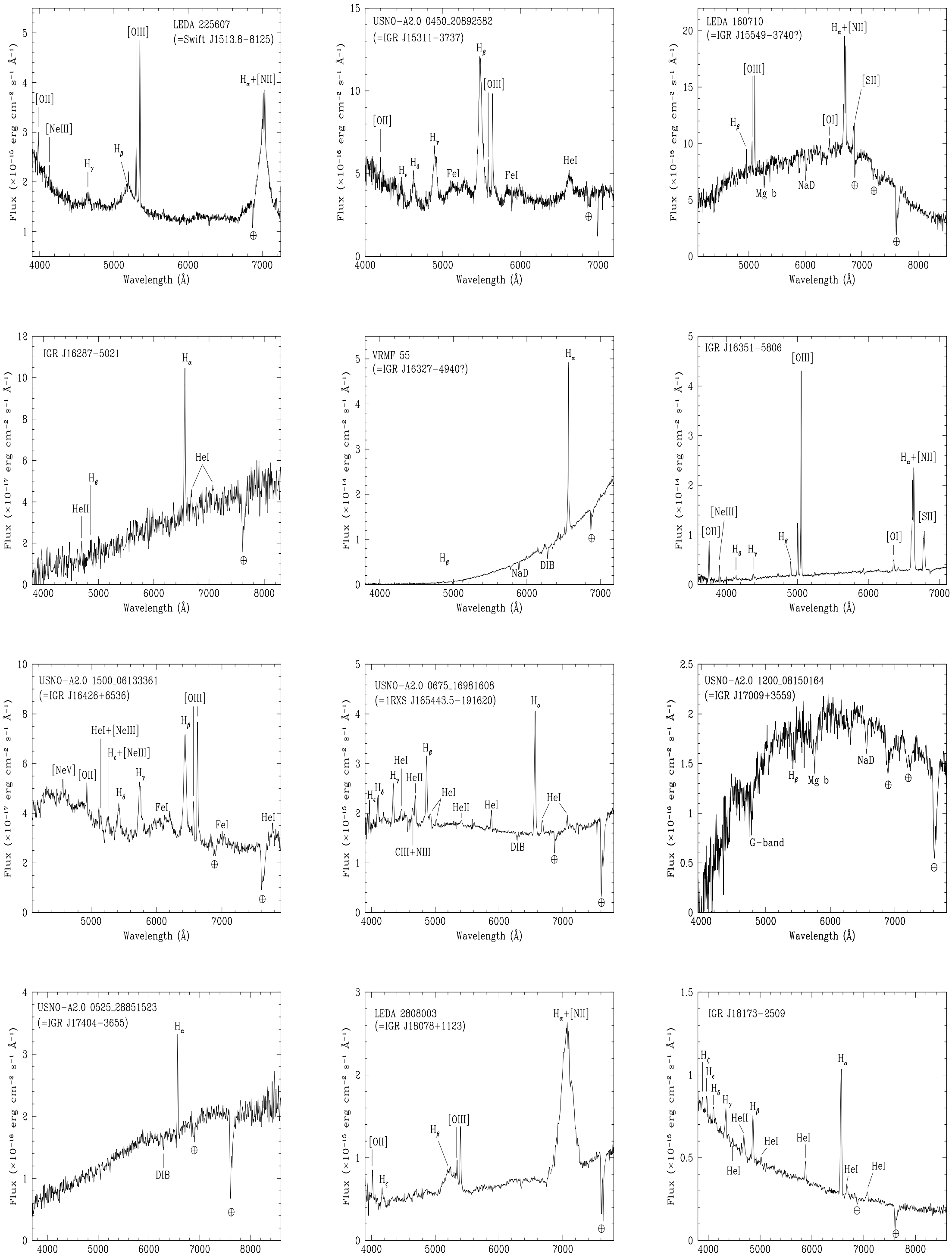
LEDA 225607
(=Swift J1513.8-8125)
[OII]
[NeIII]
H_γ
H_β
[OIII]
H_α+[NII]
Flux (×10⁻¹⁵ erg cm⁻² s⁻¹ Å⁻¹)
Wavelength (Å)
USNO-A2.0 0450_20892582
(=IGR J15311-3737)
[OII]
H_ϵ
H_δ
H_γ
FeI
H_β
[OIII]
FeI
HeI
Flux (×10⁻¹⁶ erg cm⁻² s⁻¹ Å⁻¹)
Wavelength (Å)
LEDA 160710
(=IGR J15549-3740?)
H_β
[OIII]
Mg b
NaD
[OI]
H_α+[NII]
[SII]
Flux (×10⁻¹⁵ erg cm⁻² s⁻¹ Å⁻¹)
Wavelength (Å)
IGR J16287-5021
HeII
H_β
H_α
HeI
Flux (×10⁻¹⁷ erg cm⁻² s⁻¹ Å⁻¹)
Wavelength (Å)
VRMF 55
(=IGR J16327-4940?)
H_β
NaD
DIB
H_α
Flux (×10⁻¹⁴ erg cm⁻² s⁻¹ Å⁻¹)
Wavelength (Å)
IGR J16351-5806
[OII]
[NeIII]
H_δ
H_γ
H_β
[OIII]
[OI]
H_α+[NII]
[SII]
Flux (×10⁻¹⁴ erg cm⁻² s⁻¹ Å⁻¹)
Wavelength (Å)
USNO-A2.0 1500_06133361
(=IGR J16426+6536)
[NeV]
[OII]
HeI+[NeIII]
H_ϵ+[NeIII]
H_δ
H_γ
FeI
H_β
[OIII]
FeI
HeI
Flux (×10⁻¹⁷ erg cm⁻² s⁻¹ Å⁻¹)
Wavelength (Å)
USNO-A2.0 0675_16981608
(=1RXS J165443.5-191620)
H_ϵ
H_δ
H_γ
HeI
HeII
CIII+NIII
H_β
HeI
HeII
HeI
DIB
H_α
HeI
Flux (×10⁻¹⁵ erg cm⁻² s⁻¹ Å⁻¹)
Wavelength (Å)
USNO-A2.0 1200_08150164
(=IGR J17009+3559)
G-band
H_β
Mg b
NaD
Flux (×10⁻¹⁶ erg cm⁻² s⁻¹ Å⁻¹)
Wavelength (Å)
USNO-A2.0 0525_28851523
(=IGR J17404-3655)
DIB
H_α
Flux (×10⁻¹⁶ erg cm⁻² s⁻¹ Å⁻¹)
Wavelength (Å)
LEDA 2808003
(=IGR J18078+1123)
[OII]
H_ζ
H_β
[OIII]
H_α+[NII]
Flux (×10⁻¹⁵ erg cm⁻² s⁻¹ Å⁻¹)
Wavelength (Å)
IGR J18173-2509
H_ζ
H_ϵ
H_δ
H_γ
HeII
HeI
H_β
HeI
HeI
H_α
HeI
HeI
Flux (×10⁻¹⁵ erg cm⁻² s⁻¹ Å⁻¹)
Wavelength (Å)

Figure 7.7

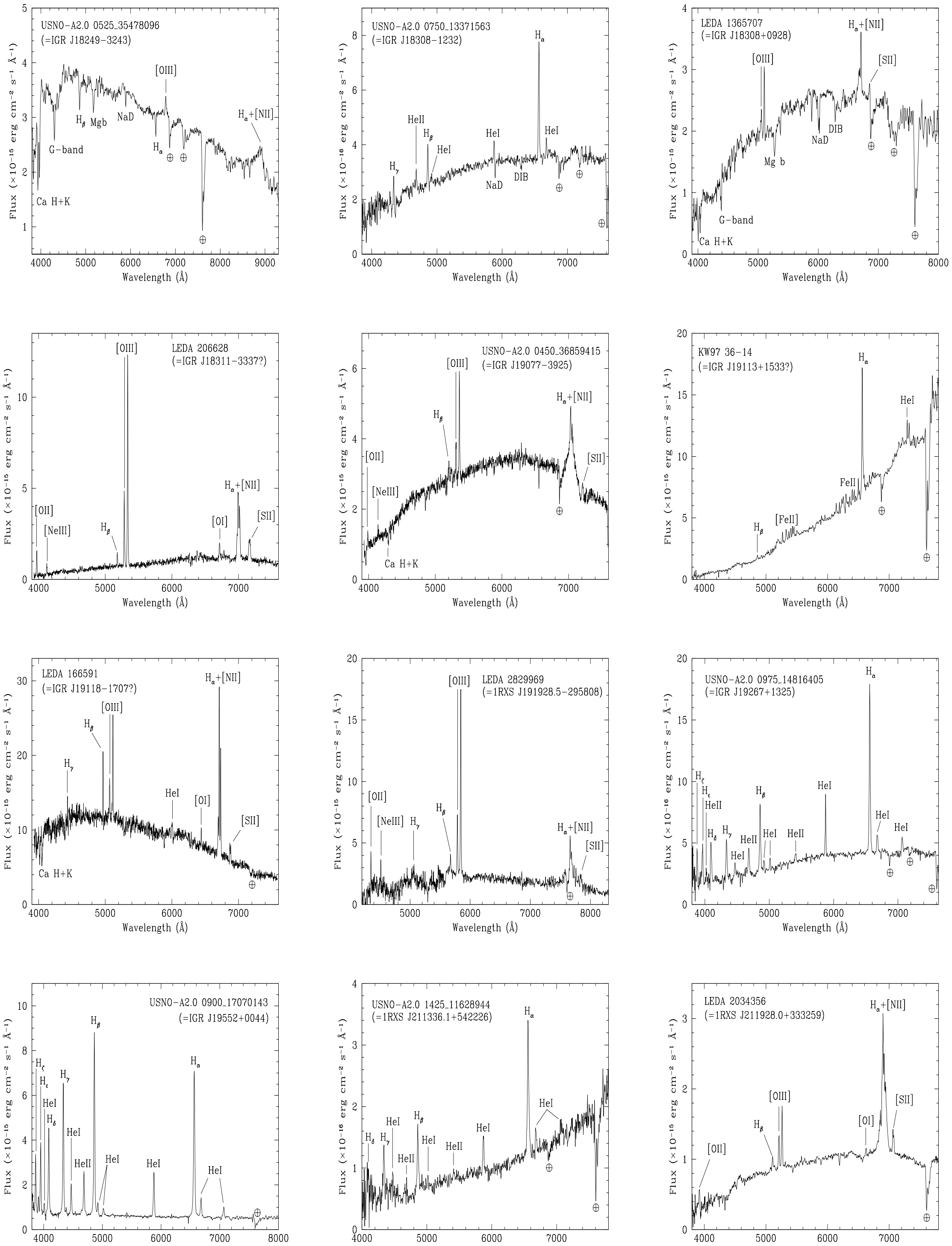
USNO-A2.0 0525_35478096
(=IGR J18249-3243)
USNO-A2.0 0750_13371563
(=IGR J18308-1232)
LEDA 1365707
(=IGR J18308+0928)
LEDA 206628
(=IGR J18311-3337?)
USNO-A2.0 0450_36859415
(=IGR J19077-3925)
KW97 36-14
(=IGR J19113+1533?)
LEDA 166591
(=IGR J19118-1707?)
LEDA 2829969
(=1RXS J191928.5-295808)
USNO-A2.0 0975_14816405
(=IGR J19267+1325)
USNO-A2.0 0900_17070143
(=IGR J19552+0044)
USNO-A2.0 1425_11628944
(=1RXS J211336.1+542226)
LEDA 2034356
(=1RXS J211928.0+333259)
Ca H+K
G-band
Mgb
NaD
DIB
[OIII]
[OII]
[NeIII]
[OI]
[SII]
[FeII]
FeII
HeI
HeII
Hα
Hβ
Hγ
Hδ
Hε
Hζ
Hα+[NII]
⊕
Flux (×10⁻¹⁵ erg cm⁻² s⁻¹ Å⁻¹)
Flux (×10⁻¹⁶ erg cm⁻² s⁻¹ Å⁻¹)
Wavelength (Å)

Figure 7.8

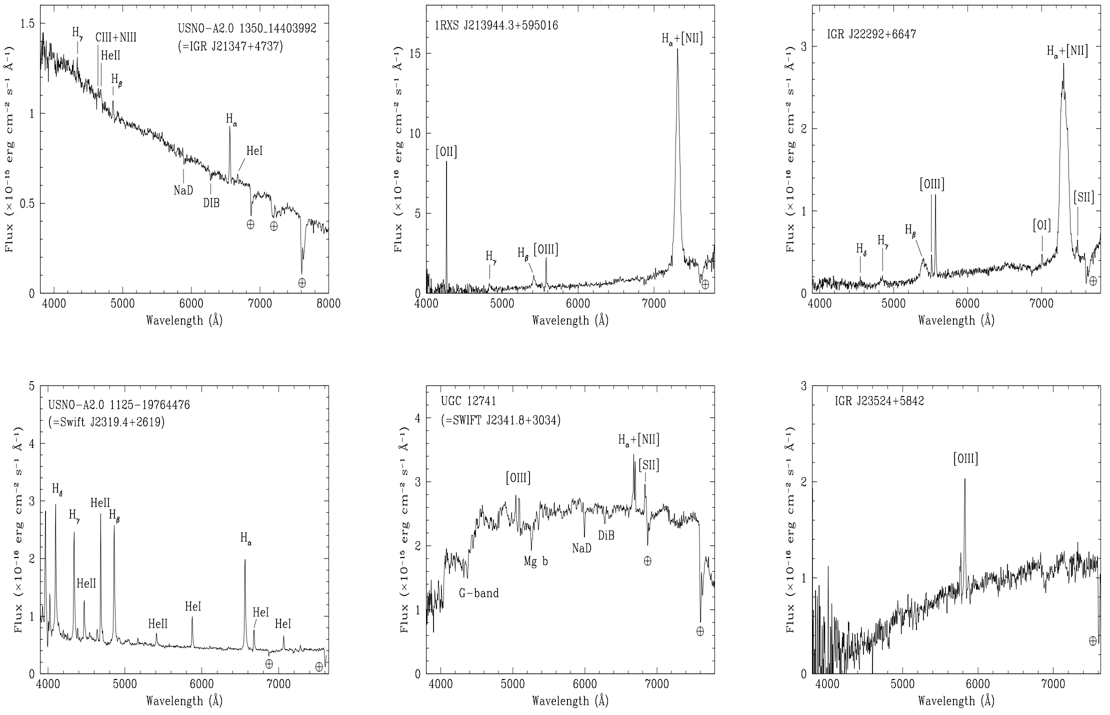
USNO-A2.0 1350_14403992
(=IGR J21347+4737)
H_γ
CIII+NIII
HeII
H_β
H_α
HeI
NaD
DIB
⊕
1RXS J213944.3+595016
H_α+[NII]
[OII]
H_γ
H_β
[OIII]
IGR J22292+6647
H_α+[NII]
[OIII]
[SII]
[OI]
H_δ
H_γ
H_β
USNO-A2.0 1125-19764476
(=Swift J2319.4+2619)
H_δ
H_γ
HeII
H_β
HeII
H_α
HeII
HeI
HeI
HeI
UGC 12741
(=SWIFT J2341.8+3034)
H_α+[NII]
[SII]
[OIII]
Mg b
NaD
DiB
G-band
IGR J23524+5842
[OIII]
Flux ($\times 10^{-15}$ erg cm^{-2} s^{-1} Å^{-1})
Flux ($\times 10^{-16}$ erg cm^{-2} s^{-1} Å^{-1})
Wavelength (Å)

Figure 7.9

Chapter 8

Appendix B1

On the identification of the *Fermi*/LAT source 0FGL J2001.0+4352 with a BL Lac

Abstract

We report on the identification of the gamma-ray source 0FGL J20001.0+4352 listed in the *Fermi* bright source catalogue. This object, which has an observed 1–100 GeV flux of (7.8±1.2)$\times 10^{-9}$ ph cm^{-2} s^{-1} and is located close to the Galactic plane, is not associated with any previously known high energy source. We use archival *XMM-Newton* and *Swift*/XRT data to localise with arcsec accuracy the X-ray counterpart of this GeV emitter and to characterise its X-ray properties: the source is bright (the 0.2–12 keV flux is 1.9×10^{-12} erg cm^{-2} s^{-1}), variable (by a factor of $\sim$2) and with a steep power law spectrum ($\Gamma = 2.7$). It coincides with a radio bright ($\sim$200 mJy at 8.4 GHz) and flat spectrum object (MG4 J200112+4352 in NED). Broad-band optical photometry of this source suggests variability also in this waveband, while a spectroscopic follow-up observation provides the first source classification as a BL Lac object. The source SED, as well as the overall characteristics and optical classification, point to a high frequency

peaked blazar identification for 0FGL J2001.0+4352.

Reference: Bassani, L., Landi, R., Masetti, N., Parisi, P., et al. 2009, MNRAS, 397, 55

Chapter 9

Appendix B2

Optical/IR counterpart to the resolved X-ray jet source CXO J172337.5-373442 and its distance

Abstract

We present results of observations in the optical to mid-infrared wavelengths of the X-ray source CXO J172337.5-373442, which was serendipitously discovered in the *Chandra* images and was found to have a fully resolved X-ray jet. The observations include a combination of photometry and spectroscopy in the optical using ground-based telescopes and mid-infrared photometry using *Spitzer*. We detect the optical/IR counterpart of CXO J172337.5-373442 and identify it to be a G9-V star located at a distance of 334±60 pc. Comparable values of the hydrogen column densities determined independently from the optical/IR observations and X-ray observations indicate that the optical source is associated with the X-ray source. Since the X-ray luminosity can not be explained in terms of emission from a single G9-V star, it is likely that CXO J172337.5-373442 is an accreting compact object in a binary system. Thus, CXO J172337.5-373442 is the nearest known resolved X-ray jet from a binary system, which is not a symbiotic star. Based

on the existing X-ray data, the nature of the compact object can not be confirmed. However the low luminosity of the X-ray point source, $7.1\times10^{30}\,L_\odot$, combined with estimates of the age of the jet and a lack of detection of bright outburst, suggests that the X-ray jet was launched during extreme quiescence of the object. The measured low X-ray luminosity of the jet suggests the likelihood of such jets being more ubiquitous than our current understanding.

Reference: Mookerjea, B., Parisi, P., Bhattacharyya, S., et al. 2010, MNRAS, 409, 114

Bibliography

[1] Akiyama, M., Ueda, Y., Ohta, K., et al. 2003, ApJS, 148, 275

[] Antonucci, R. R. J., Miller, J. S. et al. 1985, ApJ, 297, 621

[] Antonucci, R., 1993, ARA&A, 31, 473

[] Aretxaga, I., Joguet, B., Kunth, D., et al. 1999, ApJ, 519, 123

[] Barger, A.J., Cowie, L.L., Brandt, W.N., et al. 2002, 124, 1839

[] Barthelmy, S.D. 2004, Proceedings of the SPIE, 5165, 175

[] Bassani, L., Dadina, M., Maiolino, R., et al. 1999, ApJS, 121, 473

[] Bianchi, S., Corral, A., Panessa, F., et al. 2008, MNRAS, 385, 195

[] Bird, A. J., Barlow, E. J., Bassani, L., et al. 2004, ApJ, 607, 33

[] Bird, A. J., Barlow, E. J., Bassani, L., et al. 2006, ApJ, 636, 765

[] Bird, A. J., Malizia, A., Bazzano, A., et al. 2007, ApJS, 170, 175

[] Bird, A.J., Bazzano, A., Bassani, L., et al. 2010, ApJS, 186, 1

[] Bongiorno, A., Mingnoli, M., Zamorani, G., et al. 2010, A&A, 510, 56

[] Bottorff, M., Korista, K., Shlosman, I., et al. 1997, ApJ, 479, 200

[] Branduardi-Raymont G., Sako M., Kahn S.M. et al. 2001, A&A, 365, 162

[] Burlon, D., Ajello, M., Greiner, J., et al. 2011, [arXiv:1012.0302]

[] Burrows, D.N., Hill, J.E., Nousek, J.A., et al. 2004, Proc. SPIE, 5165, 201

[] Burrows, D.N., Hill, J.E., Nousek, J.A., et al. 2005, Space Sci. Rev., 120, 165

[] Cardelli, J. A., Clayton, G. C., & Mathis, J. S. 1989, ApJ, 345, 245

[] Cocchia, F., Fiore, F., Vignali, C., et al. 2007, A&A, 466, 31

[] Condon, J. J., Cotton, W. D., Greisen, E. W., et al. 1998, AJ, 115, 1693

[] Contini M & Viegas S.M. 2000, ApJ, 535, 721

[] Corral, A., Barcons, X., Carrera, F.J., et al. 2005, A&A, 431, 97

[] Comastri, A., Mignoli, M., Ciliegi, P., et al. 2002, ApJ, 571, 771

[] Comastri, A., Brusa, M., Mignoli, M., et al. 2003, AN, 324, 28

[] Cusumano, G., La Parola, V., Segreto, A., et al. 2010, A&A, 524, 64

[] Diamond-Stanic, A.M., Rieke, G.H., Rigby, J.R., 2009, ApJ, 698, 623

[] Dickey, J. M., & Lockman, F. J. 1990, ARA&A, 28, 215

[] Dressler, A., & Shectman, S. 1987, AJ, 94, 899

[] Elitzur, M., & Shlosman, I., 2006, ApJ, 648, 101

[] Elitzur, M., 2007, ASPC, 373, 415

[] Elitzur, M., 2008, [arXiv:0805.3699]

[] Emmering, R.T., Blandford, R.D. and Shlosman, I., 1992, ApJ, 385, 460

[] Fabian A.C., Vaughan S., Nandra K. et al. 2002, MNRAS, 335, 7

[] Filliatre, P., & Chaty, S. 2004, ApJ, 616, 469

[] Fiore, F., Brusa, M., Cocchia, F., et al. 2003, A&A, 409, 79

[] Gehrels, N., Chincarini, G., Giommi, P., et al. 2004, ApJ, 611, 1005

[] George I.M. & Fabian A.C. 1991, MNRAS, 249, 352

[] Giacconi, R., Rosati, P., Tozzi, P., et al. 2001, ApJ, 551, 624

[] Greenhill, L. J., Gwinn, C. R., Antonucci, R., et al. 1996, ApJ, 472, 21

[] Grimm, H. J., Gilfanov, M., Sunyaev, R., 2002, A&A, 391, 923

[] Gu, Q., & Huang, J., 2002, ApJ, 579, 205

[] Guilbert P.W. & Rees M.J. 1988, MNRAS, 233, 475

[] Haardt F. & Maraschi L. 1993, ApJ, 413, 507

[] Harmon, B. A., Wilson, C. A., Fishman, G. J., et al. 2004 Ap. J. Suppl. Series 154, 585

[] Hasinger, G., Burg, R., Giacconi, R., et al. 1998, A&A, 329, 482

[] Hasinger, G., Miyaji, T. and Schmidt, M., 2005, A&A, 441, 417

[] Heckman, T. M. 1980, A&A, 87, 152

[] Heckman T., Krolik J.H., Hewer G. et al. 1995, ApJ, 452, 549

[] Heckman T.M., Kauffmann, G., Brinchmann, J., et al. 2004, ApJ, 613, 109

[] Heckman, T.M., Ptak, A., Hornschemeier, A., et al. 2005, ApJ, 634, 161

[] Hill, J. E., Burrows, D.N., Nousek, J.A., et al. 2004, Proc. SPIE, 5165, 217

[] Ho, L. C., Filippenko, A. V., & Sargent, W. L. W. 1993, ApJ, 417, 63

[] Ho, L. C., Filippenko, A. V., & Sargent, W. L. W. 1997, ApJS, 112, 315

[] Ho, L. C., 2002, ApJ,

[] Isobe, T., Feigelson, E.D., Nelson, P.I., 1986, ApJ, 306, 490

[] Jones, D. H., Saunders, W., Colless, M., et al., 2004, MNRAS, 355, 747

[] Levenson N.A., Krolik J.H., Zycki P.T. et al. 2002, ApJ, 573, 81

[] Liu, Q., Z., Van Paradijs, J., Van den Heuvel, E.P.J., 2001, A&A, 368, 1021

[] Liu, Q., Z., Van Paradijs, J., Van den Heuvel, E.P.J., 2006, A&A, 455, 1165

[] Kaper, V.M., Van der Meer, A., 2005, astro-ph/0502314

[] Kartje, J.F., Konigl, A., and Elitzur, M., 1999, ApJ, 513, 180

[] Kaspi S., Brandt W.N., Netzer H. et al. 2001, ApJ, 554, 216

[] Kauffmann, G., Heckman, T.M., Tremonti, C., et al. 2003, MNRAS, 346, 1055

[] Kinkhabwala A., Sako M., Behar E. et al. 2002, ApJ, 575, 732

[] Konigl, A. & Kartje, J.F., 1994, ApJ, 434, 446

[] Kormendy, J., Richstone, D., 1995, ARA&A, 33, 581

[] Krivonos, R., Tsygankov, S., Revnivtsev, M., et al. 2010, A&A, 523, 61

[] Krolik J.H. & Kriss G.A. 1995, ApJ, 447, 512

[] Labanti, C., Di Cocco, G., Ferro, G., et al. 2003, A&A, 411, L149

[] Lang, K. R. 1992, Astrophysical Data: Planets and Stars (New York: Springer-Verlag)

[] Laurent-Muehleisen, S. A., Kollgaard, R. I., Ciardullo, R., et al. 1998, ApJS, 118, 127

[] Lebrun, F., Leray, J. P., Lavocat, P., et al. 2003, A&A, 411, L141

[] Levine, A. M., Lang, F. L., Lewin, W. H. G., et al. 1984, ApJS, 54, 581

[] Liu Q.Z., Van Paradijs, J., Van den Heuvel, E.P.J., 2000, A&A Suppl. Ser., 147, 25

[] Lund, N., Brandt, S., Budtz-Jorgensen, C., et al. 2003, A&A, 411, L231

[] Maccacaro, T., Gioia, I.M., Wolter, A., et al. 1988, ApJ, 326, 680

[] Mainieri, V., Bergeron, J., Hasinger, G., et al. 2002, A&A, 393, 425

[] maiolino, R., Marconi, A., Salvati, M., et al. 2001, A&A, 365, 28

[] Maiolino, R. & Risaliti, G., 2007, ASPC, 373, 447

[] Malizia, A., Landi, R., Bassani, L., et al. 2007, ApJ, 668, 81

[] Malizia, A., Bassani, L., Bird, A.J., et al. 2008, MNRAS, 389, 1360

[] Malizia, A., Bassani, L., Panessa, F., et al. 2009, MNRAS, 394, 121

[] Masetti, N., Palazzi, E., Bassani, L., Malizia, A., & Stephen, J. B. 2004, A&A, 426, L41 (Paper I)

[] Masetti, N., Mason, E., Bassani, L., et al. 2006a, A&A, 448, 547 (Paper II)

[] Masetti, N., Pretorius, M. L., Palazzi, E., et al. 2006b, A&A, 449, 1139 (Paper III

[]) Masetti, N., Bassani, L., Bazzano, A., et al. 2006c, A&A, 455, 11 (Paper IV)

[] Masetti, N., Morelli, L., Palazzi, E., et al. 2006d, A&A, 459, 21 (Paper V)

[] Masetti, N., Landi, R., Pretorius, M. L., et al. 2007, A&A, 470, 331

- [] Masetti, N., Mason, E., Morelli, L., et al. 2008a, A&A, 482, 113 (Paper VI)
- [] Masetti, N., Mason, E., Landi, R., et al. 2008b, A&A, 480, 715
- [] Masetti, N., Parisi, P., Palazzi, E., et al. 2009, A&A, 495, 121 (Paper VII)
- [] Masetti, N., Parisi, P., Palazzi, E., et al. 2010, A&A 519, A96
- [] Mas-Hesse, M., Giménez, A., Culhane, L., et al. 2003, A&A, 411, L261
- [] Matt, G., Guainazzi, M., Maiolino, R., 2003, MNRAS, 342, 422
- [] Mateos, S., Barcons, X., Carrera, F.J., et al. 2005, A&A, 433, 855
- [] McHardy, I.M., Gunn, K.F., Newsam, A.M., et al. 2003, MNRAS, 342, 802
- [] Melendez, M., Kraemer, S.B., Schmit, H.R., et al. 2008, ApJ, 689, 95
- [] Moran, E.C., Filippenko, A.V., Chornock, R., 2002, ApJ, 579, 71
- [] Moretti, A., Campana, S., Tagliaferri, G., et al. 2004, Proc. SPIE, 5165, 232
- [] Mulchaey, J.S., Koratkar, A., Ward, M.J., et al. 1994, ApJ, 436, 586
- [] Mushotzky R.F., Done C. & Pounds K. 1993, ARA&A, 31, 717
- [] Narayan, R., Mahadevan, R., Grindlay, J. E., et al. 1998, ApJ, 492, 554
- [] Negueruela, I., 2004, Proceedings of ”Massive Stars in Interacting Binaries”, ASP Conf.Ser.367:477,2007
- [] Nenkova, M., Sirocky, M.M., Ivezic, Z., et al. 2008, ApJ, 685, 147
- [] Netzer, H., Mainieri, V., Rosati, P., et al. 2006, A&A, 453, 525
- [] Ogle P.M., Marshall H.L., Lee J.C. & Canizares C.R. 2000, ApJ, 545, 81

[] Osterbrock, D. E., & Pogge, R. W. 1985, ApJ, 297, 166

[] Osterbrock, D.E., 1989, Astrophysics of Gaseous Nebulae and Active Galactic Nuclei. University Science Books, Mill Valley

[] Sako M., Kahn S.M., Behar E. et al. 2001, A&A, 365, 168

[] Severgnini, P., Caccianiga, A., Braito, V., et al. 2003, A&A, 406, 483

[] Sguera, V., Bassani, L., Landi, R., et al 2008, A&A, 487, 619

[] Shakura, N. I., Sunyaev, R. A., 1973, A&A, 24, 337

[] Shaw, S. E., Westmore, M. J., Hill, A. B., et al. 2004, A&A, 418, 1187

[] Silverman, J.D., Green, P.J., Barkhouse, W.A., et al. 2005, ApJ, 618, 123

[] Stephen, J. B., Bassani, L., Molina, M., et al. 2005, A&A, 432, L49

[] Struder L., Briel U., Dennerl K. et al. 2001, A&A, 365L, 18

[] Suganuma, M., Yoshii, Y., Kobayashi, Y., et al. 2006, ApJ, 639, 46

[] Panessa. F. & Bassani, L., A&A, 394, 435

[] Paolillo, M., Shreier, E.J., Giacconi, R., et al. 2004, ApJ, 611, 93

[] Pounds K. & Reeves J. 2002, in Proceedings of the Symposium on ÒNew visions of the X-ray Universe in the XMM-Newton and Chandra eraÓ, 26/30-11-2002, ESTEC, The Netherlands

[] Prugniel, P. 2005, The Hyperleda Catalogue http://leda.univ-lyon1.fr/

[] Revnivtsev, M. G., Sunyaev, R. A., Gilfanov, M. R., et al. 2004, Astron. Lett., 30, 527

[] Risaliti, G., Maiolino, R, and Bassani, L., 2000, A&A, 356, 33

- [] Risaliti, G., Elvis, M., Nicastro, F., 2002, ApJ, 571, 234
- [] Roming, P.W.A., Hunsberger, S.D., Mason, K.O., et al. 2004, Proceedings of the SPIE, 5165, 262
- [] Tueller, J., Baumgartner, W. H., Markwardt, C. B., et al. 2010, ApJS, 186, 378
- [] Tran, H.D., 2001, ApJ, 554, 19
- [] Trouille, L. & Barger, A.J., 2010, ApJ, 722, 212
- [] Ubertini, P., Lebrun, F., Di Cocco, G., et al. 2003, A&A, 411, L131
- [] Ueda. Y., Eguchi, S., Terashima, Y., et al. 2007, ApJ, 664, L79
- [] Van den Heuvel, Heise, 1972, Nat, 239, 67
- [] Van Paradijs, J., & McClintock, J. E. 1995, Optical and ultraviolet observations of X-ray binaries, in X-ray Binaries, ed. W. H. G. Lewin, J. van Paradijs, & E. P. J. van den Heuvel (Cambridge: Cambridge University Press), 58
- [] Ulrich M.H., Maraschi L. & Urry C.M. 1997, ARA&A, 35, 445
- [] Urry, C. M., Padovani, P., PASP, 107, 803
- [] Vargas, M., Goldwurm, A., Denis, M., et al. 1996, A&AS, 120, 291
- [] Vedrenne, G., Roques, J. P., Schonfelder, V., et al. 2003, A&A, 411, L63
- [] Veilleux, S., & Osterbrock, D. E. 1987, ApJS, 63, 295
- [] Voges, W., Aschenbach, B., Boller, T., et al. 1999, A&A, 349, 389
- [] Warner, B. 1995, Cataclysmic variable stars (Cambridge: Cambridge University Press)
- [] Wegner, W. 1994, MNRAS, 270, 229

[] Winkler, H. 1992, MNRAS, 257, 677

[] Winkler, C., Courvoisier, T.J.L., Di Cocco, G., et al. 2003, A&A, 411, L1

[] Winter, L., Lewis, K.T., Koss, M., et al. 2010, ApJ, 710, 503

[] White, N.E., Nagase, F., Parmar, A.N., 1995, in X-ray Binaries, ed. W. H. G. Lewin, J. van Paradijs, & E. P. J. van den Heuvel, Cambridge University Press

[] Wright, E. L. 2006, PASP, 118, 1711

[] Zakamska, N.L., Strauss, M.A., Krolik, J.H., et al. 2003, AJ, 126, 2125

[] Zickgraf, F., Wolf, B., Stahl, O., et al. 1985, A&A, 143, 421

[] Ziolkowski, 2002, Mem. Soc. Astron. Ital., 73 1038